Surface Plasmon

≈ 200 nm

Evanescent field

Gold film
Glass
Index matching fluid
Glass

ε_s
ε_m
ε_p

θ   θ

Light source

Detector

(b)

Laser

p-polarized

Detector

θ

Prism

50 nm Ag or Au

Thin Dielectric Layer

E k_z

+ + + + − − − − + + + +

k_x

z
y
x

n_1
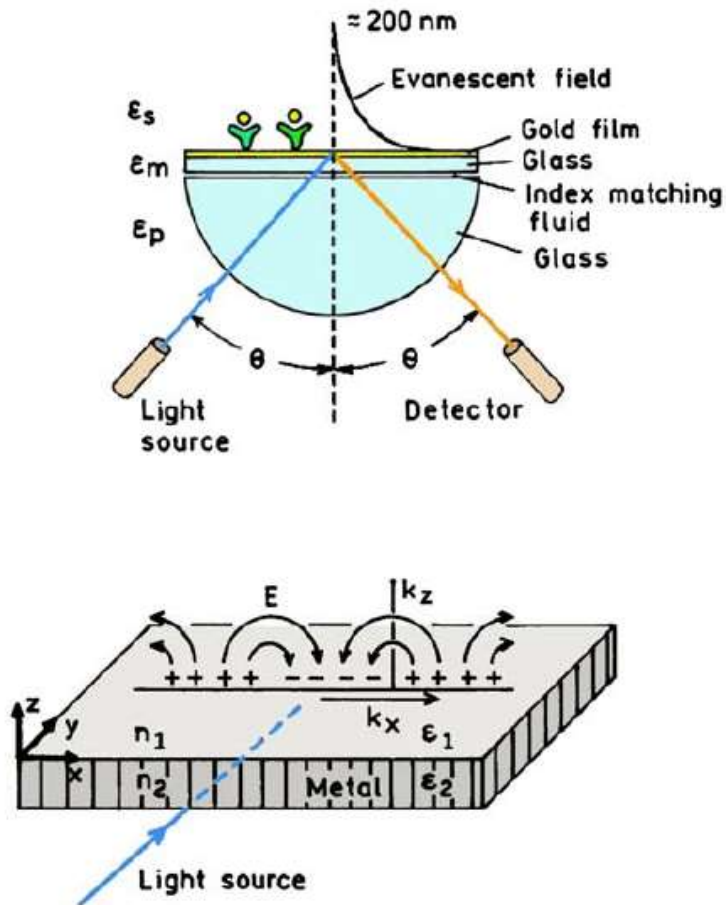n_2 Metal ε_1
ε_2

Light source

Figure 3. Schematics of an SPR experiment (top) and of the light-induced surface plasmons (bottom).

(c)

1.0

0.8

0.6

0.4

0.2

0

Reflectivity, R

θ_c

a   a

38   40   42   44   46   48

θ_0 θ_1

θ / deg

Drift: Drude model

Electric field E

e⁻

random scattering centers
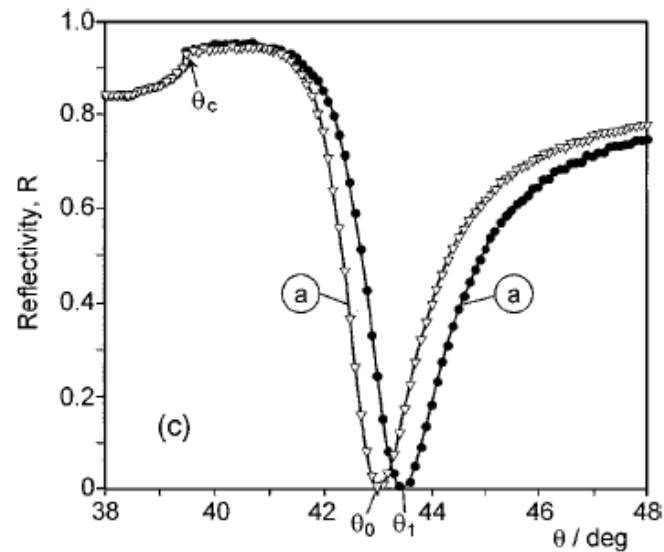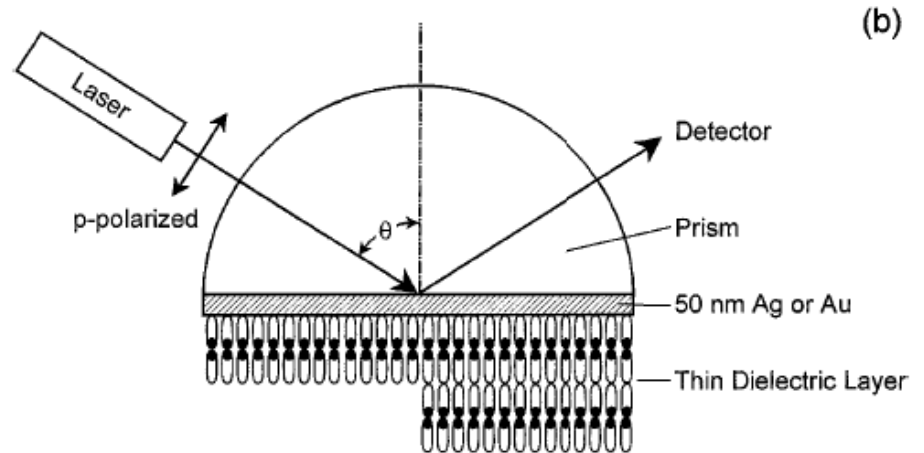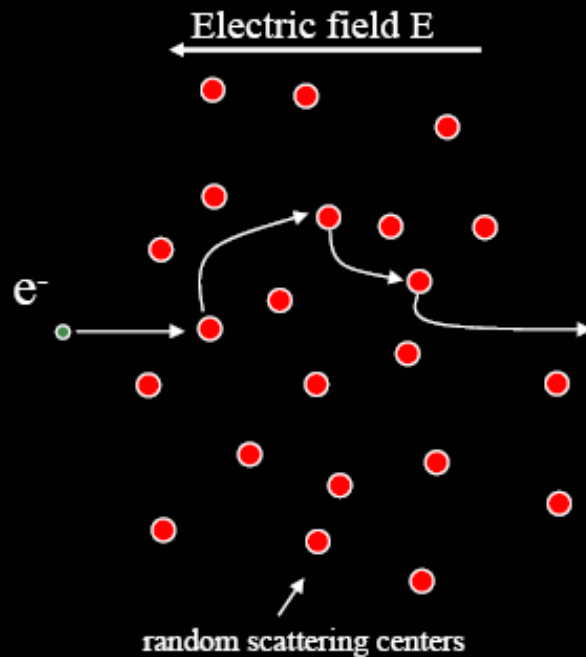
$$F = ma$$

$$eE = m \frac{\partial v}{\partial t}$$

$$v_{avg} = \underbrace{\frac{e\,\tau}{m}}_{\mu} E$$

$$j = ne\,v_{avg} = \underbrace{\frac{ne^2\tau}{m}}_{\sigma} E$$

$$m\frac{\partial}{\partial t}\langle \vec{v} \rangle = q\vec{E} - \gamma\langle \vec{v} \rangle$$

$$\sigma(\omega) = \frac{\sigma_0}{1 + i\omega\tau}$$

AC Dielectric Response

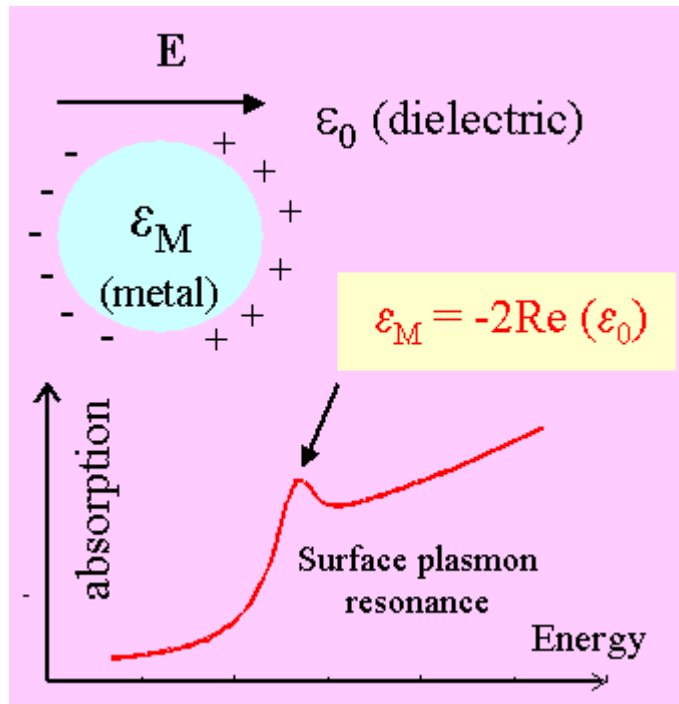$$\varepsilon_m = 1 - \frac{\omega_p^2}{\omega^2}$$

Plasma frequency

polarizability of a small metal sphere with dielectric function $\varepsilon(\lambda)$

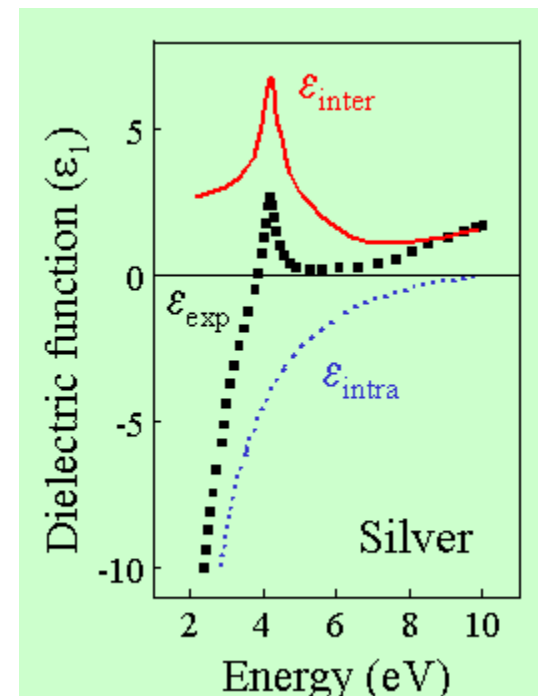$$\alpha = R^3 \frac{\varepsilon - 1}{\varepsilon + 2}.$$

$$\varepsilon = \varepsilon_{\mathrm{b}} + 1 - \frac{\omega_{\mathrm{p}}^2}{\omega^2 + i\omega\gamma},$$

$$\alpha = \frac{R^3(\varepsilon_{\mathrm{b}}\omega^2 - \omega_{\mathrm{p}}^2) + i\omega\gamma\varepsilon_{\mathrm{b}}}{[(\varepsilon_{\mathrm{b}} + 3)\omega^2 - \omega_{\mathrm{p}}^2] + i\omega\gamma(\varepsilon_{\mathrm{b}} + 3)}.$$

$$\omega_{\mathrm{R}} = \frac{\omega_{\mathrm{p}}}{\sqrt{\varepsilon_{\mathrm{b}} + 3}}$$

$$\gamma(\varepsilon_{\mathrm{b}} + 3).$$

E

ε_0 (dielectric)

ε_M (metal)

$\varepsilon_M = -2\text{Re}\,(\varepsilon_0)$

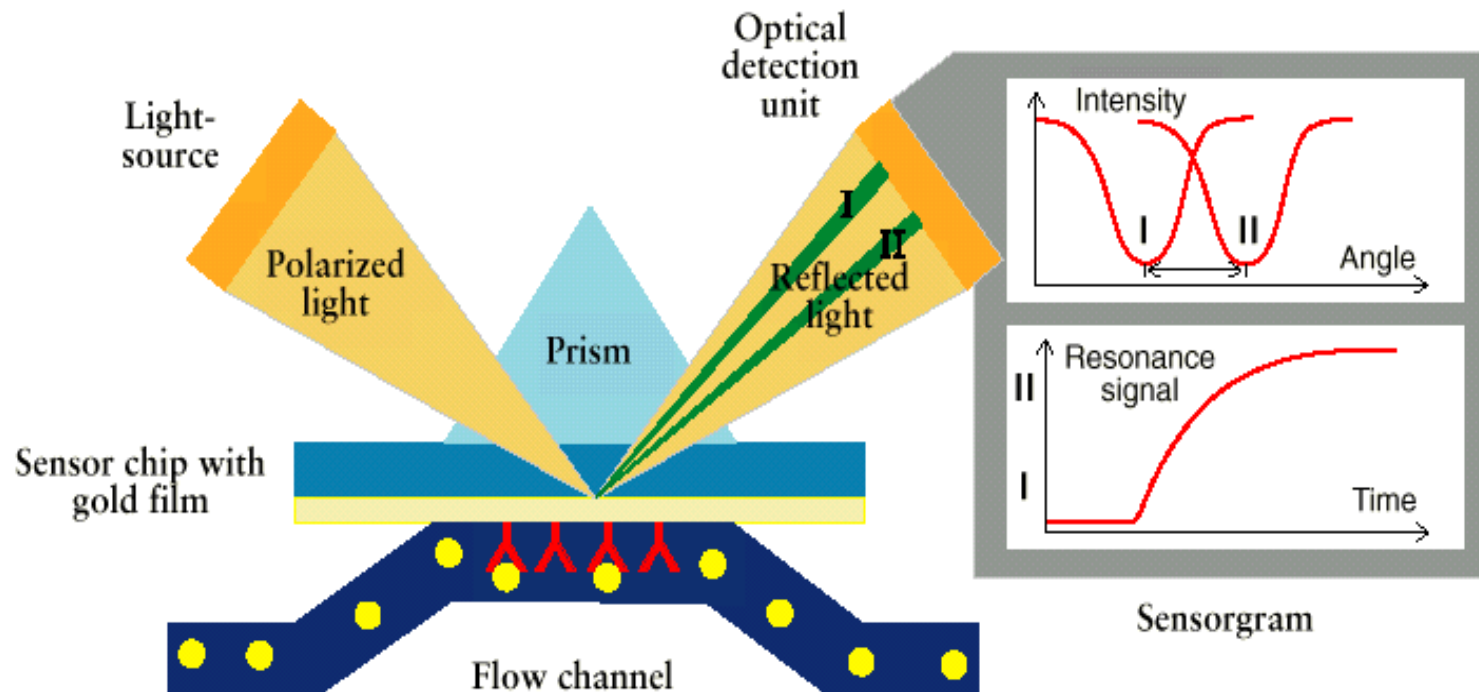absorption

Surface plasmon resonance

Energy

$$\varepsilon_{eff} = \varepsilon_0 + 3N\varepsilon_0 \frac{\varepsilon_M - \varepsilon_0}{\varepsilon_M + 2\varepsilon_0}$$

Dielectric function (ε_1)

ε_{inter}

ε_{exp}

ε_{intra}

Silver

Energy (eV)

Biomolecular Binding in Real Time

Principle of Detection - SPR (Surface Plasmon Resonance)

SPR (Surface Plasmon Resonance) Detection System

Gold-Dextran Surfaces

Sensor Chip

Chip

Lot No:

00245

Biosensor

Microfluidic System

SPR Imaging Apparatus

Flow Cell

Polarizer

Collimated
White Light Source

Gold Film

Prism

Narrow Band
Interference Filter

CCD Camera
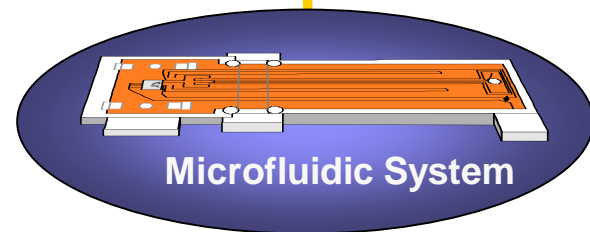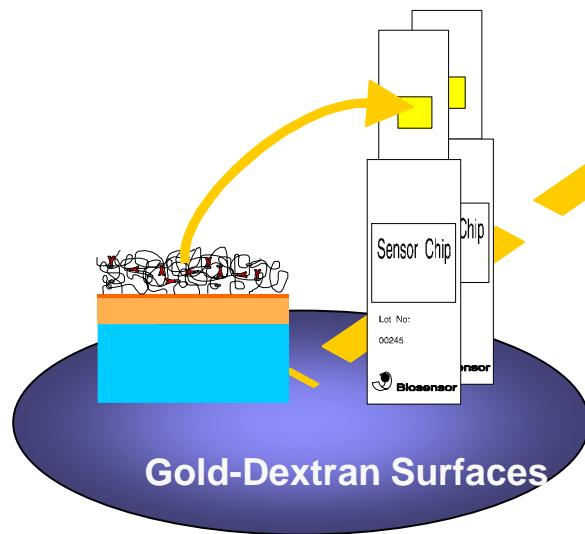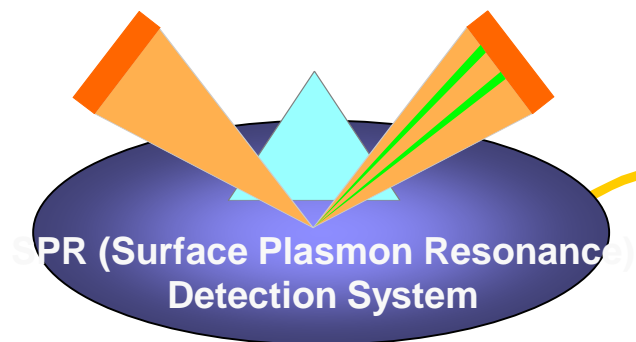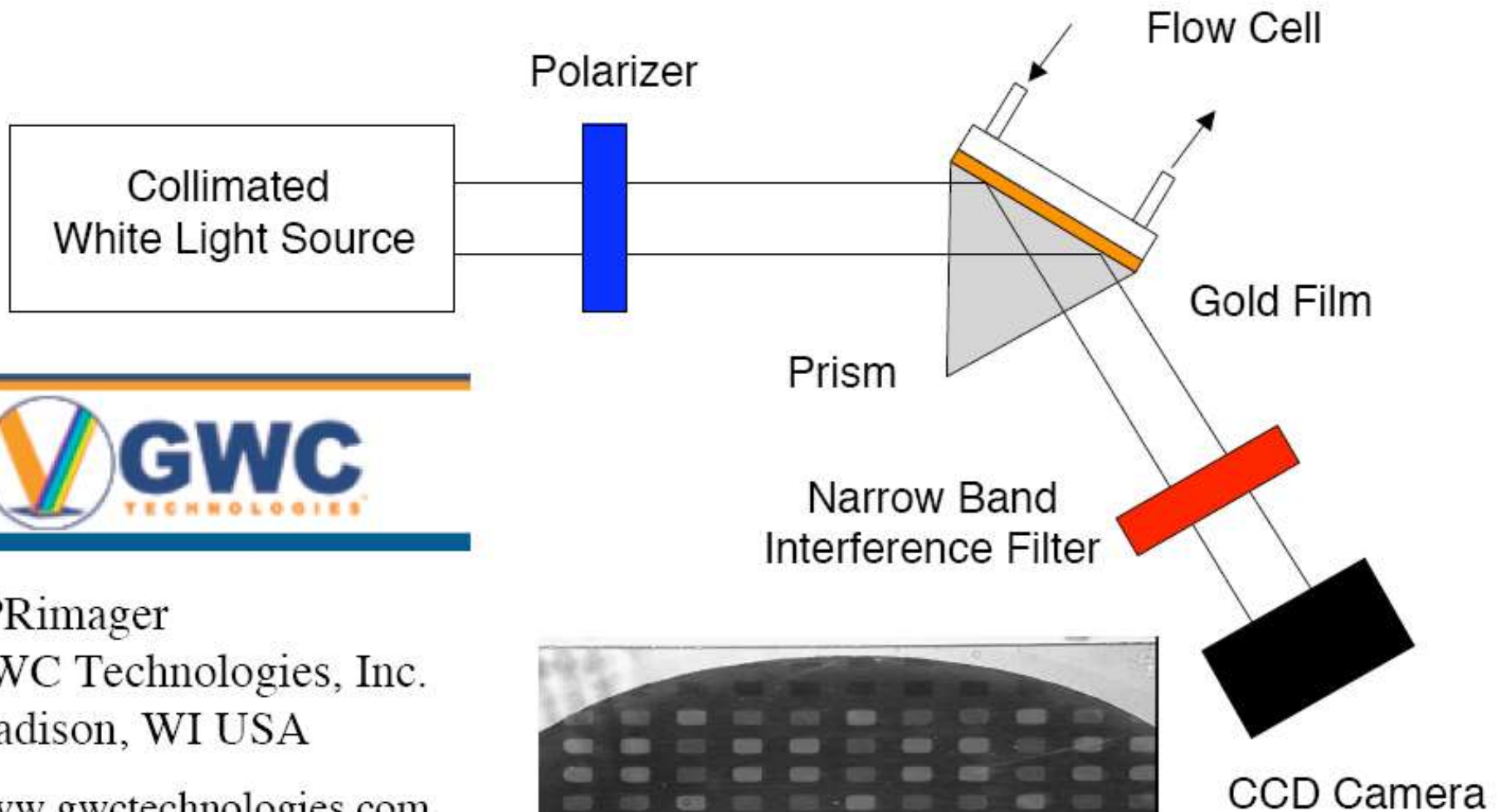
SPRimager
GWC Technologies, Inc.
Madison, WI USA

www.gwctechnologies.com

Raw Image

UCIrvine
University of California, Ir
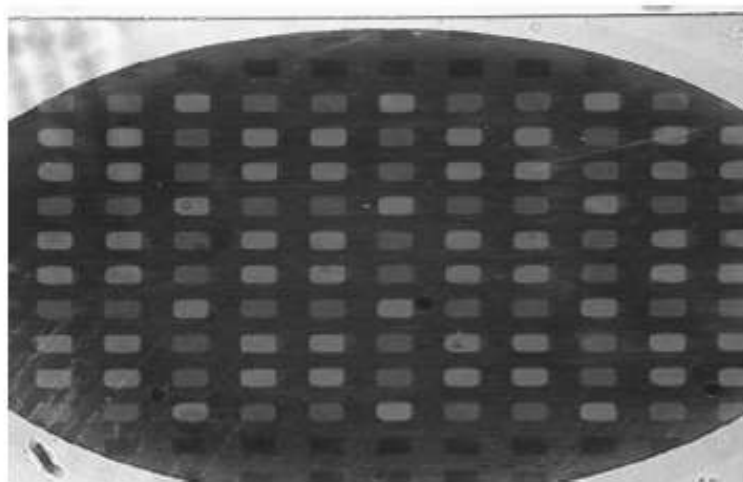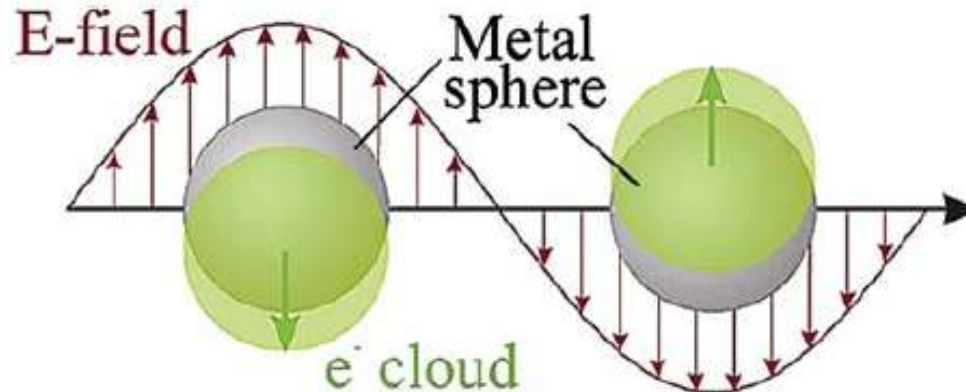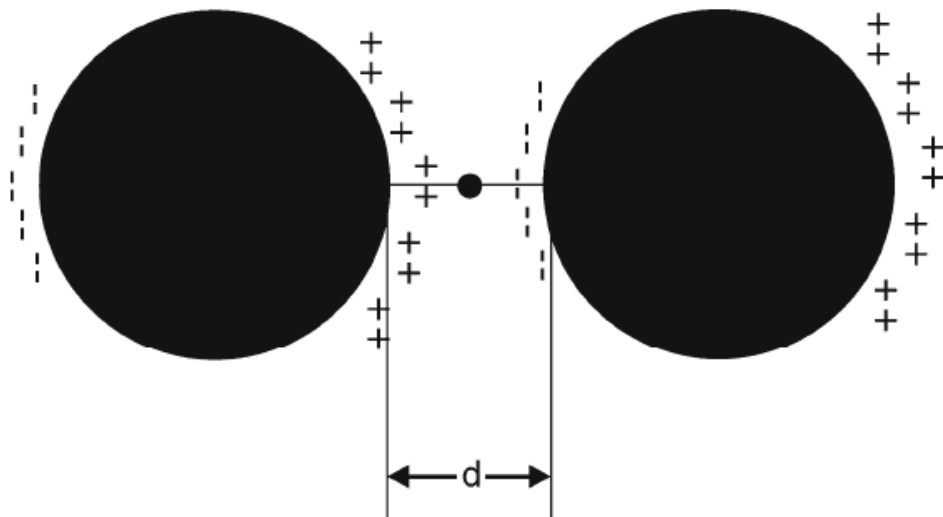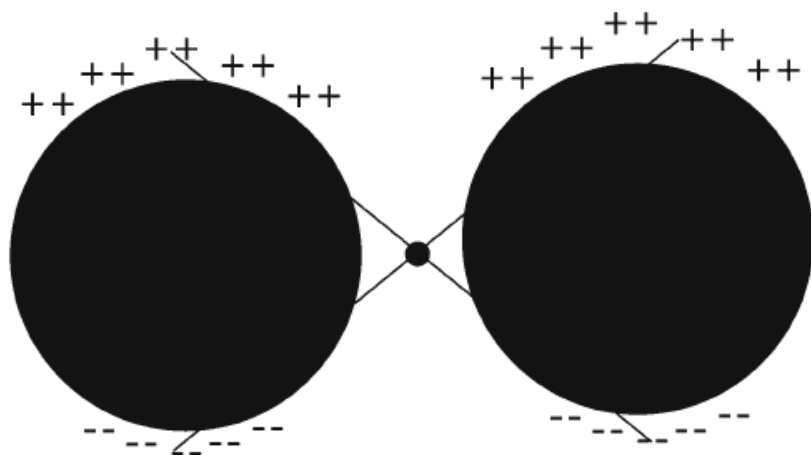
Localized Plasmon

Figure 6. Schematic of plasmon oscillation for a sphere. From [39].

field enhancement

$E_s = gE_0$, where E_0 is the magnitude of the incident field

$$E_R \propto \alpha_R E_s \propto \alpha_R g E_0$$

$$E_{SERS} \propto \alpha_R g g' E_0$$

$$I_{SERS} \propto |\alpha_R|^2 |g g'|^2 I_0$$

$$g \cong g'$$

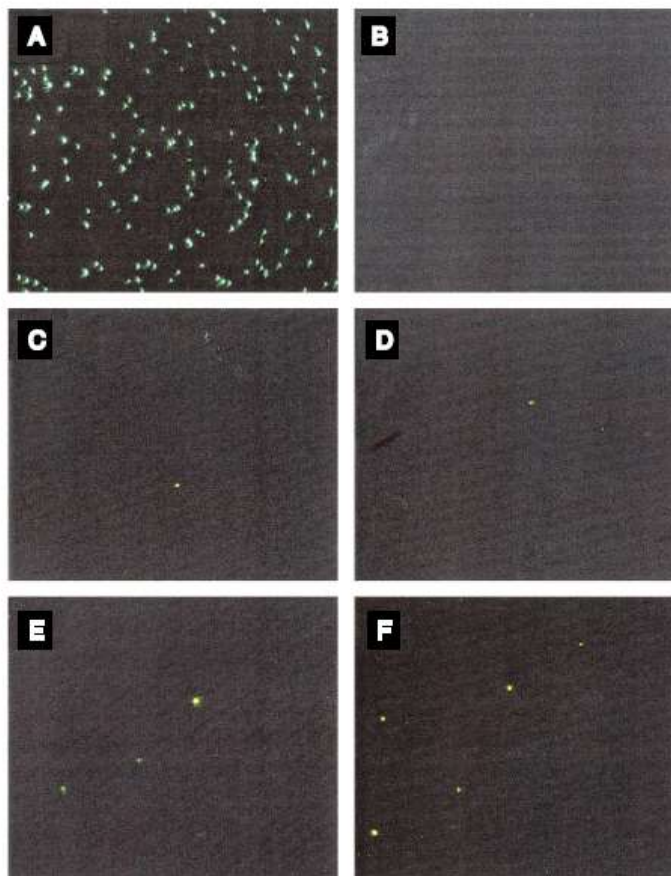$$|E_L|^4 = |g|^4.$$

Probing Single Molecules and Single Nanoparticles by Surface-Enhanced Raman Scattering

Shuming Nie* and Steven R. Emory

Fig. 1. Single Ag nano-particles imaged with eva-nescent-wave excitation. Total internal reflection of the laser beam at the glass-liquid interface was used to reduce the laser scattering background. The instrument setup for evanescent-wave micros-copy was adapted from Funatsu et al. (11). The im-ages were directly record-ed on color photographic film (ASA-1600) with a 30-s exposure by a Nikon 35-mm camera attached to the microscope. (**A**) Un-filtered photograph show-ing scattered laser light from all particles immobi-lized on a polylysine-coat-ed surface. (**B**) Filtered photographs taken from a blank Ag colloid sample (incubated with 1 mM NaCl and no R6G analyte molecules). (**C**) and (**D**) Fil-tered photographs taken from a Ag colloid sample incubated with 2×10^{-11} M R6G. These images were selected to show at least one Raman scatter-ing particle. Different ar-eas of the cover slip were rapidly screened, and most fields of view did not contain visible particles. (**E**) Filtered photograph taken from Ag colloid incubated with 2×10^{-10} M R6G. (**F**) Filtered photograph taken from Ag colloid incubated with 2×10^{-9} M R6G. A high-performance bandpass filter was used to remove the scattered laser light and to pass Stokes-shifted Raman signals from 540 to 580 nm (920 to 2200 cm^{-1}). Continuous-wave excitation at 514.5 nm was provided by an Ar ion laser. The total laser power at the sample was 10 mW. Note the color differences between the scattered laser light in (A) and the red-shifted light in (C) through (F).
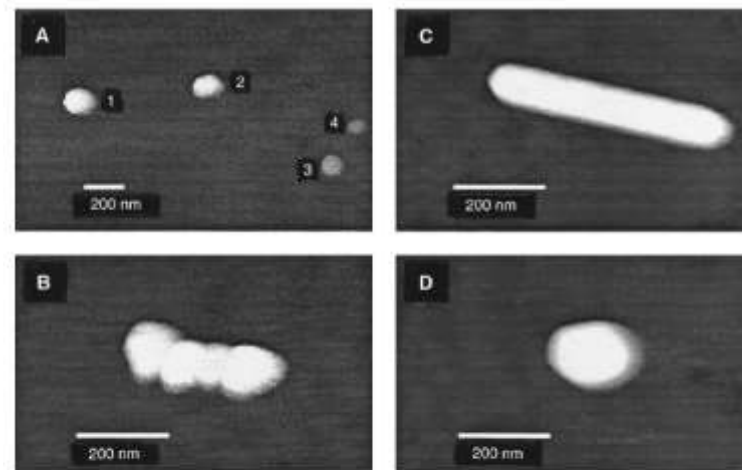

Fig. 2. Tapping-mode AFM images of screened Ag nanoparticles. (**A**) Large area survey image showing four single nanoparticles. Particles 1 and 2 were highly efficient for Raman enhancement, but particles 3 and 4 (smaller in size) were not. (**B**) Close-up image of a hot aggregate containing four linearly arranged particles. (**C**) Close-up image of a rod-shaped hot particle. (**D**) Close-up image of a faceted hot particle.

Fig. 3. Surface-enhanced Raman spectra of R6G obtained with a linearly polarized confocal laser beam from two Ag nanoparticles. The R6G concentration was 2×10^{-11} M, corresponding to an average of 0.1 analyte molecule per particle. The direction of laser polarization and the expected particle orientation are shown schematically for each spectrum. Laser wavelength, 514.5 nm; laser power, 250 nW; laser focal radius, ~250 nm; integration time, 30 s. All spectra were plotted on the same intensity scale in arbitrary units of the CCD detector readout signal.
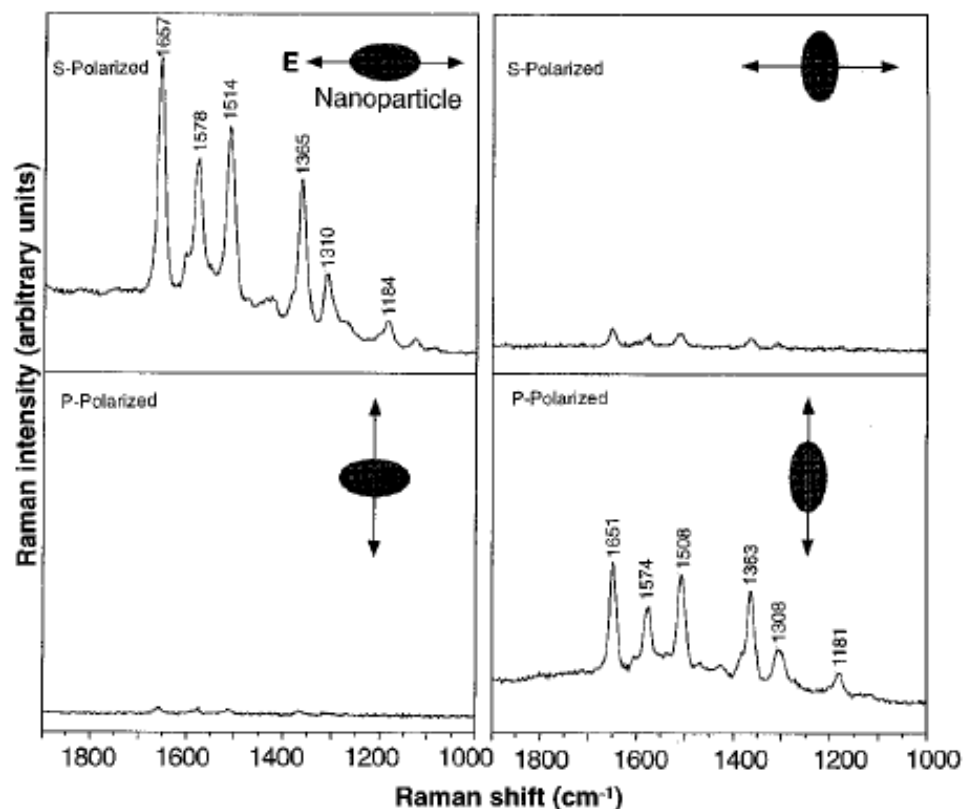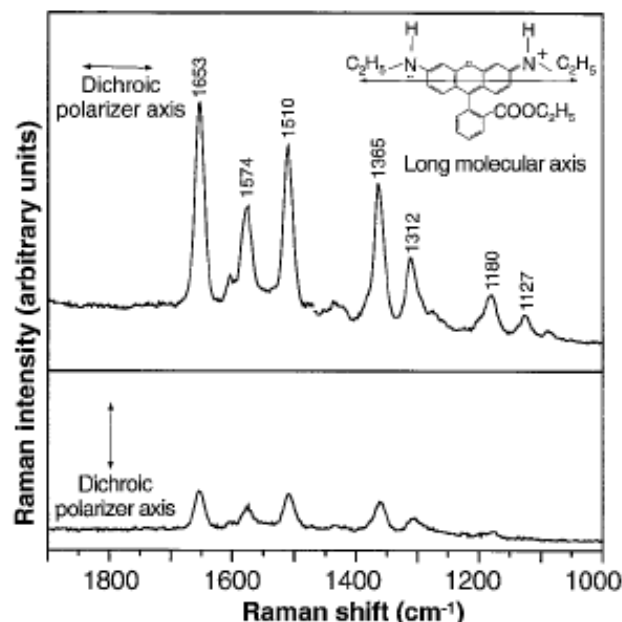
Fig. 4. Emission-polarized surface-enhanced Raman signals of R6G observed from a single Ag nanoparticle with a polarization-scrambled confocal laser beam. A dichroic sheet polarizer was rotated 90° to select Raman scattering signals polarized parallel (upper spectrum) or perpendicular (lower spectrum) to the long molecular axis of R6G. (**Inserts**) Structure of R6G, the electronic transition dipole (along the long axis when excited at 514.5 nm), and the dichroic polarizer orientations. Other conditions as in Fig. 3.

troscopic signatures of adsorbed molecules. For single rhodamine 6G molecules adsorbed on the selected nanoparticles, the intrinsic Raman enhancement factors were on the order of 10^{14} to 10^{15}, much larger than the ensemble-averaged values derived from conventional measurements. This enormous enhancement leads to vibrational Raman signals that are more intense and more stable than single-molecule fluorescence.

Electromagnetic contributions to single-molecule sensitivity in surface-enhanced Raman scattering
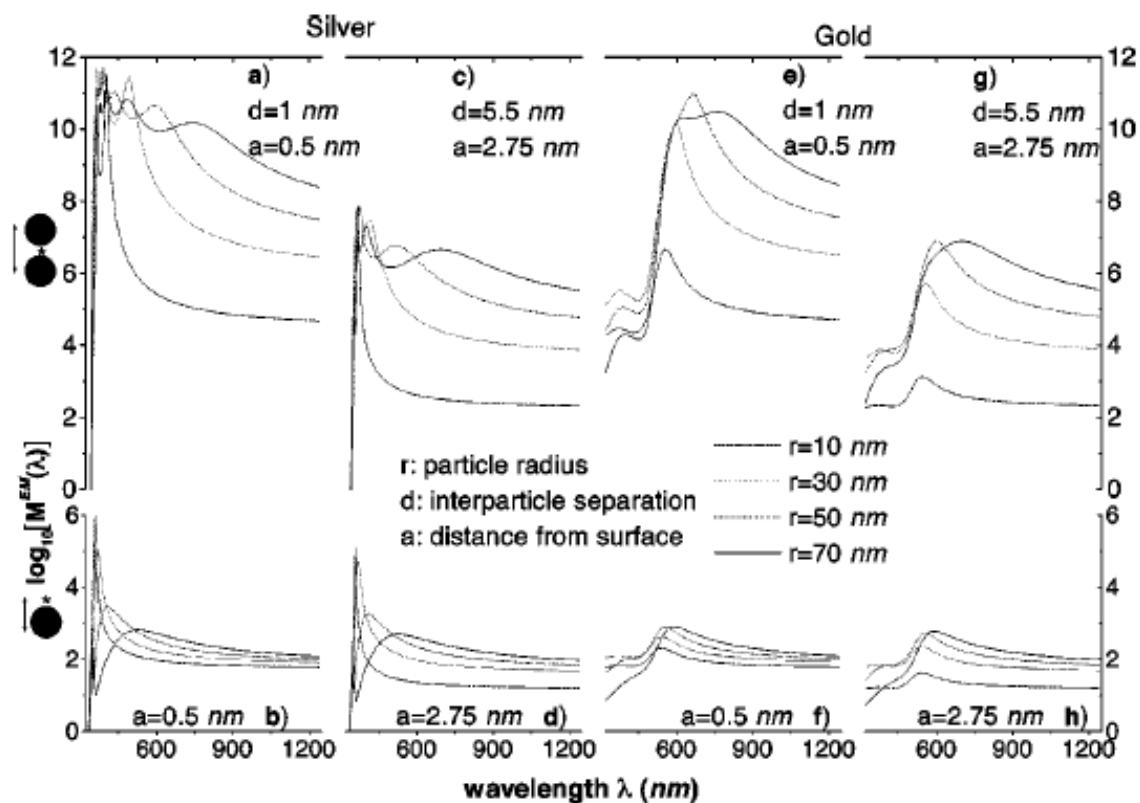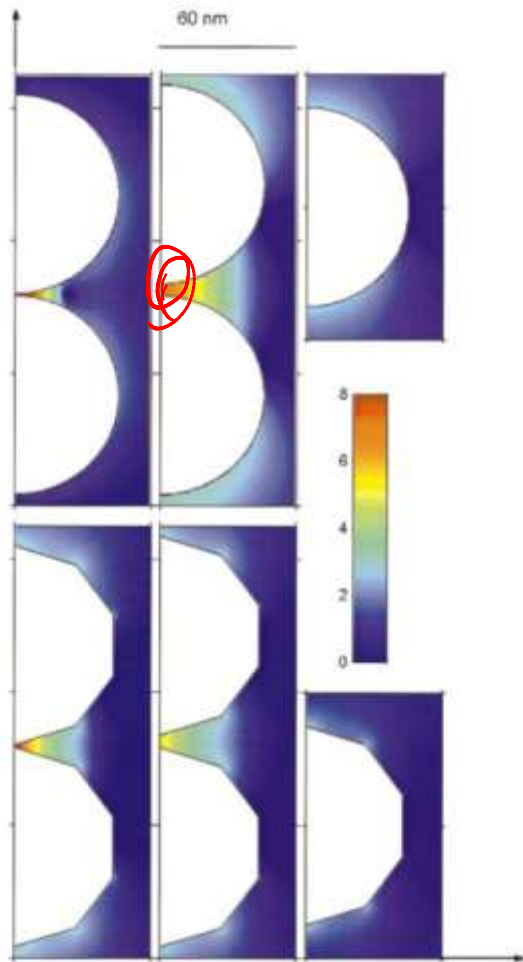
FIG. 3. (Color) EM-enhancement factor M^{EM} at a cross section through six different silver particle configurations. The wavelength of the incident field is $\lambda = 514.5$ nm with vertical polarization. The left-hand column illustrates the EM enhancement for dimer configurations of two spheres (top) and two polygons (bottom) with a separation of 1 nm. The middle column shows the same situation, but with a separation distance of 5.5 nm. The right-hand column shows the case of an isolated single particle. All particles share a common largest dimension of 90 nm. Note that the color scale from dark blue to dark red is logarithmic, covering the interval $10^0 < M^{EM} < 10^8$. Regions with enhancement outside this interval are shown in dark blue and dark red, respectively.
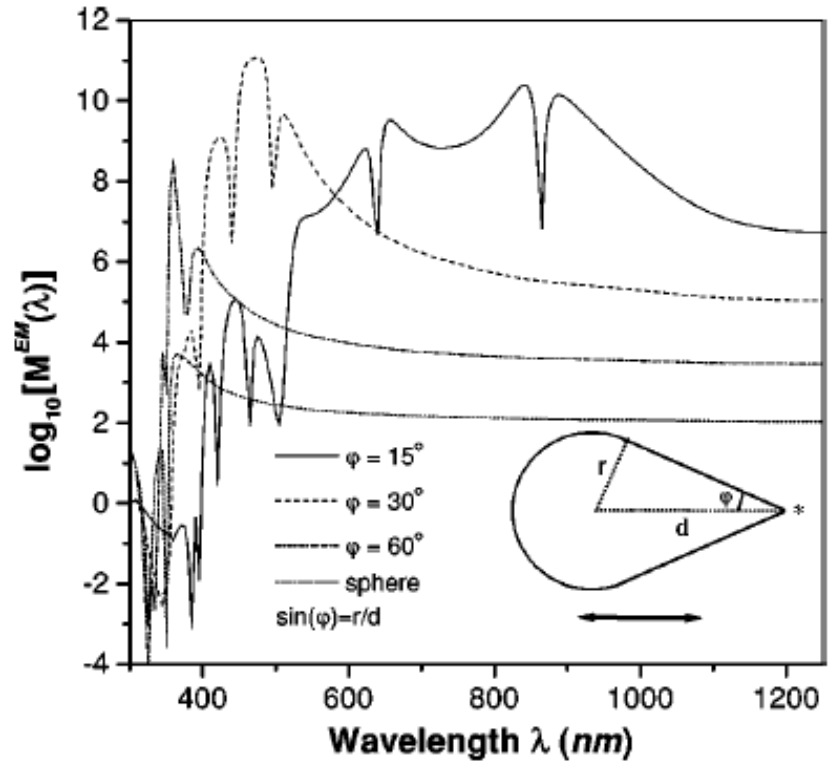

FIG. 5. EM-enhancement factor for a rotationally symmetric silver droplet as a function of the angle defining the opening edge ϕ. The field is polarized parallel to the axis of the droplet and the evaluation position (star) is located 0.5 nm outside the tip. As the droplet becomes sharper the enhancement increases several orders of magnitude.

Nanosphere Arrays with Controlled Sub-10-nm Gaps as Surface-Enhanced Raman Spectroscopy Substrates
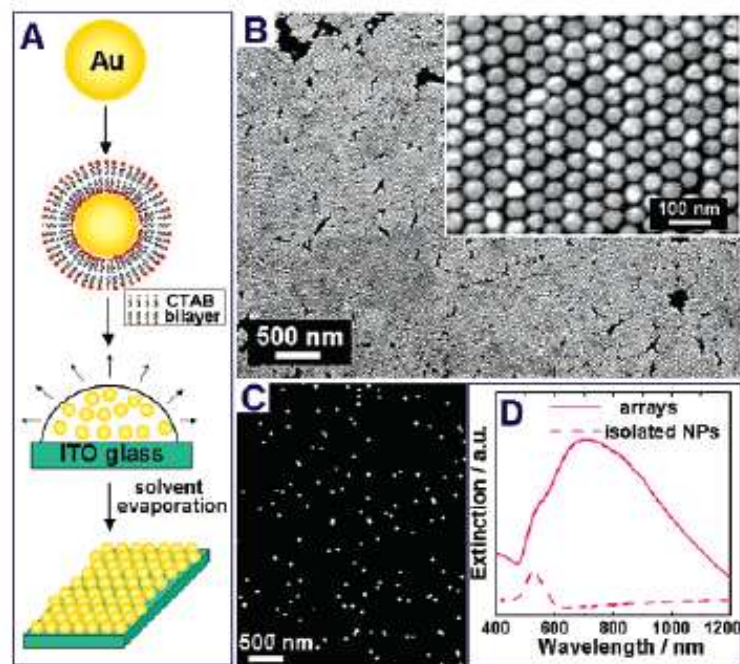
Figure 1. (A) Schematic illustration of the fabrication of sub-10-nm gap Au NP arrays. (B) SEM image of the arrays. (C) SEM image of monolayer of isolated Au NPs on ITO glass. (D) Vis−NIR extinction spectrum of the monolayer of isolated Au NPs and arrays.
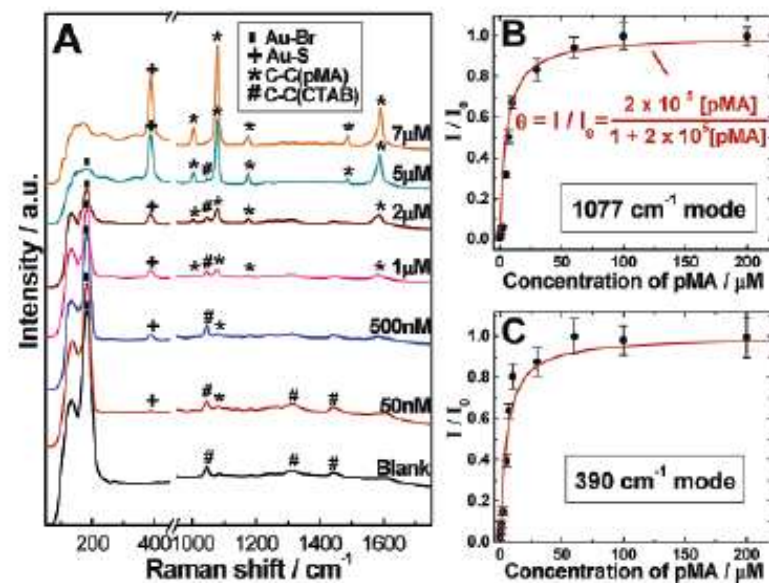
Figure 2. (A) SERS spectra of 5 μL of pMA with different concentrations deposited on the NP arrays. The excitation laser wavelength is 785 nm. Adsorption isotherm of pMA on the NP arrays obtained according to (B) 1077 and (C) 390 cm^{-1} modes in the SERS spectra. I_0 is the peak intensity of a saturated pMA monolayer.

band arises from a coalescence of the dimer plasmon resonances

Profiling the Near Field of a Plasmonic Nanoparticle with Raman-Based Molecular Rulers
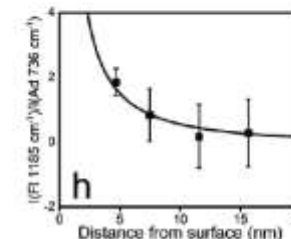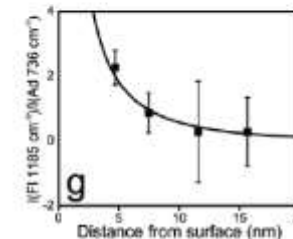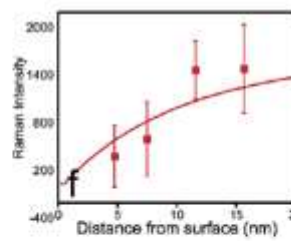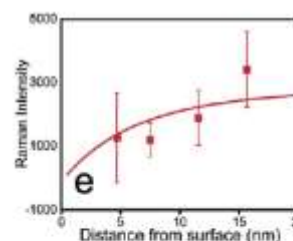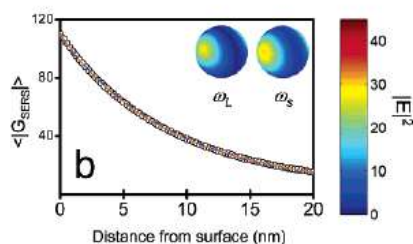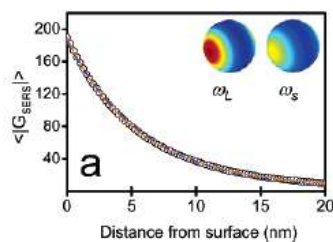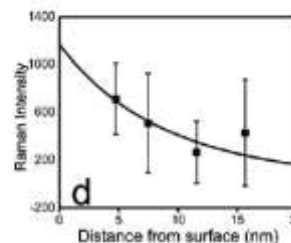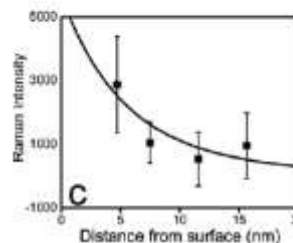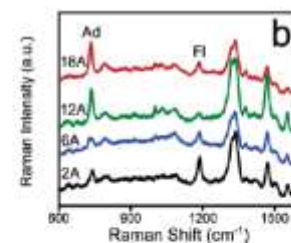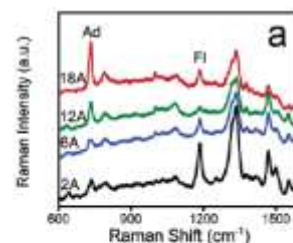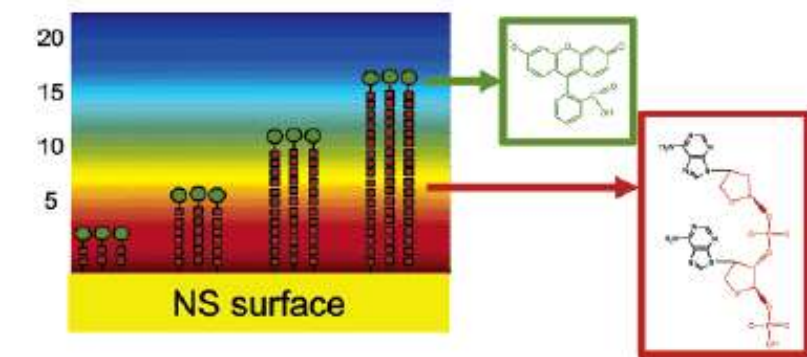
Spectroscopic Tags Using Dye-Embedded Nanoparticles and Surface-Enhanced Raman Scattering
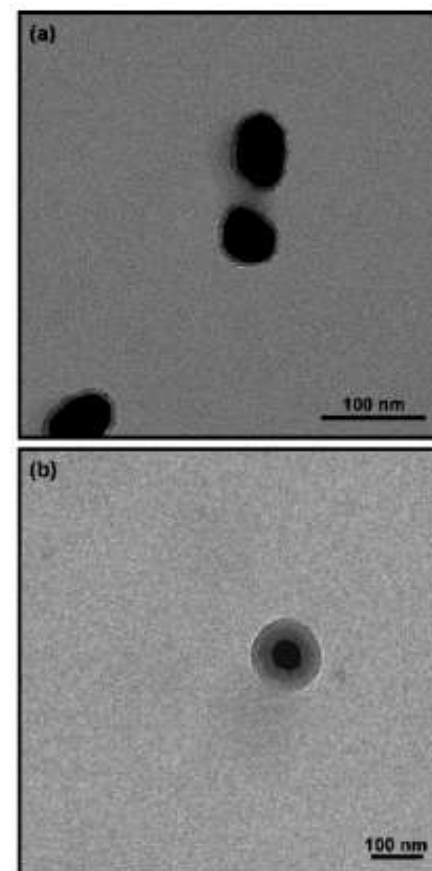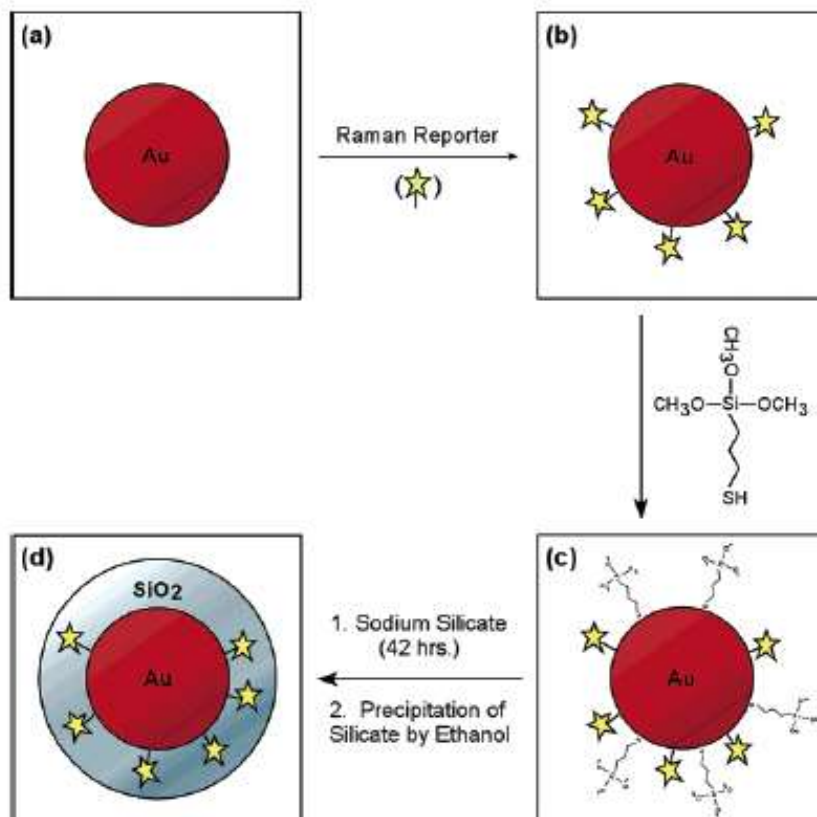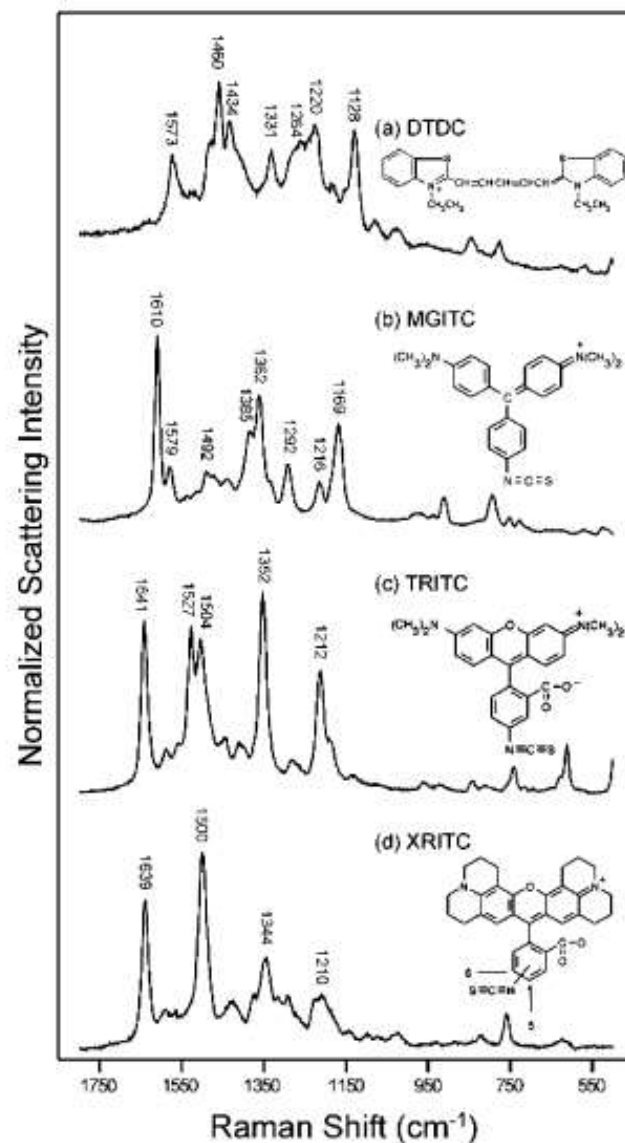
Figure 4. Chemical structures of four Raman reporters and their surface-enhanced resonance Raman spectra: (a) 3,3′-Diethylthiadicarbocyanine iodide (DTDC); (b) malachite green isothiocyanate (MGITC); (c) tetramethylrhodamine-5-isothiocyanate (TRITC); and (e) rhodamine-5-(and-6)-isothiocyanate (XRITC).

Nanoparticle Probes with Surface Enhanced Raman Spectroscopic Tags for Cellular Cancer Targeting
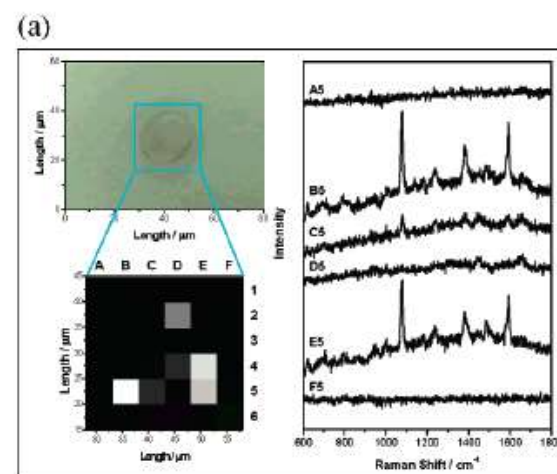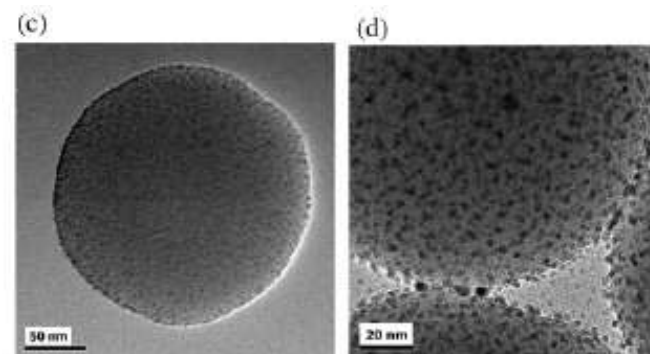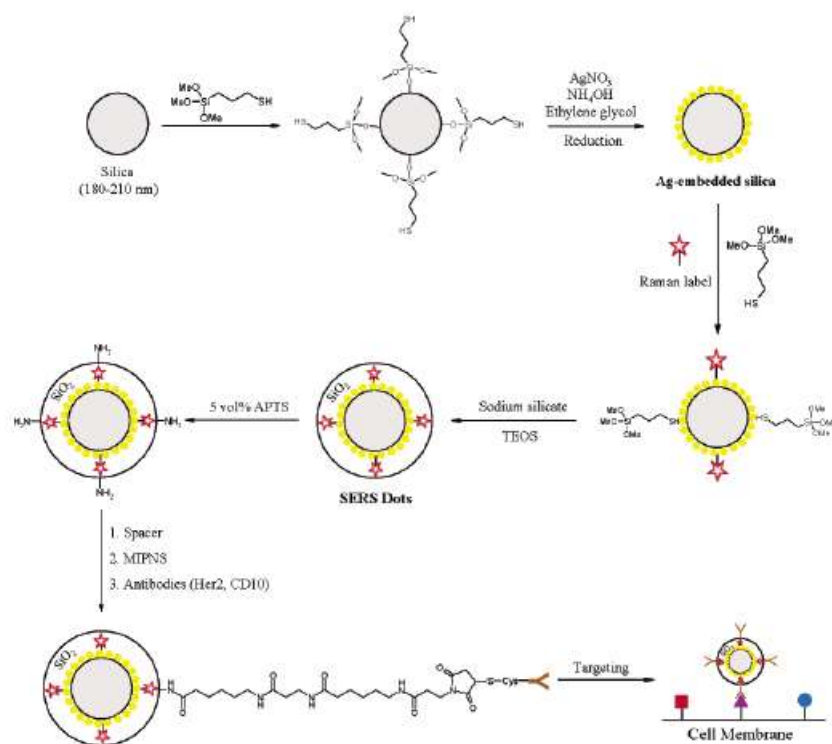
Biological Imaging of HEK293 Cells Expressing PLCγ1 Using Surface-Enhanced Raman Microscopy
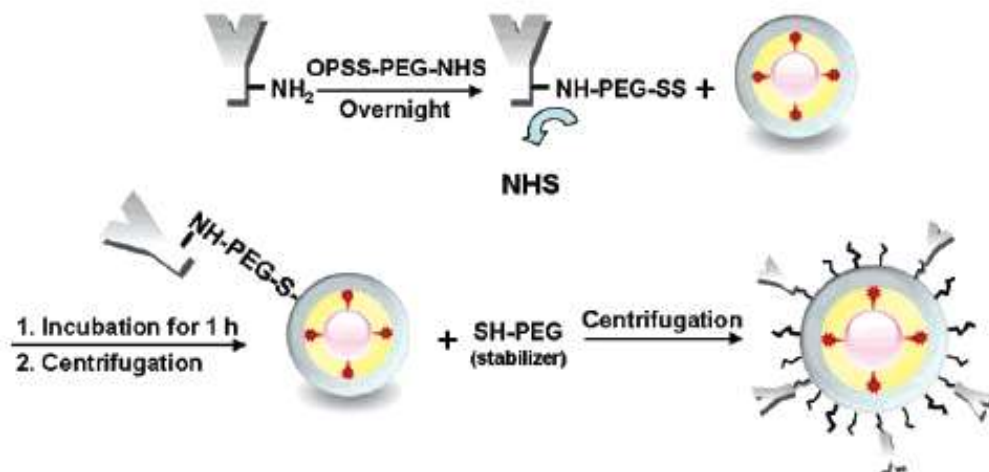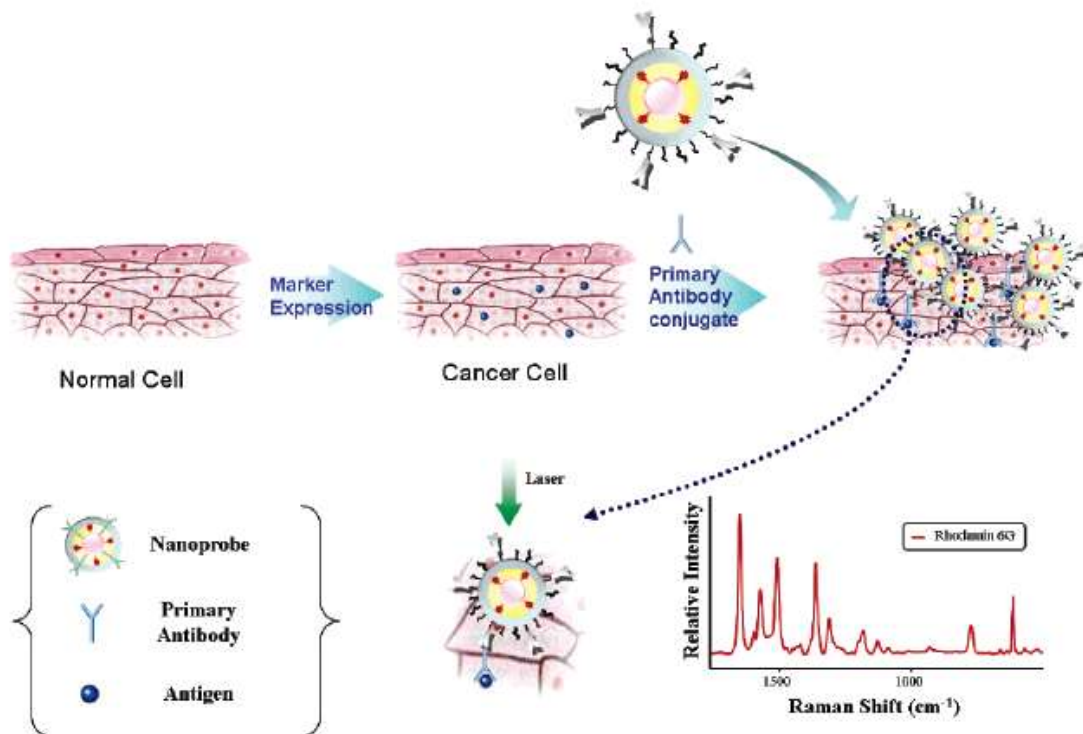
Figure 4. Schematic diagram depicting immobilization of Au/Ag core−shell nanoprobes on PLCγ1-expressing HEK293 cells and their SERS detection.
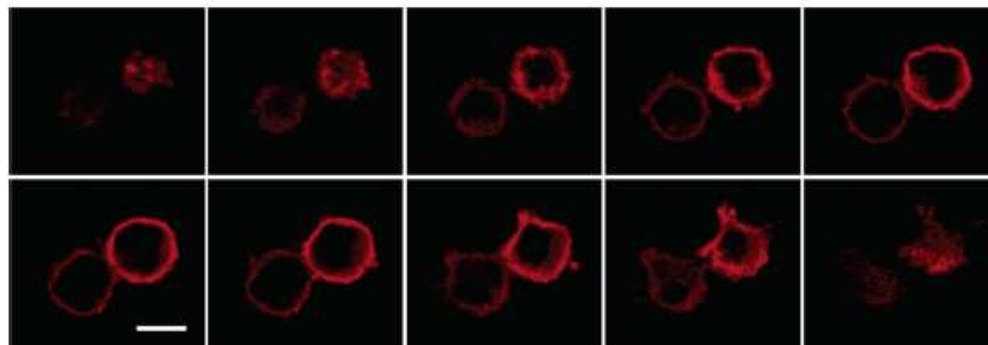
Figure 5. Serial fluorescence optical sections of PLCγ1-expressing HEK293 cells using red QDs. The z-axis interval of optical slices is 1.3 μm. Cells were incubated for 30 min in red QDs, after which the free QDs were washed away. These fluorescence images indicate that PLCγ1 markers are only expressed on the surface membranes. Scale bar, 10 μm.
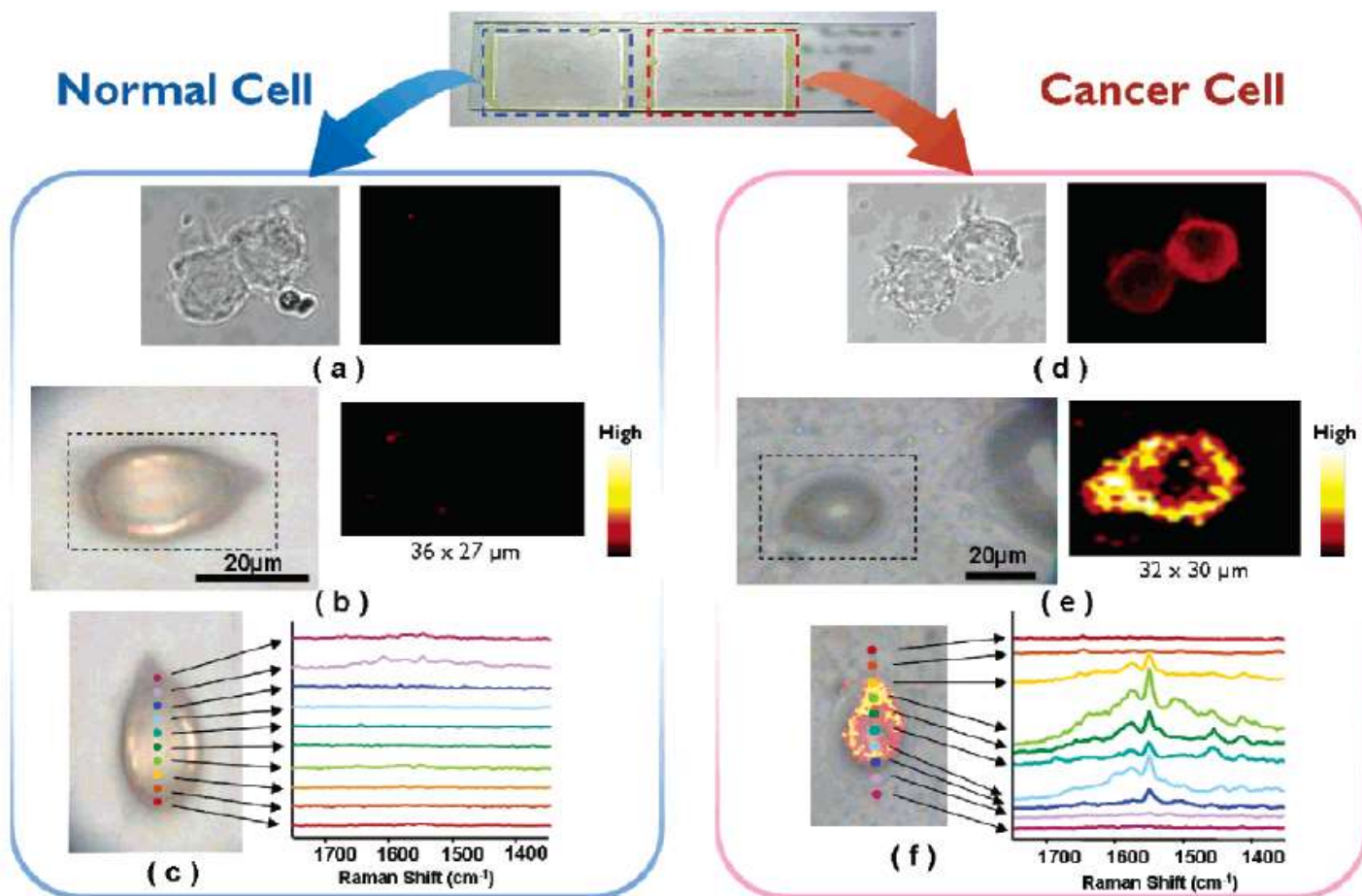
Figure 6. Fluorescence and SERS images of normal HEK293 cells and PLCγ1-expressing HEK293 cells. (a) QD-labeled fluorescence images of normal cells: (left) brightfield image, (right) fluorescence image. (b) SERS images of single normal cell: (left) brightfield image, (right) Raman mapping image of single normal cell based on the 1650-cm^{-1} R6G peak. The cell area was scanned with an interval of 1 μm. Intensities are scaled to the highest value in each area. (c) Overlay image of brightfield and Raman mapping for single normal cell. Colorful spots indicate the laser spots across the middle of the cell along the y axis. (d) QD-labeled fluorescence images of cancer cells: (left) brightfield image, (right) fluorescence image. (e) SERS images of single cancer cell: (left) brightfield image, (right) Raman mapping image of single cancer cell based on the 1650-cm^{-1} R6G peak. The cell area was scanned with an interval of 1 μm. Intensities are scaled to the highest value in each area. (f) Overlay image of brightfield and Raman mapping for single cancer cell. Colorful spots indicate the laser spots across the middle of the cell along the y axis.

Mammalian Cell Surface Imaging with Nitrile-Functionalized Nanoprobes: Biophysical Characterization of Aggregation and Polarization Anisotropy in SERS Imaging
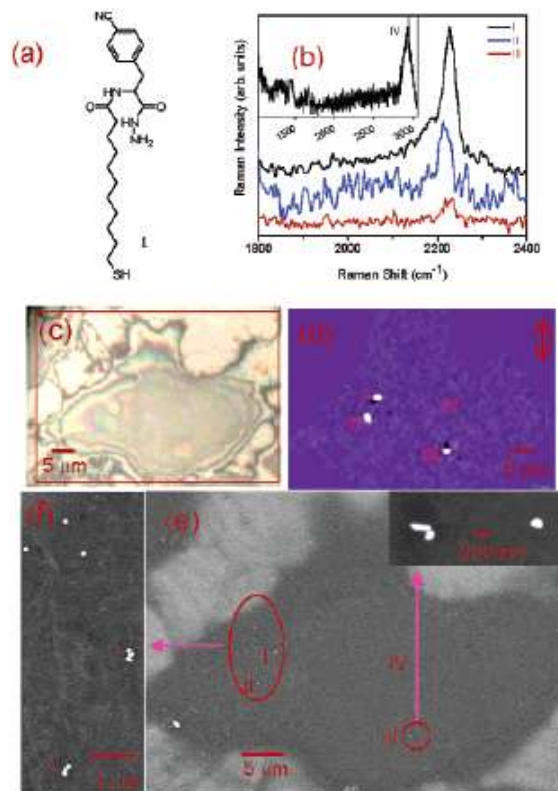
Figure 1. (a) The chemical structure of Raman reporter 1; (b) Raman spectra of the CN vibration mode extracted from positions I, II, and III of the cell shown in the optical image (c). Inset of (b) is a cellular Raman spectrum taken from spot IV of the same cell. (d) Raman intensity map of the C≡N band of the same cell, and (e) the corresponding SEM image. Inset in (e) showed the NPs in the lower right circle. (f) The group of NPs as shown in the large oval of (e).
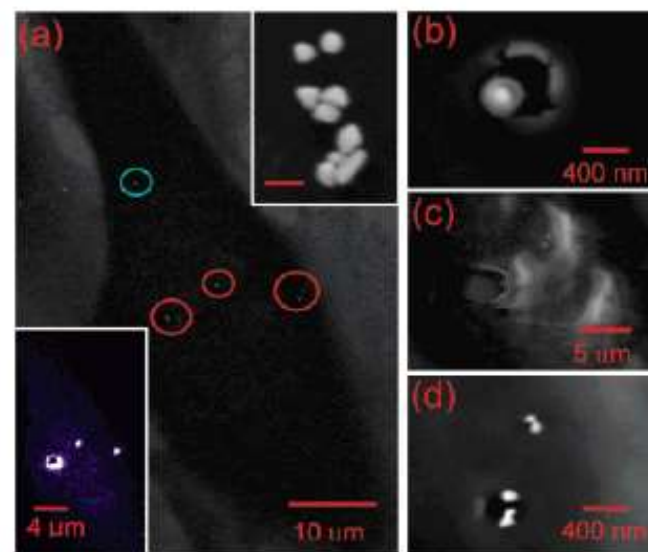
Figure 2. (a) SEM image of a cell. Upper right inset: magnification of a group of aggregated NPs. The scale bar is 200 nm. Lower left inset: the corresponding Raman intensity image of the same cell obtained with a power density of 10^5 W/cm^2. Laser-induced damage to the cell is shown in (b) the monomer (blue circle in a), (c) the aggregates, and (d) a pair of dimers.

Molecular imaging of live cells by Raman microscopy

Almar F Palonpon[1,2], Mikiko Sodeoka[2,3] and Katsumasa Fujita[1,2]

Color channels: cyto c (G), protein (B), lipid (R)

(a)

min 0 5 10
15 20 25

5μm   Color channels: cyto c (G), protein (B), lipid (R)

(b)

min 0 5 10
15 20 25

5μm   Color channels: cyto c (G), protein (B), lipid (R)

(c)

min 0
5
10
15
20
25
30
35

10 μm   Color channels: cyto c (G), protein & lipid (B)

Raman shift [cm⁻¹]

800   1200   1600

Current Opinion in Chemical Biology

(a)

Alkyne

EdU   dU

EdU   dU   cell

Silent Region

Alkyne

N₂

Raman shift (cm⁻¹)

(b)

with EdU   without EdU

10 μm   10 μm

Color channels: cyto c (B), protein (G), EdU (R)

(c)

control   3 hr

9 hr   12 hr

14 hr   21 hr

10 μm

Color channels: cyto c (B), protein (G), EdU (R)

(d)

AltQ2

(e)

747 cm⁻¹   2122 cm⁻¹   2248 cm⁻¹   overlay

10 μm

Color channels: cyto c (B), EdU (R), AltQ2 (G)

Current Opinion in Chemical Biology

(a)

Alkyne vs Nitrile

CC 2110

CN 2242

2.34

1.00

Relative intensity

Raman shift (cm⁻¹)
2000 2100 2200 2300

Azide vs Nitrile

CN 2242

N₃ 2096

1.00

0.38

Relative intensity

Raman shift (cm⁻¹)
2000 2100 2200 2300

Deuterium vs Nitrile

11xCD 2124 CN 2241

1.07
1.00

Relative intensity

Raman shift (cm⁻¹)
2000 2100 2200 2300

(b)

R: Alkyl, Alkenyl, Acyl, etc.
Ar: Aryl, X: SiMe₃, Br, or I

Raman Intensity versus EdU (RIE)

F   Ar══F══Ar

E3 Ar══E3══X   Ar══C══Ar   E2 Ar══E2══R

E1 Ar══E1══H

D3 R══D3══X   D2 R══D2══R

B3 Ar══B3══X   D1 R══D1══H   B2 Ar══B2══R

B1 Ar══B1══H   EdU

A3 R══A3══X

A1 R══A1══H   A2 R══A2══R

10

1

0.1

Raman shift (cm⁻¹)
2100 2150 2200 2250

(c)

RIE: 0.73   1.3   0.85   2.8
Raman shift: 2100   2103   2194   2164

Current Opinion in Chemical Biology

A) General click chemistry

1 step — fixation → — 2 step — Cu catalyst / click reaction → fluorescent imaging

SM = small molecule
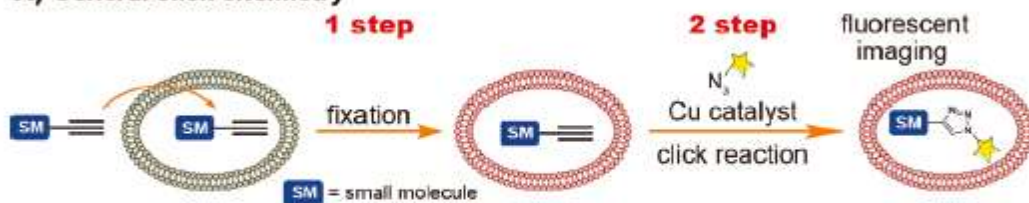
B) Cu-free click chemistry

1 step — Cu-free click reaction → fluorescent imaging

C) This time (Click-free)

Raman Tag

Direct Raman imaging in living cells
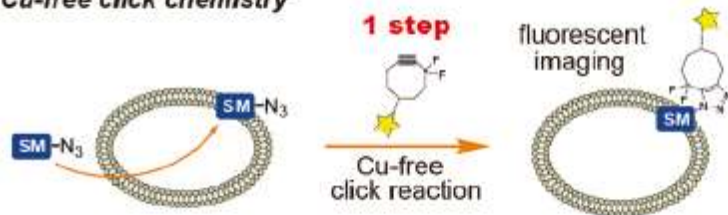
Figure 1. Concept of click-free imaging.

2122

silent region

representative cellular signal

Intensity (a.u.) — Raman shift (cm⁻¹)

EdU / BrdU / dU / N₂

alkyne tag

EdU   BrdU   dU
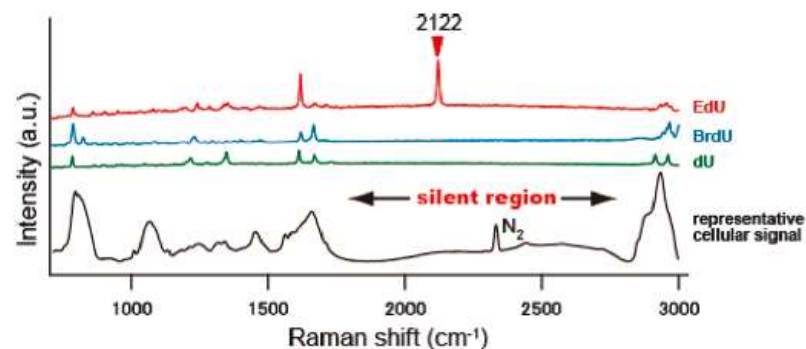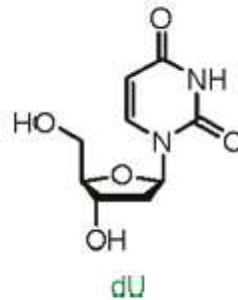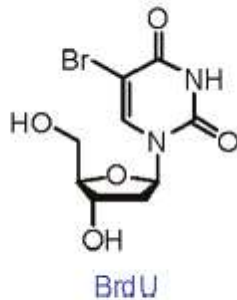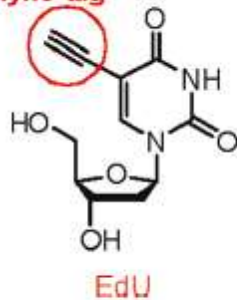
Figure 2. Structures of thymidine analogues.

a

Laser

Spectrometer

CCD   Slit

GLP

Shutter   ≈ To PC

L1   Edge filter

L2   Cylindrical lens   L3

Periscope   GM1 (x)   L5   L6

Dichroic mirror

Microscope tube lens

≈ From CCD

PC

Halogen lamp
BP filter
Condenser lens/DF condenser
Sample
Objective

← Raman excitation/detection
◄----- BF/DF observation

DF observation
IR   Filter
L7   L8   EM-CCD-1

To PC

— Line-shaped laser focus

Video camera

BF observation

TV monitor

b

n = n + 1

PC
Voltage output at V_n

Galvanometer mirror
Relocate laser focus at X_n

Cooled CCD camera   Trigger →   Shutter for laser
Camera exposure   Shutter open

PC
Save nth frame of CCD image

c

Bright-field image

y direction

Scan direction

$x_1 x_2 x_3 \cdots$ x_n
x direction

A cm⁻¹   B cm⁻¹   C cm⁻¹

y direction

CCD image
(400 × 1,340 pixel)

x direction

Wavenumber

Raman image at A cm⁻¹

y direction

x direction

B cm⁻¹

x direction

C cm⁻¹

x direction

Alkynyl sugar analogs for the labeling and visualization of glycoconjugates in cells

Scheme 1. Modified sugar analogs and probes used in this study.
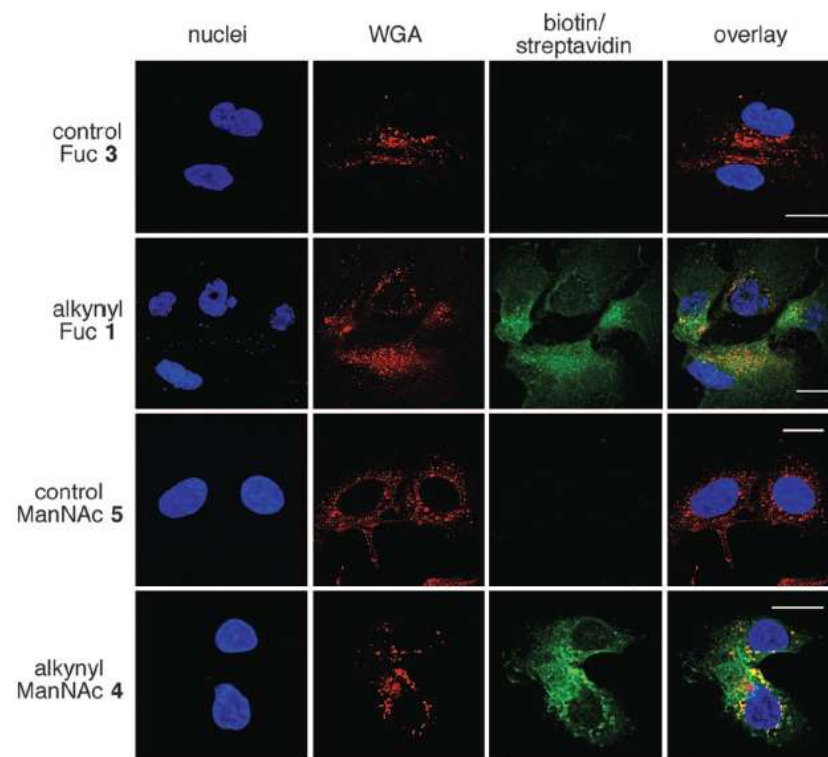
Cell-permeable probe for identification and imaging of sialidases
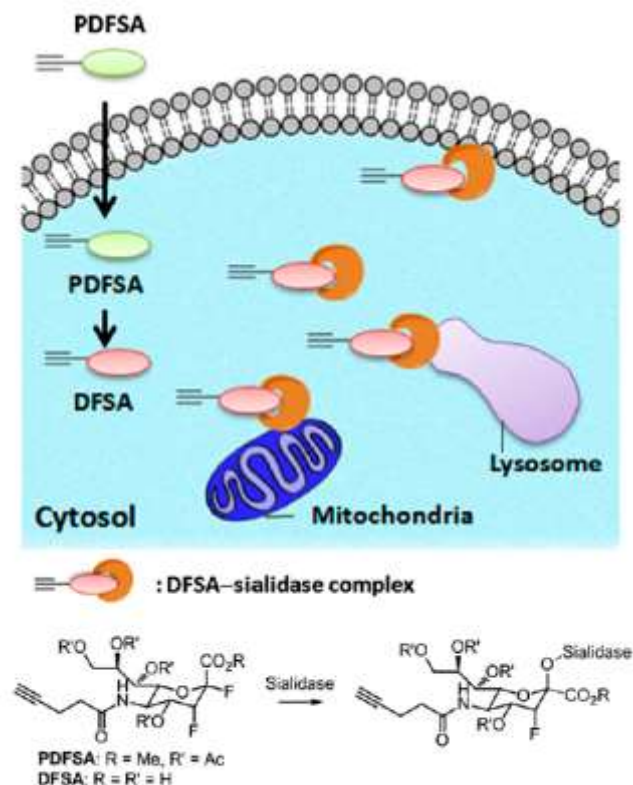
Fig. 1. Identification and imaging of sialidase with activity changes using these activity-based sialidase probes.
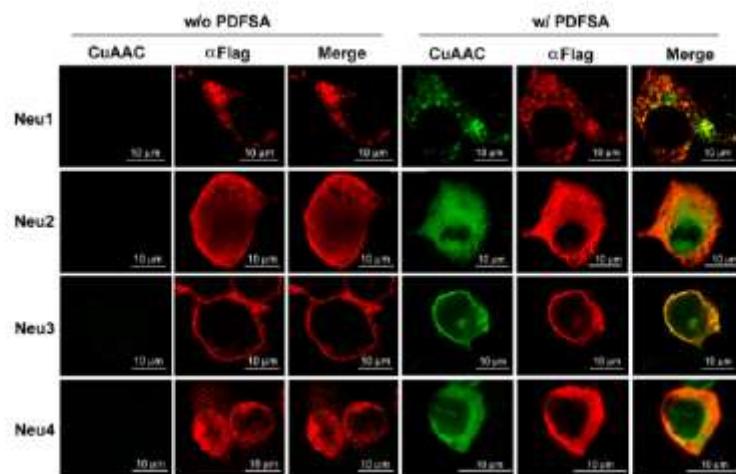
Nanomedicine

Nanobots
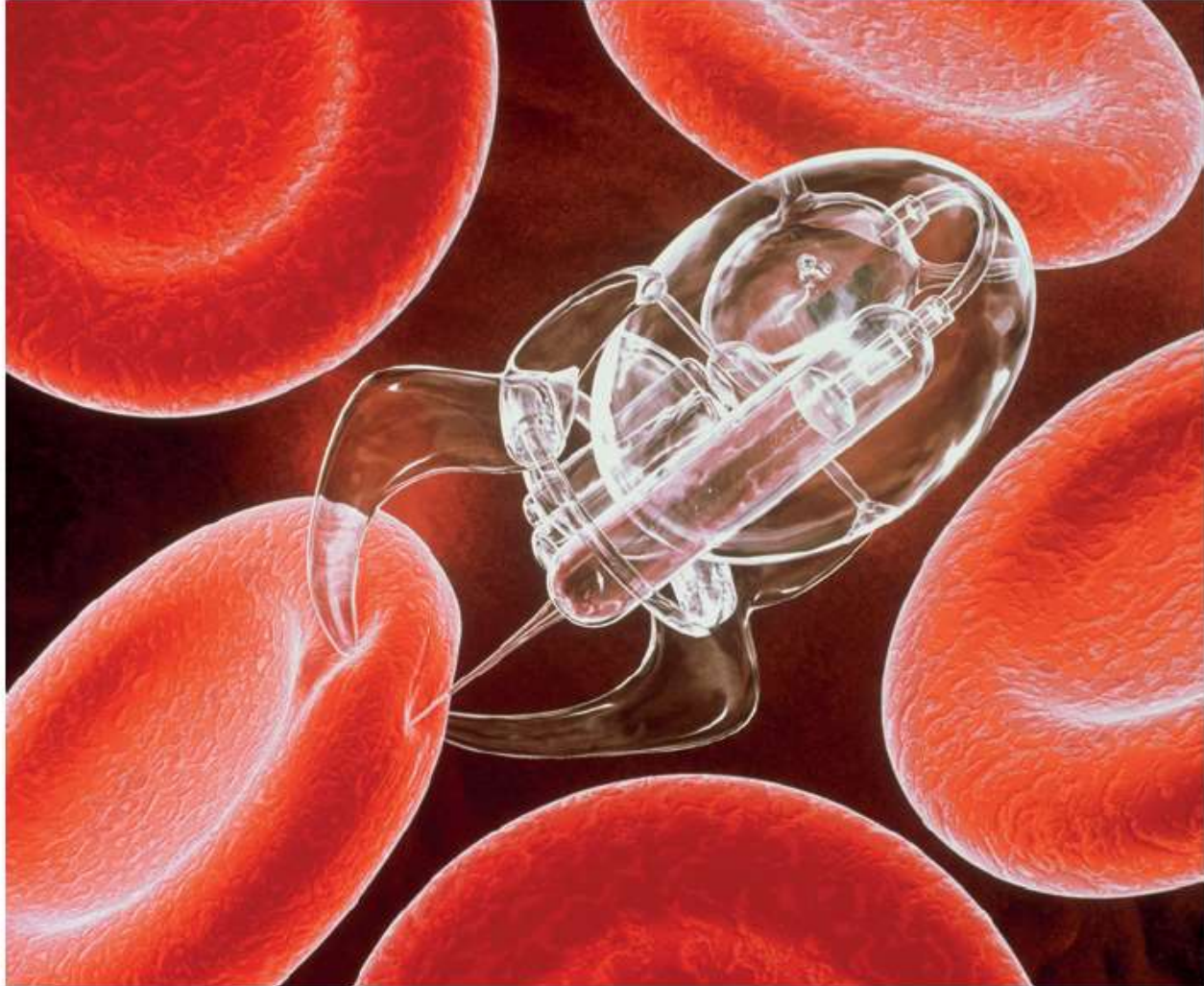
© CONEYL JAY / GETTY IMAGES

Virus Infection
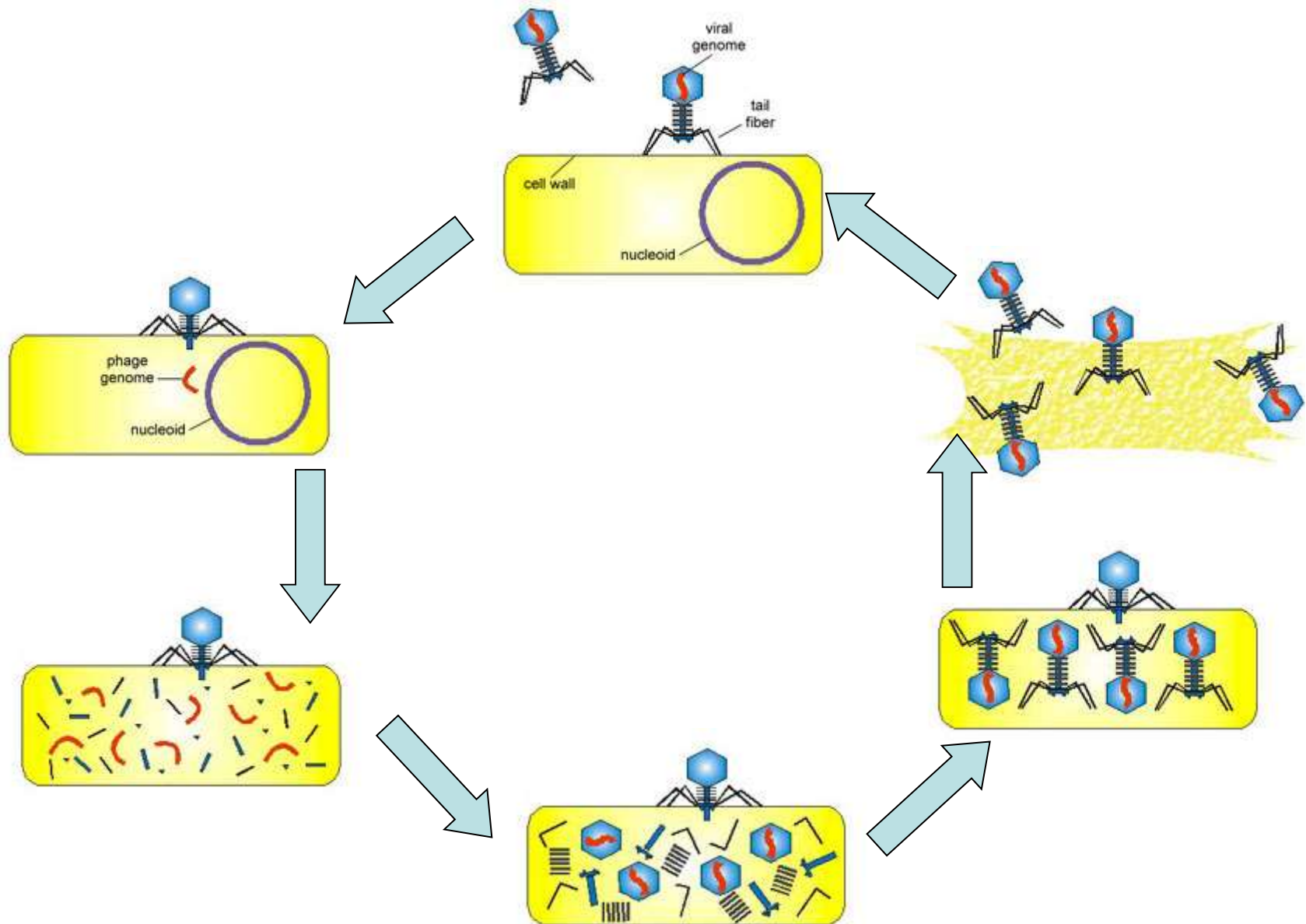
Table 1. Examples of Nanomaterials in Clinical Use.*

Nanomaterial	Trade Name	Application	Target	Adverse Effects	Manufacturer	Current Status
Metallic						
Iron oxide	Feridex	MRI contrast	Liver	Back pain, vaso-dilatation	Bayer Schering	FDA approved
	Resovist	MRI contrast	Liver	None	Bayer Schering	FDA approved
	Combidex	MRI contrast	Lymph nodes	None	Advanced Magnetics	In phase 3 clinical trials
	NanoTherm	Cancer therapy	Various forms	Acute urinary retention	MagForce	In phase 3 clinical trials
Gold	Verigene	In vitro diagnostics	Genetic	Not applicable	Nanosphere	FDA approved
	Aurimmune	Cancer therapy	Various forms	Fever	CytImmune Sciences	In phase 2 clinical trials
Nanoshells	Auroshell	Cancer therapy	Head and neck	Under investigation	Nanospectra Biosciences	In phase 1 clinical trials
Semiconductor						
Quantum dot	Qdots, EviTags, semiconductor nanocrystals	Fluorescent contrast, in vitro diagnostics	Tumors, cells, tissues, and molecular sensing structures	Not applicable	Life Technologies, eBioscience, Nanoco, CrystalPlex, Cytodiagnostics	Research use only
Organic						
Protein	Abraxane	Cancer therapy	Breast	Cytopenia	Abraxis Bioscience	FDA approved
Liposome	Doxil/Caelyx	Cancer therapy	Various forms	Hand–foot syndrome, stomatitis	Ortho Biotech	FDA approved
Polymer	Oncaspar	Cancer therapy	Acute lymphoblastic leukemia	Urticaria, rash	Rhône-Poulenc Rorer	FDA approved
	CALAA-01	Cancer therapy	Various forms	Mild renal toxicity	Calando	In phase 2 clinical trials
Dendrimer	VivaGel	Microbicide	Cervicovaginal	Abdominal pain, dysuria	Starpharma	In phase 2 clinical trials
Micelle	Genexol-PM	Cancer therapy	Various forms	Peripheral sensory neuropathy, neutropenia	Samyang	For phase 4 clinical trials

* MRI denotes magnetic resonance imaging.

Nanomedicine Technology Development Pipeline
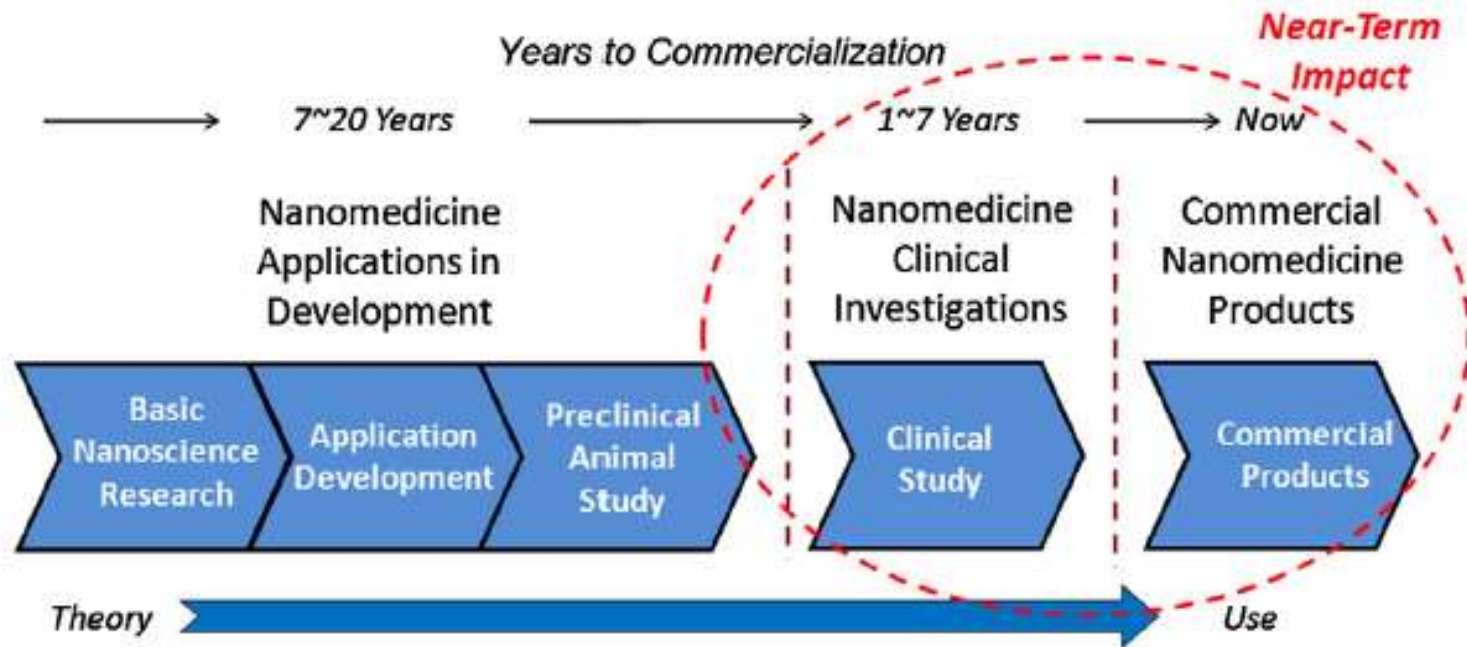
Gene Therapy

- Gene therapy is a technique for correcting defective genes responsible for disease development. Researchers may use one of several approaches for correcting faulty genes:

  - **A normal gene may be inserted into a nonspecific location within the genome to replace a nonfunctional gene. This approach is most common.**

  - **An abnormal gene could be swapped for a normal gene through homologous recombination.**

  - **The abnormal gene could be repaired through selective reverse mutation, which returns the gene to its normal function.**

  - **The regulation (the degree to which a gene is turned on or off) of a particular gene could be altered.**

How Gene Therapy Works?

- In most gene therapy studies, a "normal" gene is inserted into the genome to replace an "abnormal," disease-causing gene. A carrier molecule called a vector must be used to deliver the therapeutic gene to the patient's target cells. Currently, the most common vector is a virus that has been genetically altered to carry normal human DNA. Viruses have evolved a way of encapsulating and delivering their genes to human cells in a pathogenic manner. Scientists have tried to take advantage of this capability and manipulate the virus genome to remove disease-causing genes and insert therapeutic genes.

- Target cells such as the patient's liver or lung cells are infected with the viral vector. The vector then unloads its genetic material containing the therapeutic human gene into the target cell. The generation of a functional protein product from the therapeutic gene restores the target cell to a normal state.

Gene Delivery

- Transfection- the delivery of foreign molecules such as DNA and RNA into eukaryotic cells
- Naked DNA is not suitable for in-vivo transport of genetic materials-> degradation by serum nucleases
- Ideal gene delivery system
  - Biocompatible
  - Non-immunogenic
  - Stable in blood stream
  - Protect DNA during transport
  - Small enough to extravagate
  - Cell and tissue specific

Endocytosis

Endocytosis in Animal Cells
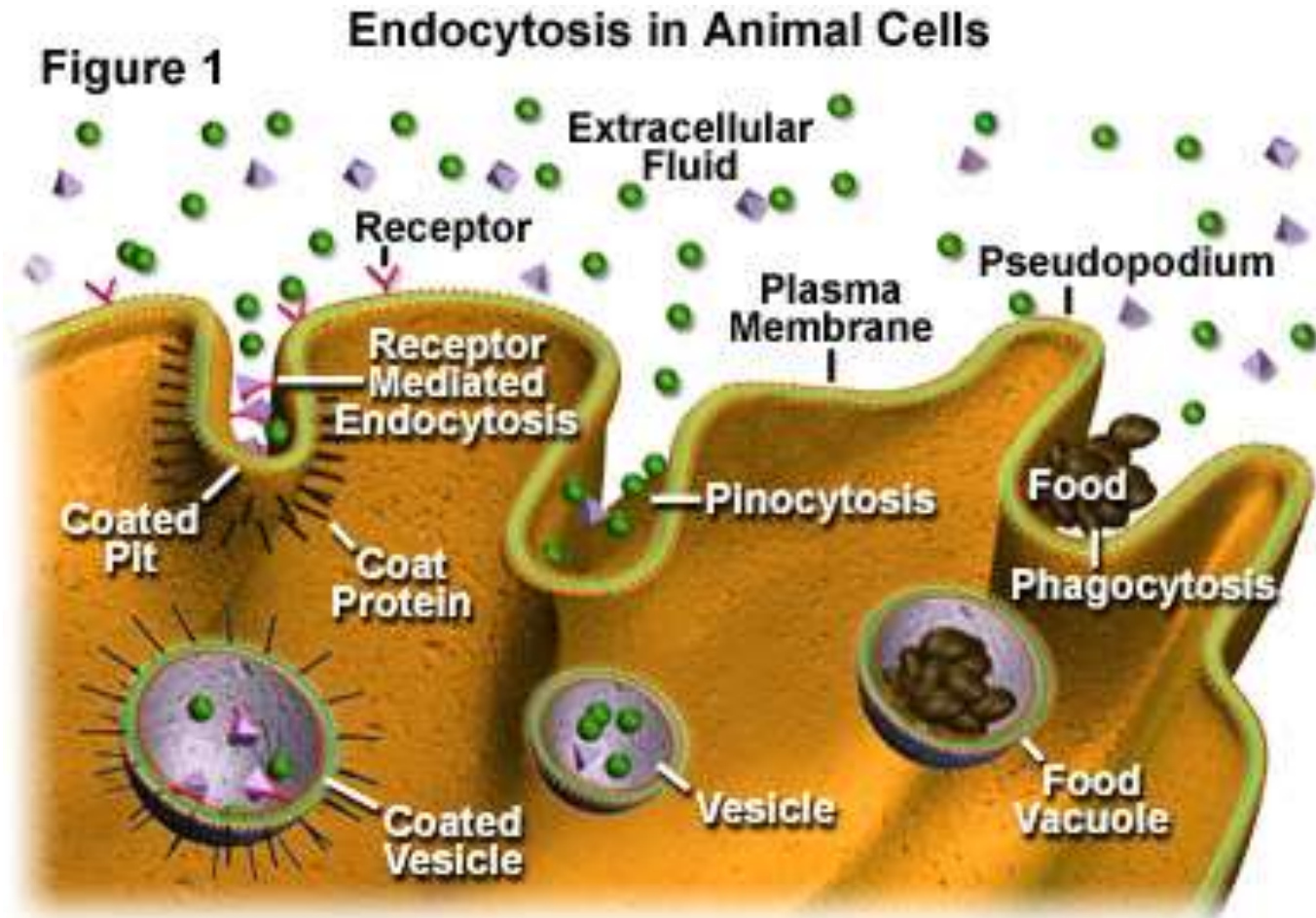
Figure 1

Endocytic pathway in mammalian cells
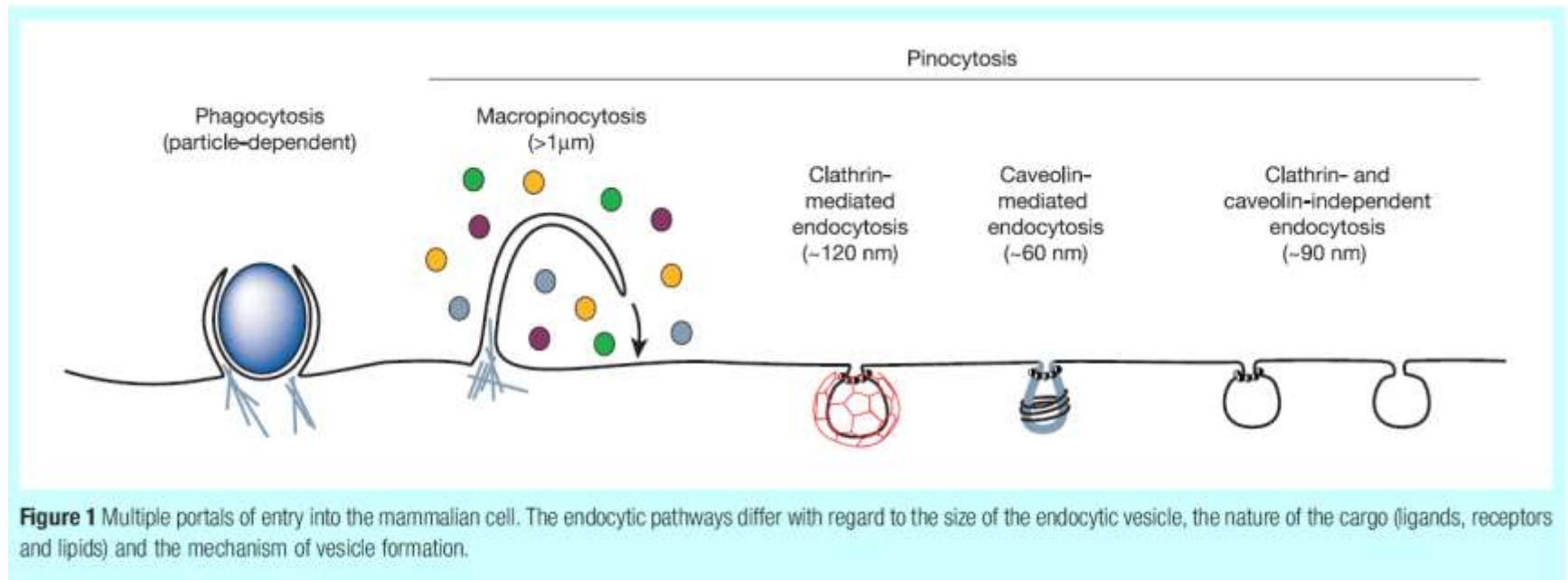
Figure 1 Multiple portals of entry into the mammalian cell. The endocytic pathways differ with regard to the size of the endocytic vesicle, the nature of the cargo (ligands, receptors and lipids) and the mechanism of vesicle formation.

Barrier to non-viral gene delivery
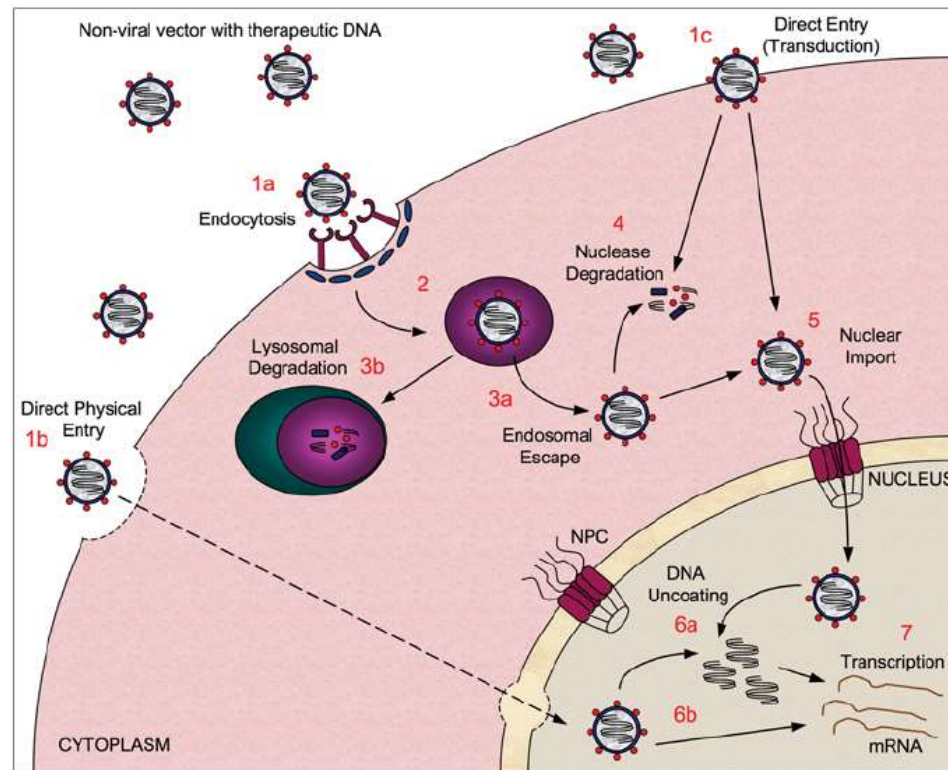
Figure 1   Barriers to non-viral gene delivery

Representation of the route travelled by a non-viral gene-delivery vector carrying therapeutic DNA to the nucleus. A non-viral vector, formed by interaction of the DNA with a carrier compound, must cross the plasma membrane to enter the cell. This can be via several routes, including endocytosis-based entry (1a), direct physical entry routes, such as electroporation or ballistic delivery (1b), or direct entry via protein transduction (1c). Depending on the mode of cellular entry, the vector may become encapsulated in an endosome (2), from which it must escape (3a) or it will become degraded when the endosome fuses with a lysosome (3b). The DNA will at some point be subjected to degradation by cytosolic nucleases (4), as it traverses through the cytoplasm to reach the nucleus. Finally, the vector must undergo nuclear transport (5) through NPCs embedded in the NE in order to gain access to the nucleoplasm. Once in the nucleus, the DNA may (6a) or may not (6b) need to be uncoated, depending upon the vector used, before it can ultimately be transcribed (7).

NLS-mediated nuclear import
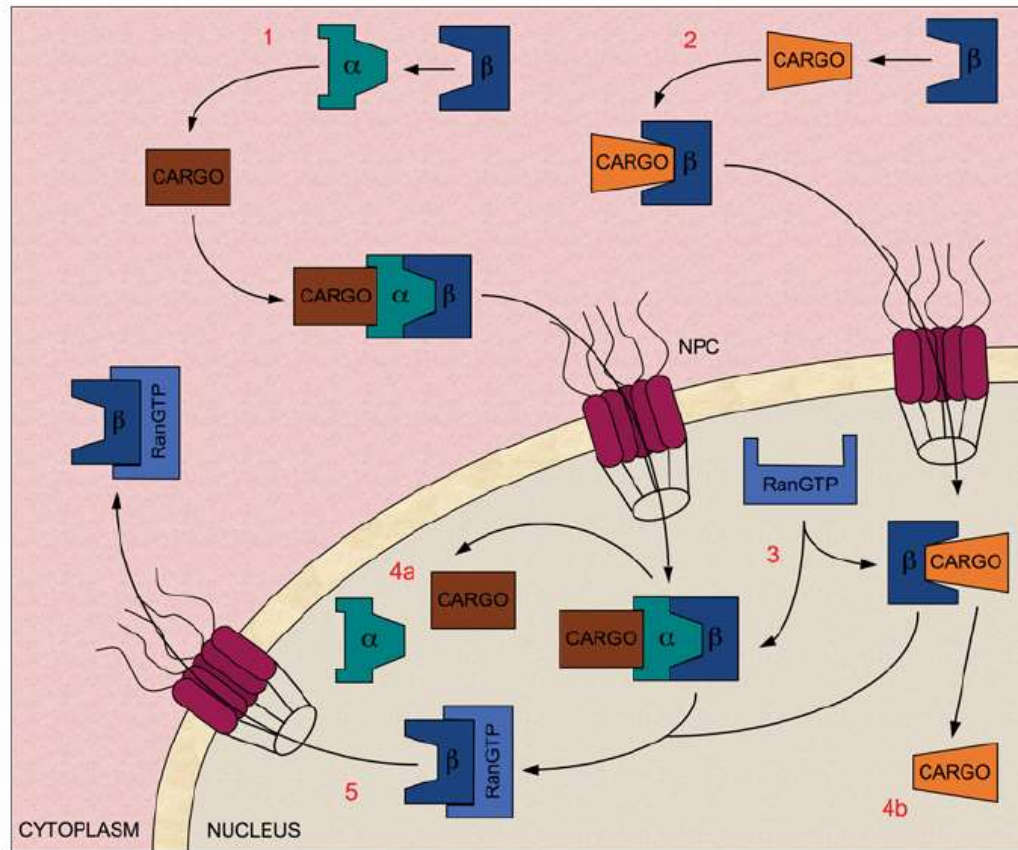
Figure 2 **NLS-mediated nuclear import pathways**

In classical nuclear import, the NLS found in cargo bound for the nucleus is recognized by the Imp α subunit of the Imp α/β heterodimer (1). However, there are also many examples where Imp β or one of its many homologues can mediate nuclear import or cargo proteins independently of Imp α (2). In both cases, transient interactions between the Imp β and the nucleoporin proteins that line the NE-embedded NPCs mediate translocation into the nucleus. Once inside, RanGTP binds to Imp β (3), releasing Imp α and the cargo into the nucleoplasm (4a and 4b). RanGTP itself is then recycled back to the cytoplasm (5), where it is converted into its RanGDP state (not shown). An animated version of this Figure can be found at http://www.BiochemJ.org/bj/406/0185/bj4060185add.htm

Barriers to DNA Delivery

A number of challenges and barriers face the successful delivery of therapeutic DNA to target cells in the body. Physicochemical, economic and sterilization challenges complicate formulation; the complex environment of the human body hinders its successful transport to the target cell population; and endocytic pathway barriers hinder its successful transport to the nucleus of the cell (the site of action). Each known and major barrier is listed in Fig. B1, using nanoscale DNA-delivery systems as representative examples. Each barrier exists independent of length scale. L = lysosome. A number of clever systems have been devised to overcome these barriers, the general design criteria of which are given in Tables B1 and B2.

Formulation level	Organism level	Cellular level

Barriers / challenges / needs

Formulation	Organism	Cellular
Economically viable	Prolonged circulation time	Transport to cell surface
FDA-approvable	Stability in blood circulation	Cellular internalization
Acceptable shelf-life	Access to target tissue/cells	Intracellular transport
	Elimination from body	Enzymatic degradation
	Mininal toxicity	Nuclear entry

Figure B1 Barriers to DNA delivery.

Organism Level

Barrier/challenge/need	Rationale	Example approaches	Materials design criteria
Prolonged circulation time	Maximize total flux past target cell type	PEG conjugates to minimize interaction with serum proteins	Hydrophilic
			Uncharged
Stability within blood circulation	Maintenance of designed functionality	Crosslinking to maximize overall stability	Stable crosslinks within bloodstream, but reversible upon entry into target cell
Access to target tissue/cells	Transport from capillary lumen to extracellular space to reach target cell surface	Vaso-active protein conjugates (for example, vascular endothelial growth factor)	Retention of protein activity post conjugation
		Targeting restricted to 'leaky' vessel tissues (for example, tumour, liver, spleen).	Small diameter delivery system (for example, <100 nm)
Elimination from body	Minimal build-up of delivery vector over time	Control over molecular weight	Filterable through kidneys
		Engineered biodegradation sites	Biodegradable
Minimal toxicity and immunogenicity	Safety over treatment duration and beyond that required for FDA-approval	Minimize cation density	Non-cytotoxic
		Avoid protein-based materials/conjugates	Non-immunogenic

| Barrier number (from Fig. B1)	Barrier/challenge/need	Example approaches	Materials design criteria
1, 2 and 3	Transport to cell surface, association with cell membrane, internalization	Receptor/ligand interaction (for example, antibody/polymer conjugates, recombinant protein–polymer fusions, carbohydrate conjugates) Non-specific interaction with cell surface (for example, positive zeta potential, lipid conjugates)	Cell-type specificity, low cross reactivity, if desired Promiscuous attachment, high cross reactivity, if desired (for example, positive zeta potential, lipid conjugation) Endocytic pathway trigger (for example, clathrin-dependent, clathrin-independent, caveolin-dependent)
4 and 5	Escape endosomal vesicle and avoid transport to lysosome	Buffering capacity between pH ~7.2 and ~5.0 Fusogenic peptide conjugate	Ability to disrupt endosomal membrane and/or fusion of endosome with lysosome
6	Transport through cytosol to perinuclear space with minimal degradation	'Higher' molecular weight to maintain complex stability within cytosol	Thermodynamic and kinetic stability of complex within cytosol Minimize DNA degradation within cytosol
7	Separation of complex to allow nuclear translocation	Hydrolytically or reductively degradable polymers to reduce molecular weight	'Triggered' degradation of polymer to reduce thermodynamic and kinetic stability of complex. Release of intact DNA at or near nuclear envelope
8	Nuclear entry	Nuclear localization sequence conjugates Mitosis	Facilitate nuclear uptake of DNA using virus-derived signals Facilitate nuclear uptake during mitosis when the nuclear envelope is dissolved.

CRISPR CAS9

CRISPRs (**clustered regularly interspaced short palindromic repeats**) are segments of prokaryotic DNA containing short repetitions of base sequences. Each repetition is followed by short segments of "spacer DNA" from previous exposures to a bacterial virus or

Movie

- https://youtu.be/2pp17E4E-O8
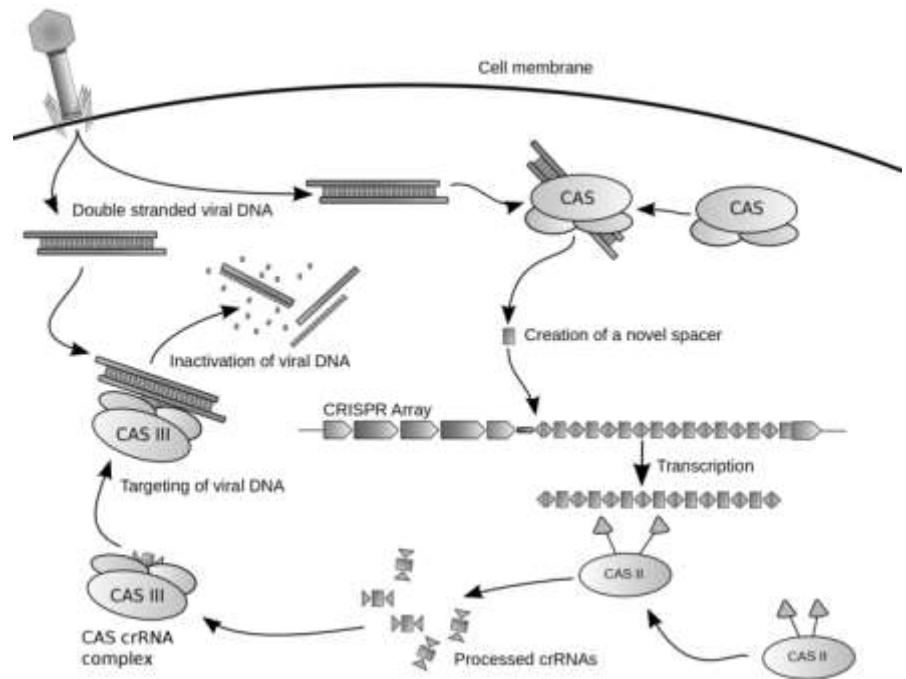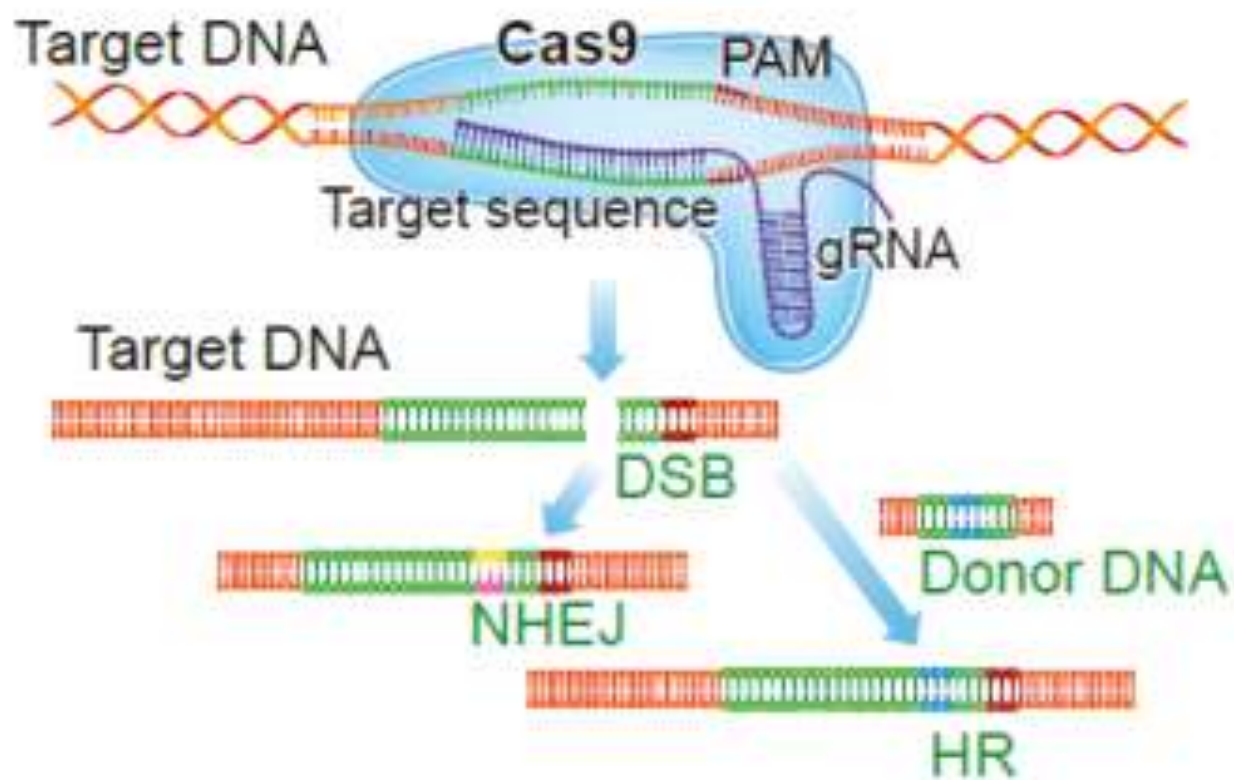
CANCER NANOTECHNOLOGY: OPPORTUNITIES AND CHALLENGES
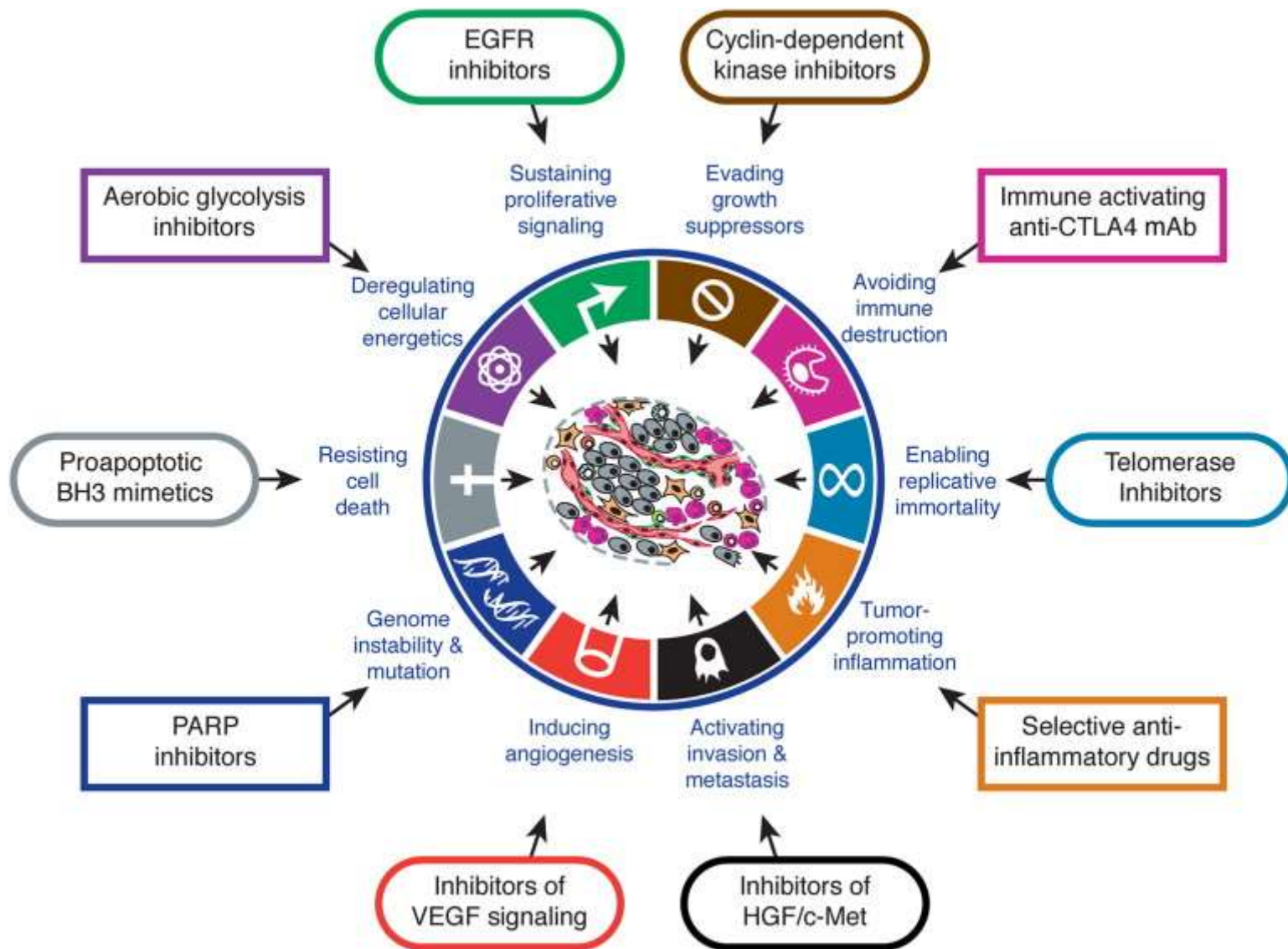
Summary

- Nanotechnology concerns the study of devices that are themselves or have essential components in the 1–1,000 nm dimensional range (that is, from a few atoms to subcellular size).

- Two main subfields of nanotechnology are nanovectors — for the administration of targeted therapeutic and imaging moieties — and the precise patterning of surfaces.

- Nanotechnology is no stranger to oncology: liposomes are early examples of cancer nanotherapeutics, and nanoscale-targeted magnetic resonance imaging contrast agents illustrate the application of nanotechnology to diagnostics.

- Photolithography is a light-directed surface-patterning method, which is the technological foundation of microarrays and the surface-enhanced laser desorption/ionization time-of-flight approach to proteomics. Nanoscale resolution is now possible with photolithography, and will give rise to instruments that can pack a much greater density of information than current biochips.

- The ability of nanotechnology to yield advances in early detection, diagnostics, prognostics and the selection of therapeutic strategies is predicated based on its ability to 'multiplex' — that is, to detect a broad multiplicity of molecular signals and biomarkers in real time. Prime examples of multiplexing detection nanotechnologies are arrays of nanocantilevers, nanowires and nanotubes.

- Multifunctionality is the fundamental advantage of nanovectors for the cancer-specific delivery of therapeutic and imaging agents. Primary functionalities include the avoidance of biobarriers and biomarker-based targeting, and the reporting of therapeutic efficacy.

- Thousands of nanovectors are currently under study. By systematically combining them with preferred therapeutic and biological targeting moieties it might be possible to obtain a very large number of novel, personalized therapeutic agents.

- Novel mathematical models are needed, in order to secure the full import of nanotechnology into oncology.

Cancer Hallmark
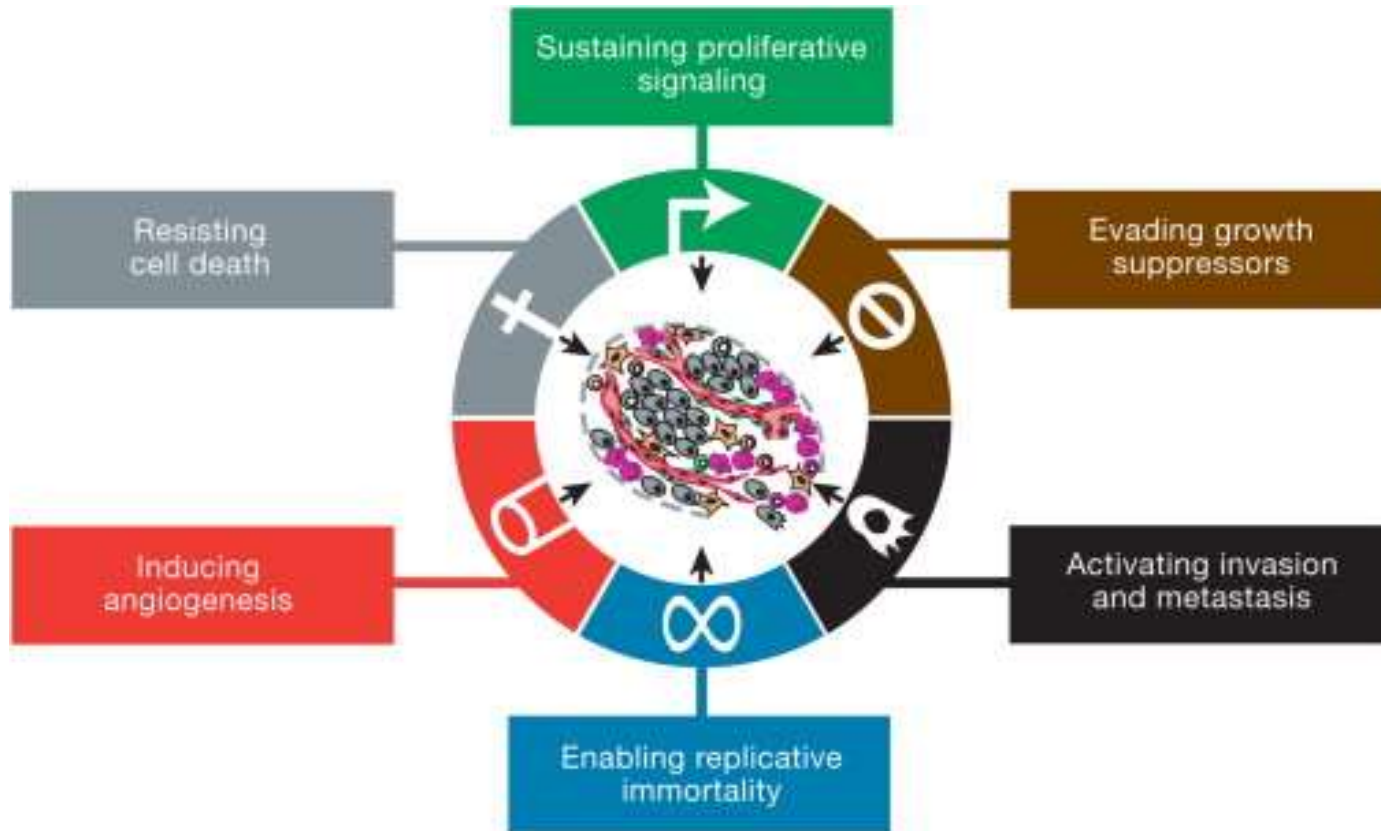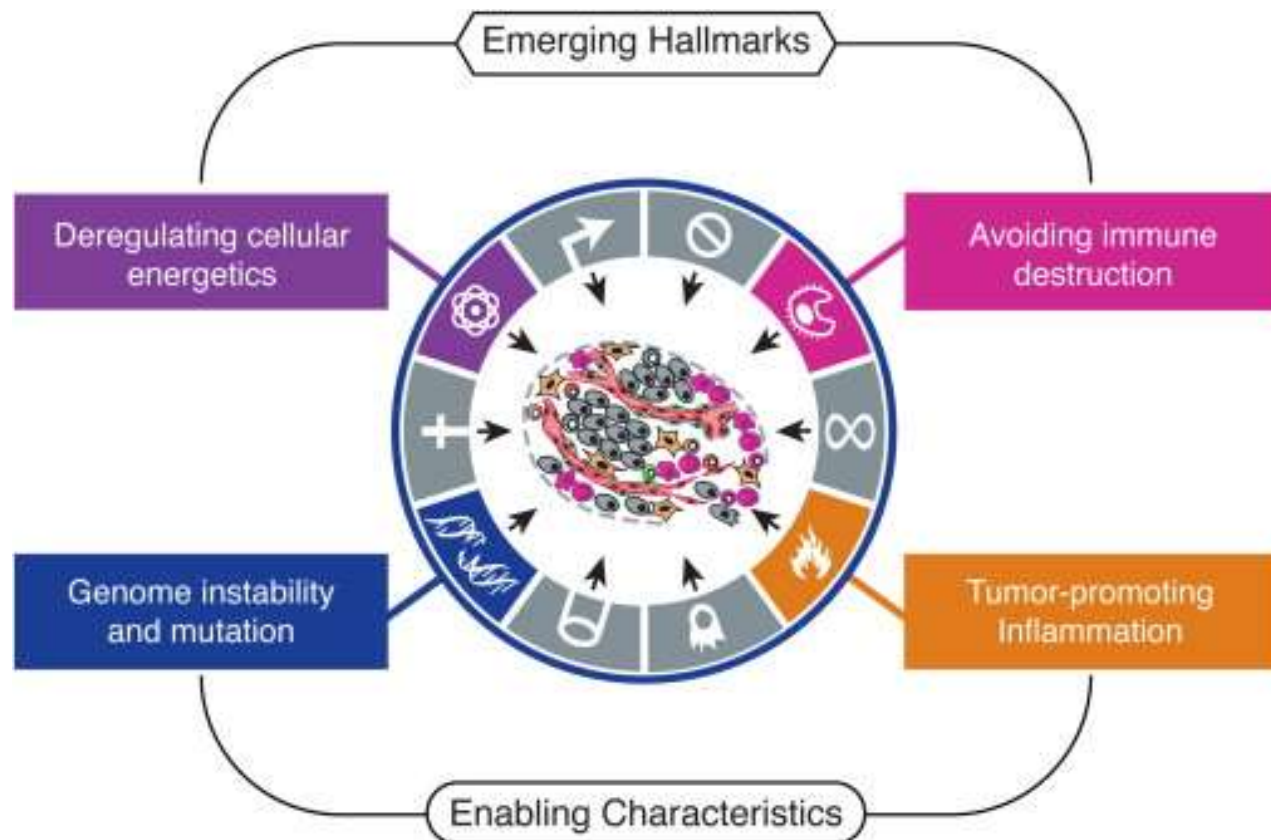
An increasing body of research suggests that two additional hallmarks of cancer are involved in the pathogenesis of some and perhaps all cancers. One involves the capability to modify, or reprogram, cellular metabolism in order to most effectively support neoplastic proliferation. The second allows cancer cells to evade immunological destruction, in particular by T and B lymphocytes, macrophages, and natural killer cells. Because neither capability is yet generalized and fully validated, they are labeled as emerging hallmarks. Additionally, two consequential characteristics of neoplasia facilitate acquisition of both core and emerging hallmarks. Genomic instability and thus mutability endow cancer cells with genetic alterations that drive tumor progression. Inflammation by innate immune cells designed to fight infections and heal wounds can instead result in their inadvertent support of multiple hallmark capabilities, thereby manifesting the now widely appreciated tumor-promoting consequences of inflammatory responses.

EGFR inhibitors

Cyclin-dependent kinase inhibitors

Aerobic glycolysis inhibitors

Immune activating anti-CTLA4 mAb

Sustaining proliferative signaling

Evading growth suppressors

Deregulating cellular energetics

Avoiding immune destruction

Proapoptotic BH3 mimetics

Telomerase Inhibitors

Resisting cell death

Enabling replicative immortality

PARP inhibitors

Selective anti-inflammatory drugs

Genome instability & mutation

Tumor-promoting inflammation

Inhibitors of VEGF signaling

Inhibitors of HGF/c-Met

Inducing angiogenesis

Activating invasion & metastasis

Figure 4 | **Multicomponent targeting strategies.** Nanoparticles extravasate into the tumour stroma through the fenestrations of the angiogenic vasculature, demonstrating targeting by enhanced permeation and retention. The particles carry multiple antibodies, which further target them to epitopes on cancer cells, and direct antitumour action. Nanoparticles are activated and release their cytotoxic action when irradiated by external energy. Not shown: nanoparticles might preferentially adhere to cancer neovasculature and cause it to collapse, providing anti-angiogenic therapy. The red blood cells are not shown to scale; the volume occupied by a red blood cell would suffice to host 1–10 million nanoparticles of 10 nm diameter.

a
- Blood vessel
- Nanoparticle
- Neovascular endothelium
- Tumour stroma
- Permeation enhancer e.g. MMP9

b
- Molecular motor molecule e.g. actin
- Actin filaments

c
- Therapeutic agent bound to myosin
- Tumour cell
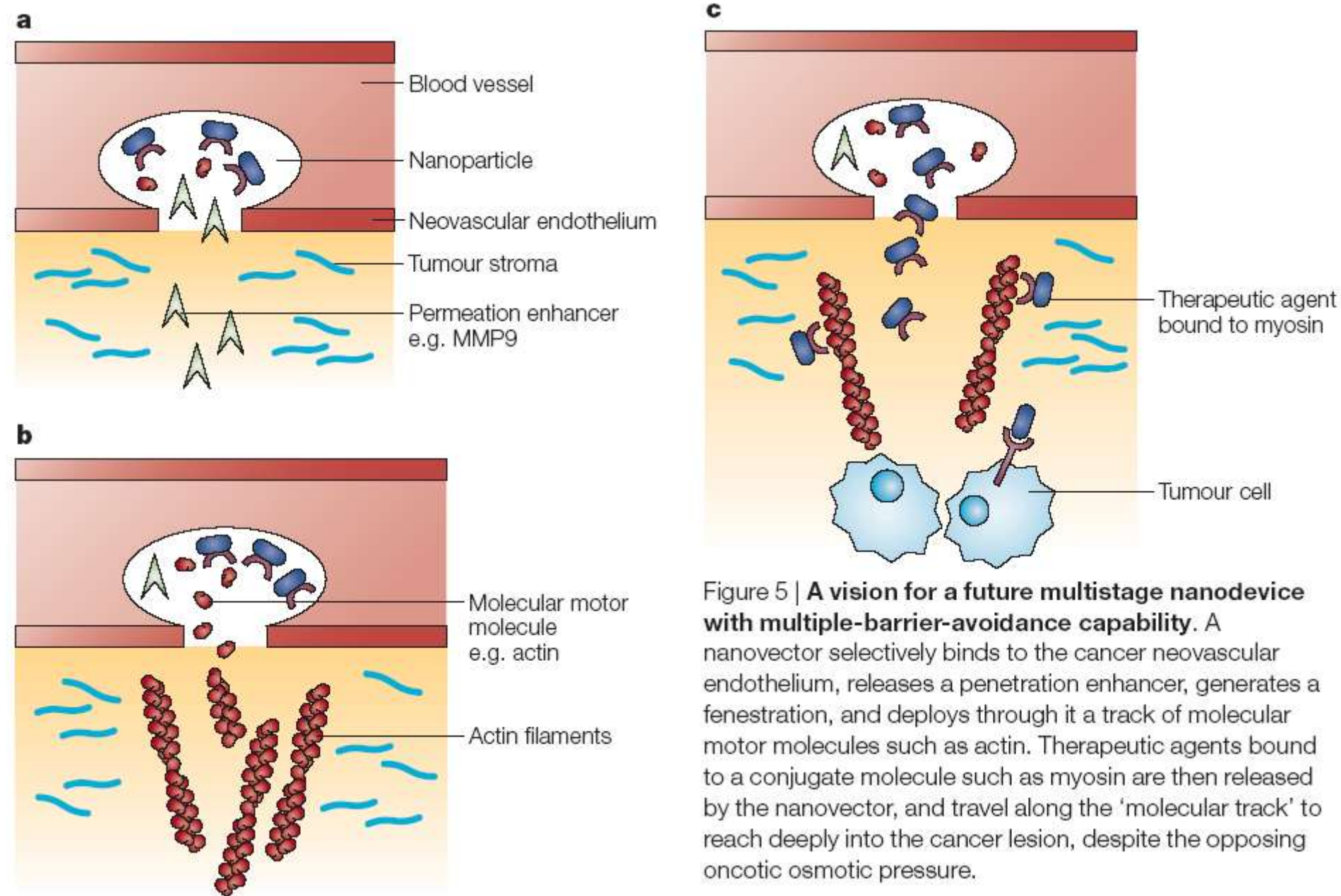
Figure 5 | **A vision for a future multistage nanodevice with multiple-barrier-avoidance capability**. A nanovector selectively binds to the cancer neovascular endothelium, releases a penetration enhancer, generates a fenestration, and deploys through it a track of molecular motor molecules such as actin. Therapeutic agents bound to a conjugate molecule such as myosin are then released by the nanovector, and travel along the 'molecular track' to reach deeply into the cancer lesion, despite the opposing oncotic osmotic pressure.

Polymer conjugates as anticancer nanomedicines

At a glance

- Water-soluble polymers conjugated to proteins and anticancer drugs are in routine clinical use and clinical development as both single agents and components of combination therapy. This is establishing polymer therapeutics as one of the first classes of anticancer nanomedicine. There is growing optimism about the use of ever more sophisticated polymer-based vectors for cancer therapy.

- The covalent conjugation of synthetic polymers, particularly poly(ethyleneglycol) (PEG), to protein drugs increases their plasma residence, reduces protein immunogenicity and can increase their therapeutic index. Several PEGylated enzymes (such as L-asparaginase) and cytokines (including interferon-α and granulocyte colony-stimulating factor) have now entered routine clinical use.

- Polymer conjugation alters the biodistribution of low-molecular-weight drugs, enabling tumour-specific targeting with reduced access to sites of toxicity. More than ten polymer–anti-tumour conjugates have been transferred into clinical development. They have been designed for lysosomotropic delivery following passive tumour targeting by the enhanced permeability and retention effect (EPR effect) or, in one case, for receptor-mediated targeting by the introduction of a cell-specific ligand. Polyglutamic acid–paclitaxel is showing particular promise in phase III trials in women with non-small-cell lung cancer.

- New strategies are making polymer conjugates active against new molecular targets (for example, anti-angiogenics), and the combination of polymer conjugates with low-molecular-weight drugs (which are routinely used in chemotherapy), radiotherapy or tailor-made prodrugs is showing promise. Moreover, the polymer platform provides an ideal opportunity to deliver a drug combination from a single carrier, and combined endocrine therapy and chemotherapy is showing preclincal potential as a breast cancer therapy.

- The polymers that have been used clinically so far have a linear polymer architecture. The principles for the design of polymer therapeutics are now being applied to new hyperbranched dendrimers and dendritic polymer architectures. Before clinical evaluation it is essential to establish the safety of new polymers, particularly in respect of general toxicity, immunogenicity and metabolic fate.

Box 1 | **Rationale for design of PEG–protein conjugates**

Recombinant DNA and monoclonal antibody technology has created a growing number of peptide, protein and antibody-based drugs. The conjugation of poly(ethyleneglycol) (PEG) to proteins (PEGylation) is proving a useful tool to:

- Increase protein solubility and stability, and also to reduce protein immunogenicity[29,30].
- Prevent the rapid renal clearance of small proteins and receptor-mediated protein uptake by cells of the reticuloendothelial (RES) system.
- Prolong plasma half-life — leading to the need for less frequent dosing, which is of great patient benefit.

Although several water-soluble polymers have been successfully used for protein conjugation, PEG is particularly attractive because:

- PEG is used as a pharmaceutical excipient and is known to be non-toxic and non-immunogenic.
- PEG has a flexible, highly water-soluble chain that extends to give a hydrodynamic radius some 5–10 times greater than that of a globular protein of equivalent molecular weight. Its high degree of hydration means the polymer chain effectively has a 'water shell', and this helps to mask the protein to which it is bound.
- PEG can be prepared with a single reactive group at one terminal end, and this aids site-specific conjugation to a protein and avoids protein crosslinking during conjugation.

Although first generation protein conjugates were synthesized using linear monomethoxyPEGs (molecular weight (Mw) of ~5,000 g mol^{-1}), with many polymer chains randomly attached to each protein molecule, various sophisticated conjugation chemistries have now emerged that use linear or branched PEGs of Mw ~5,000–40,000 g mol^{-1}. Several techniques, most recently including phage display, enable site-specific peptide and protein modification. The specific linking chemistries and synthetic strategies being used are described in more detail elsewhere[29,30,44,45].

## Box 2 | Rationale for the design of polymer–drug conjugates

Ringsdorf's vision of the idealized polymer chemistry for drug conjugation[67] and Trouet and De Duve's realization that the endocytic pathway might be useful for lysosomotropic drug delivery[156] led to the concept of targetable anticancer polymer–drug conjugates. Low-molecular-weight anticancer agents typically distribute randomly throughout the body, and this often leads to side effects. The attachment of drugs to polymeric carriers can:

- Limit cellular uptake to the endocytic route.
- Produce long-circulating conjugates. Most of the dose of low-molecular-weight drug typically leaves the circulation within minutes, whereas a polymer conjugate will ideally circulate for several hours to facilitate passive tumour targeting caused by the leakiness of angiogenic tumour blood vessels by the enhanced permeability and retention effect (EPR effect)[39]. Conjugates have also been synthesized to contain targeting ligands (such as antibodies, peptides and sugars) with the aim of further promoting increased (building on the EPR effect) tumour targeting by receptor-mediated delivery[26,28].

Several features are needed for the effective design of polymer–drug conjugates:

- The polymer must be non-toxic and non-immunogenic. It must also be suitable for industrial-scale manufacture. Polymer molecular weight should be high enough to ensure long circulation, but for non-biodegradable polymeric carriers this molecular weight (Mw) must be less than 40,000 g mol^{-1} to enable the renal elimination of the carrier following drug delivery. Therefore, the optimum (usually Mw 30,000–100,000 g mol^{-1}) must be tailored to suit the particular polymer being used.
- The poymer must be able to carry an adequate drug payload in relation to its potency.
- The polymer–drug linker must be stable during transport to the tumour, but able to release the drug at an optimum rate on arrival within tumour cells.
- If the drug exerts its effects through an intracellular pharmacological receptor, access to the correct intracellular compartment is essential. Peptidyl and ester polymer–drug linkers have been widely used. In particular, peptide sequences designed for cleavage by the lysosomal thiol-dependent protease cathepsin B[81,82], but pH-sensitive cis-aconityl, hydrazone and acetal linkages have also been used[157]. They are hydrolysed within endosomal and lysosomal vesicles because of the local acidic pH (6.5–4.0). The ideal rate of release will vary according to the mechanism of action of the drug being delivered. Typically, conjugates containing doxorubicin linked by Gly-Phe-Leu-Gly release the drug payload over 24–48 h.
- The intracellular delivery and transfer of a drug out of the endosomal or lysosomal compartment is in many cases not only essential for therapeutic activity[158], it also provides the opportunity to bypass mechanisms of drug resistance that are reliant on membrane efflux pumps such as p-glycoprotein[159]. The limitation of polymer Mw to <100,000 g mol^{-1} ensures that the conjugate will be small enough to extravasate easily into the tumour, and will enable endocytic internalization by all types of tumour cell.
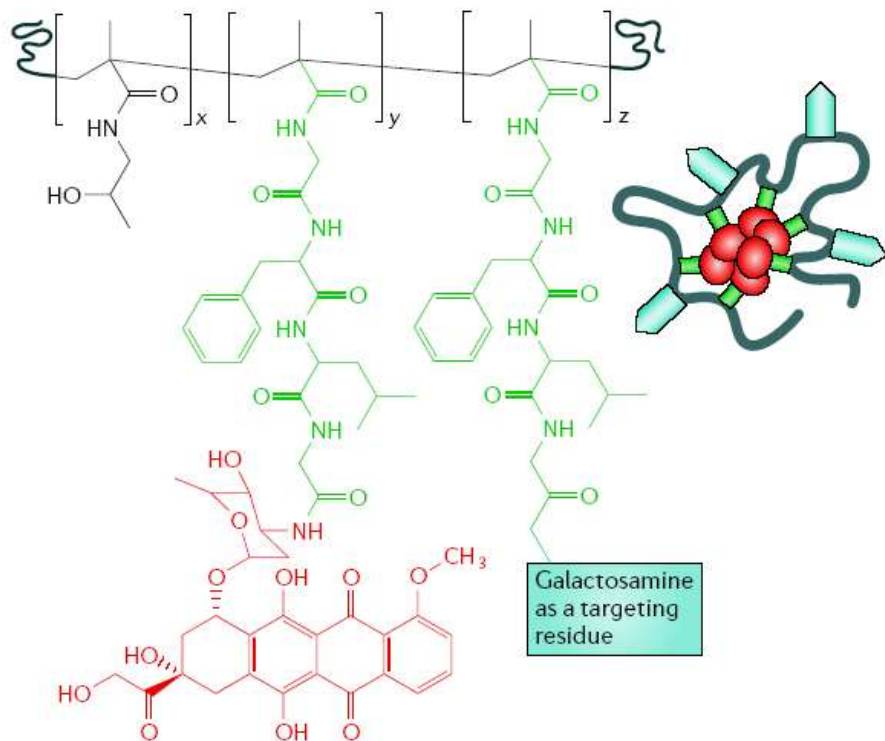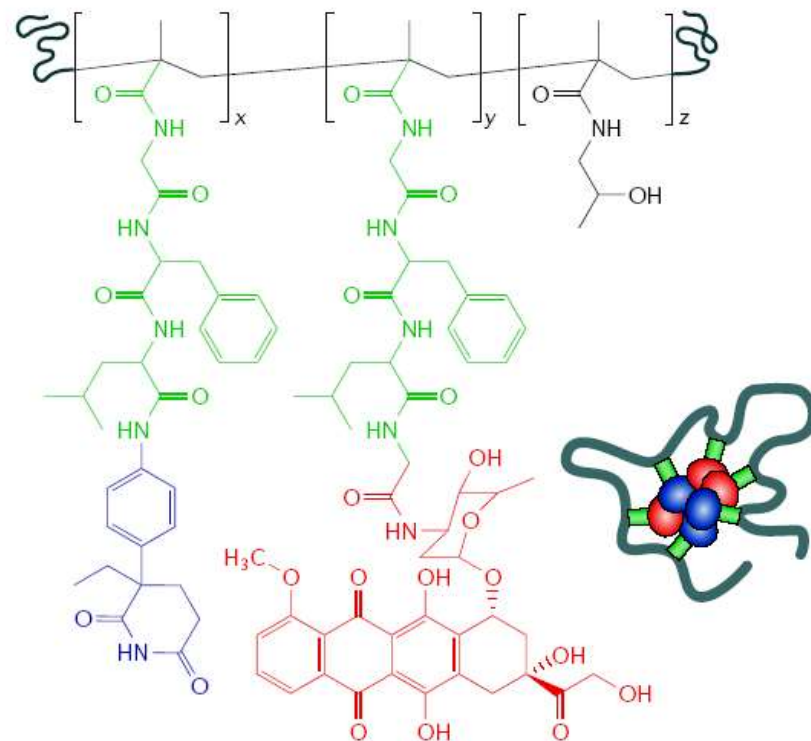
a Polymer–drug conjugate
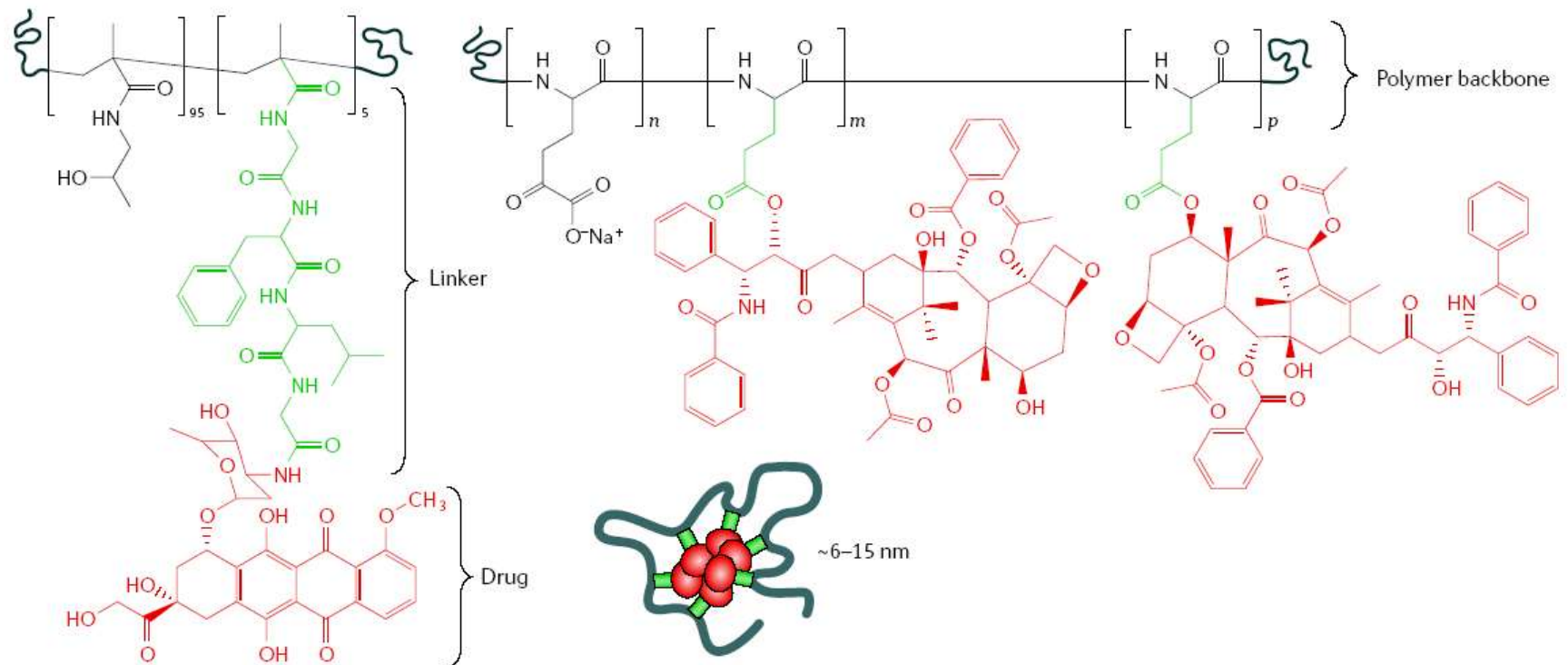
b Targeted conjugate

c Polymeric combination therapy

Galactosamine as a targeting residue

Figure 1 | **Polymer–anticancer drug conjugates**. Each panel shows both the detailed chemical structure and a cartoon of the general structure. The polymer backbone is shown in black, linker region in green, drug in red and additional components (for example, a targeting residue) in blue. **a** | Two examples of more 'simple' polymer–drug conjugates containing doxorubicin (left) and paclitaxel (right) that have progressed to clinical trial. **b** | A multivalent receptor-targeted conjugate containing galactosamine (light blue) to promote liver targeting. **c** | Polymer combination therapy containing the aromatase inhibitor aminogluthethimide (red) and doxorubicin (blue).
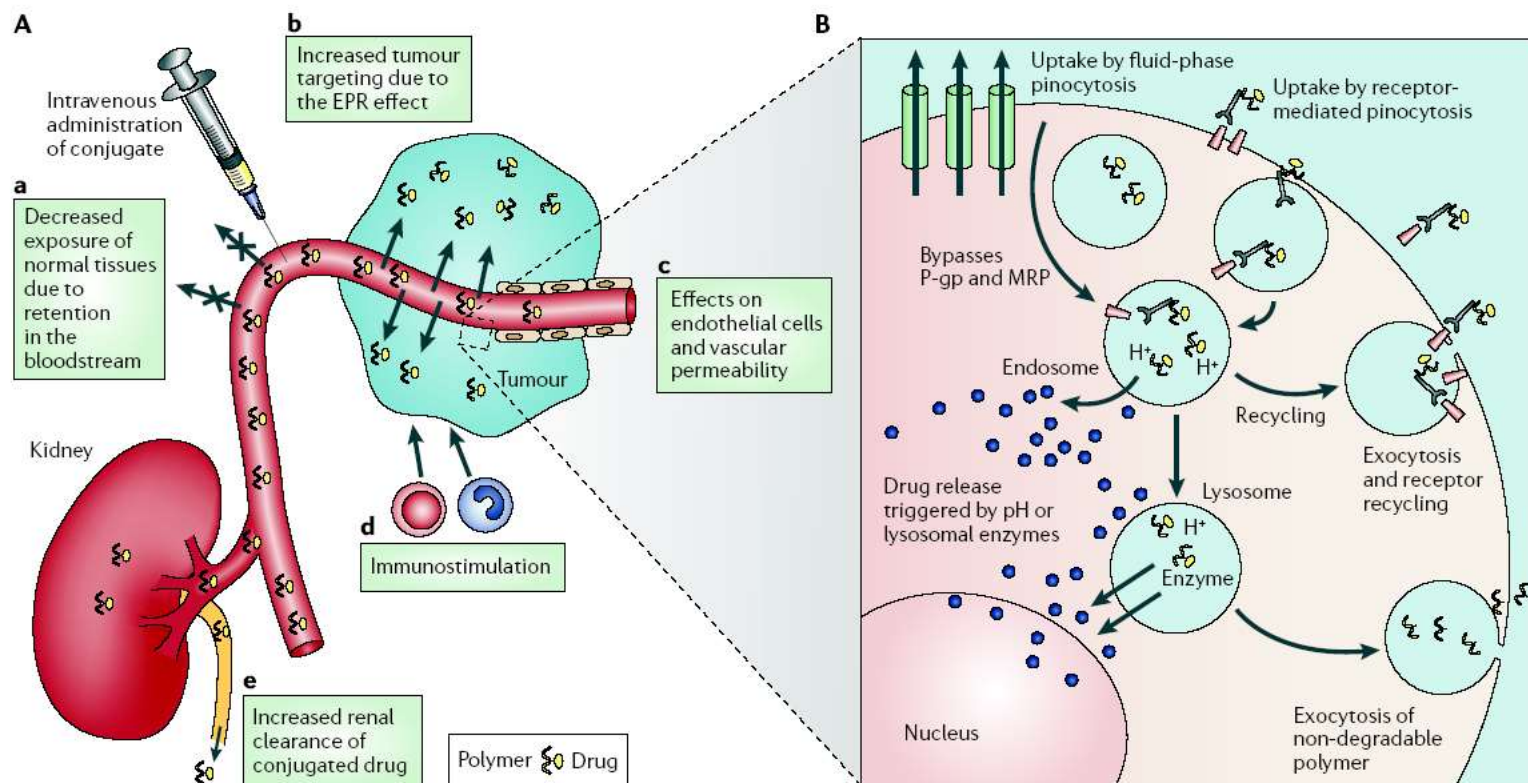
Figure 2 | **Current understanding of the mechanism of action of polymer–drug conjugates. A** | Hydrophilic polymer–drug conjugates administered intravenously can be designed to remain in the circulation — their clearance rate depends on conjugate molecular weight, which governs the rate of renal elimination. **a** | Drug that is covalently bound by a linker that is stable in the circulation is largely prevented from accessing normal tissues (including sites of potential toxicity), and biodistribution is initially limited to the blood pool. **b** | The blood concentration of drug conjugate drives tumour targeting due to the increased permeability of angiogenic tumour vasculature (compared with normal vessels), providing the opportunity for passive targeting due to the enhanced permeability and retention effect (EPR effect). **c** | Through the incorporation of cell-specific recognition ligands it is possible to bring about the added benefit of receptor-mediated targeting of tumour cells. **d** | It has also been suggested that circulating low levels of conjugate (slow drug release) might additionally lead to immunostimulation. **e** | If the polymer–drug linker is stable in the circulation, for example, N-(2-hydroxypropyl)methacrylamide (HPMA) copolymer–Gly-Phe-Leu-Gly–doxorubicin, the relatively high level of renal elimination (whole body $t_{1/2}$ clearance >50% in 24 h) compared with free drug ($t_{1/2}$ clearance ~50% in 4 days) can increase the elimination rate. **B** | On arrival in the tumour interstitium, polymer-conjugated drug is internalized by tumour cells through either fluid-phase pinocytosis (in solution), receptor-mediated pinocytosis following non-specific membrane binding (due to hydrophobic or charge interactions) or ligand–receptor docking. Depending on the linkers used, the drug will usually be released intracellularly on exposure to lysosomal enzymes (for example, Gly-Phe-Leu-Gly and polyglutamic acid (PGA) are cleaved by cathepsin B) or lower pH (for example, a hydrazone linker degrades in endosomes and lysosomes (pH 6.5–<4.0). The active or passive transport of drugs such as doxorubicin and paclitaxel out of these vesicular compartments ensures exposure to their pharmacological targets. Intracellular delivery can bypass mechanisms of resistance associated with membrane efflux pumps such as p-glycoprotein. If >10-fold, EPR-mediated targeting will also enable the circumvention of other mechanisms of drug resistance. Non-biodegradable polymeric platforms must eventually be eliminated from the cell by exocytosis. Rapid exocytic elimination of the conjugated drug before release would be detrimental and prevent access to the therapeutic target. In general, polymeric carriers do not access the cytosol. MRP, multidrug resistance protein.
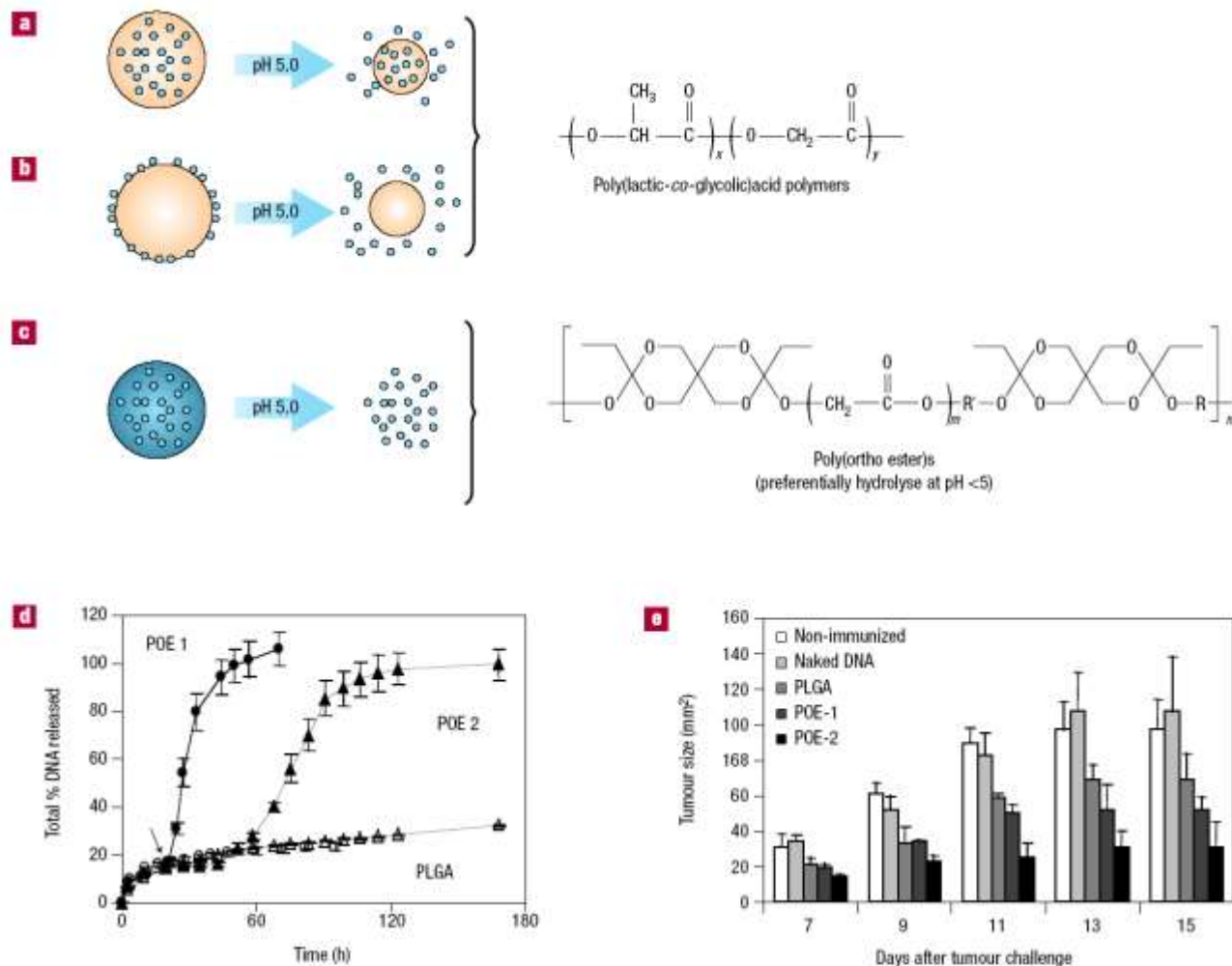
Figure 4 Degradation of polymeric microspheres as a function of pH. Microspheres <10 micrometres in diameter are preferentially internalized by APCs, providing a mechanism by which to target vaccines to the immune system. Following internalization by APCs, the spheres are sequestered within acidic vesicles, providing a mechanism through which to modulate the release of encapsulated DNA intracelluarly. **a**, Poly(lactic-*co*-glycolic)acid (PLGA) microspheres degrade relatively independent of the extracellular and acidic vesicle pH and release DNA as a function of polymer degradation. **b**, DNA adsorbed to the surface of PLGA-based microspheres release DNA more quantitatively than encapsulated DNA, but relatively independent of pH. **c**, Poly(orthoesters) degrade more rapidly at pH ~5.0, allowing triggered release of the DNA in the acidic environment of the phagosome. **d**, The pH-sensitive release of plasmid DNA from microspheres comprised of poly(orthoesters) (POE-1 and POE-2) described in ref. 63 and the pH-independent release of plasmid DNA from PLGA-based microspheres. The arrow shows the time at which the pH was changed from 7.4 to 5.0. The error bars represent the standard deviations over three samples. **e**, The influence that different DNA release kinetics can have on the efficacy of an anticancer DNA-therapeutic (adapted from ref. 63). The error bars represent the standard error from the average over five samples.
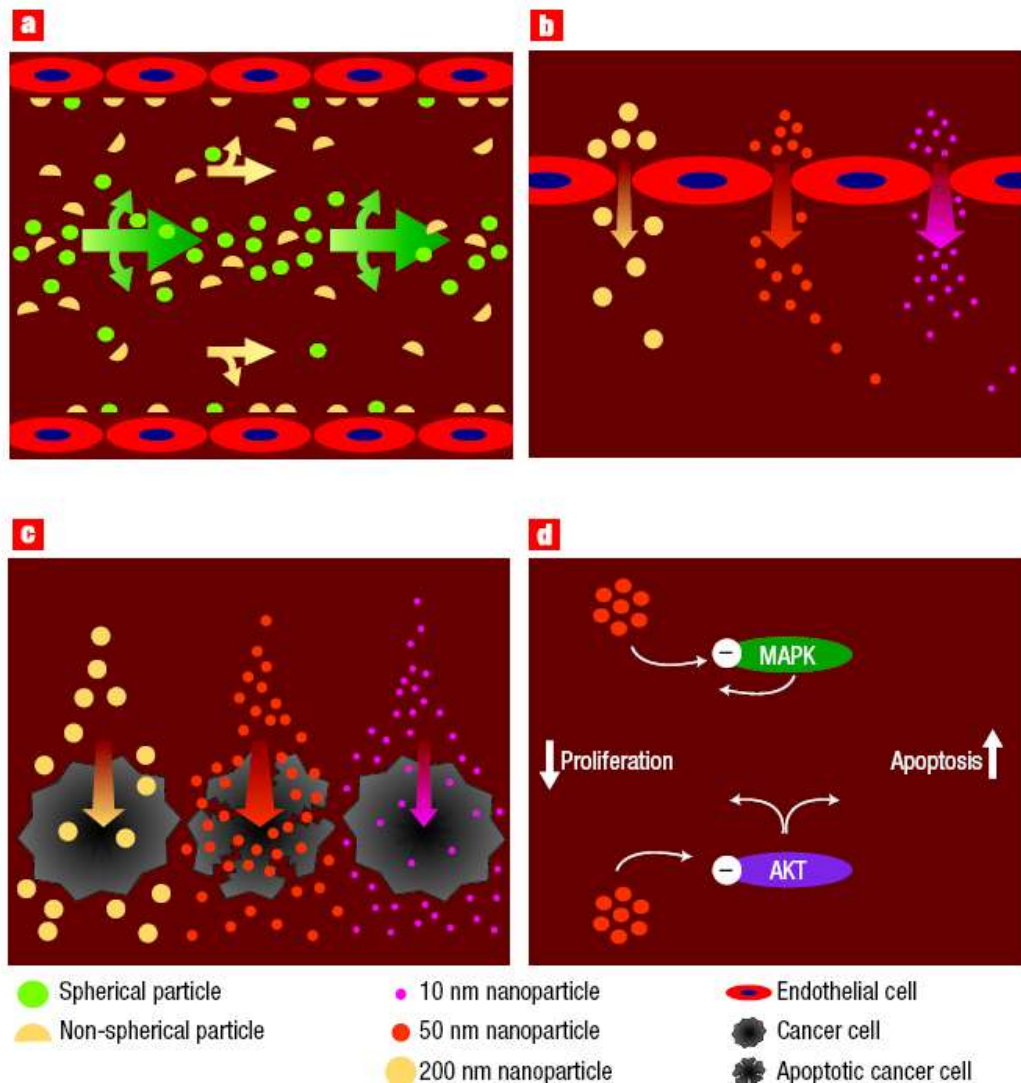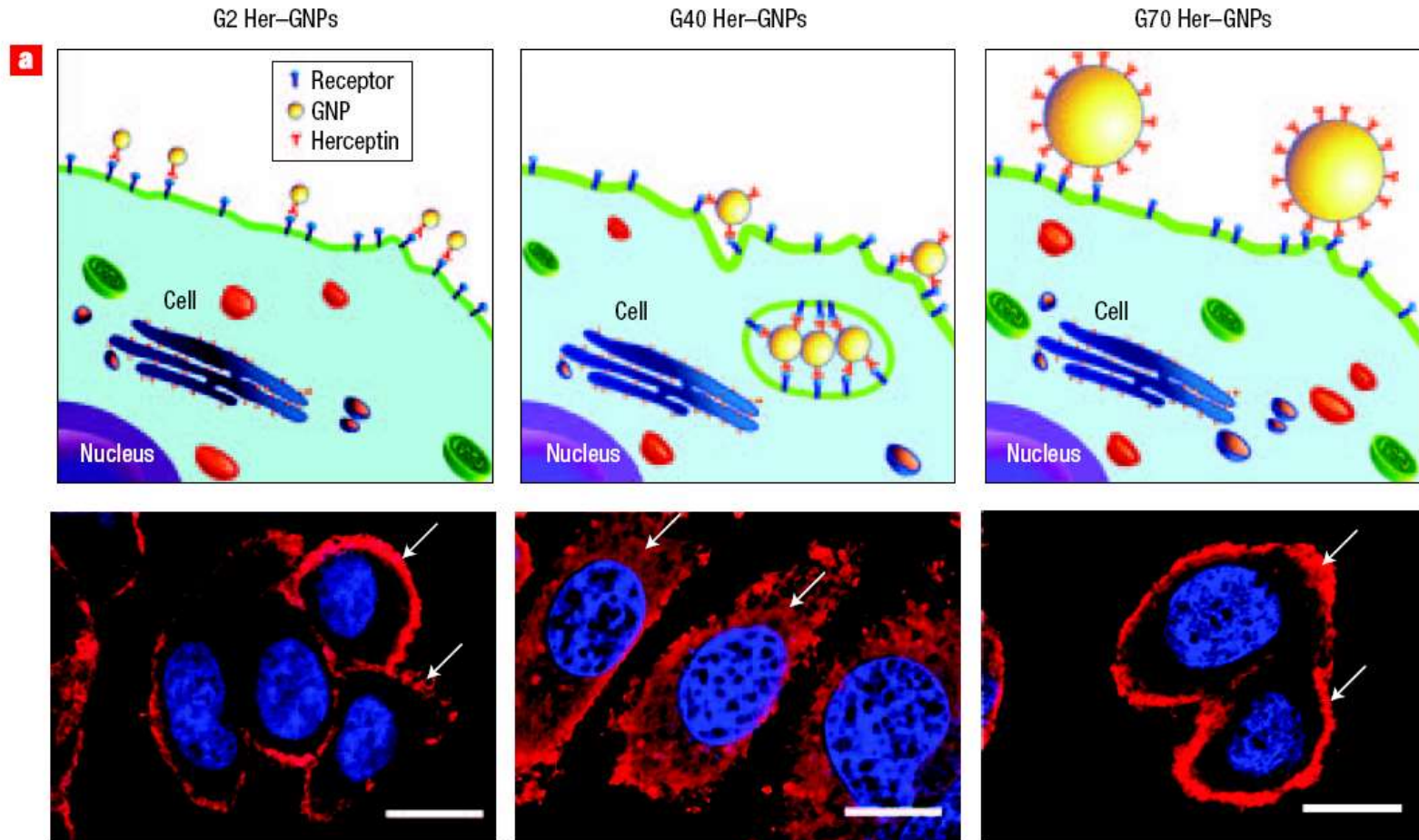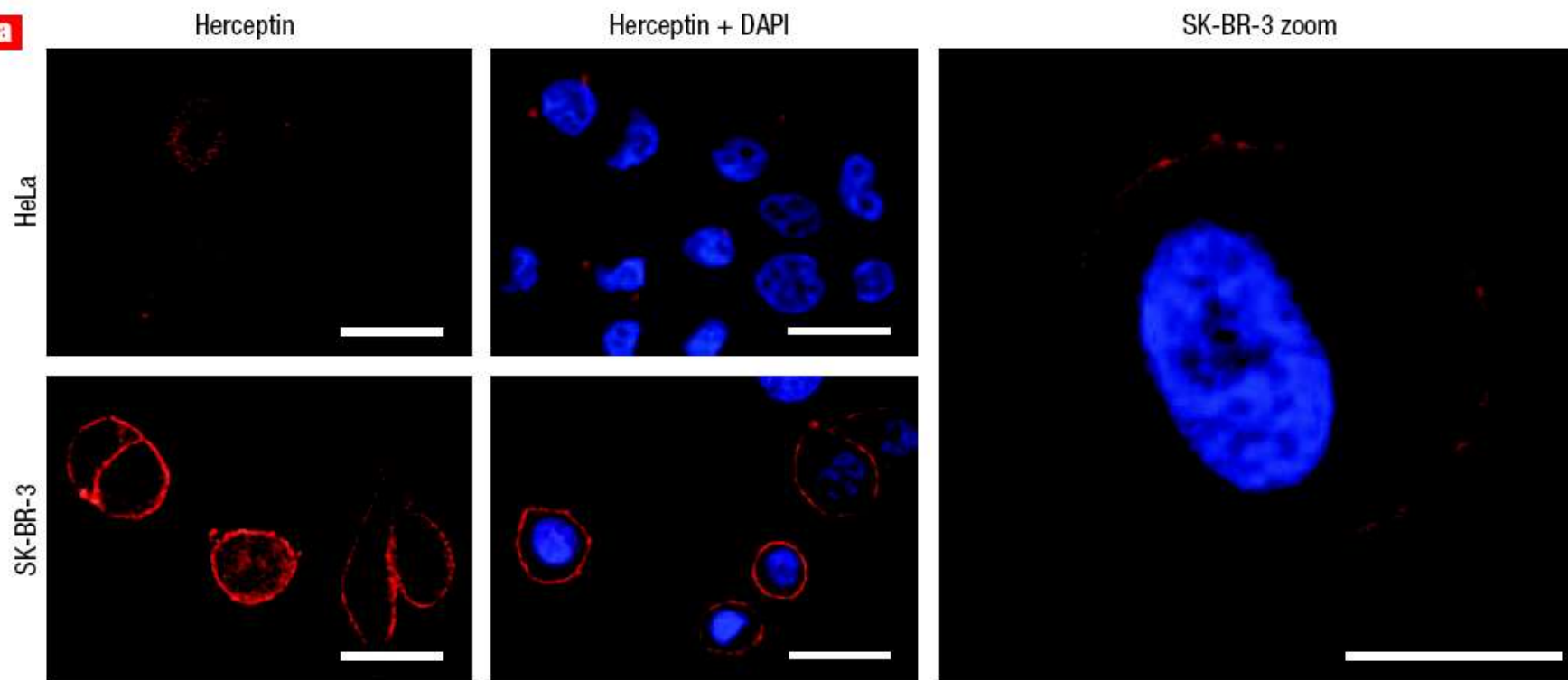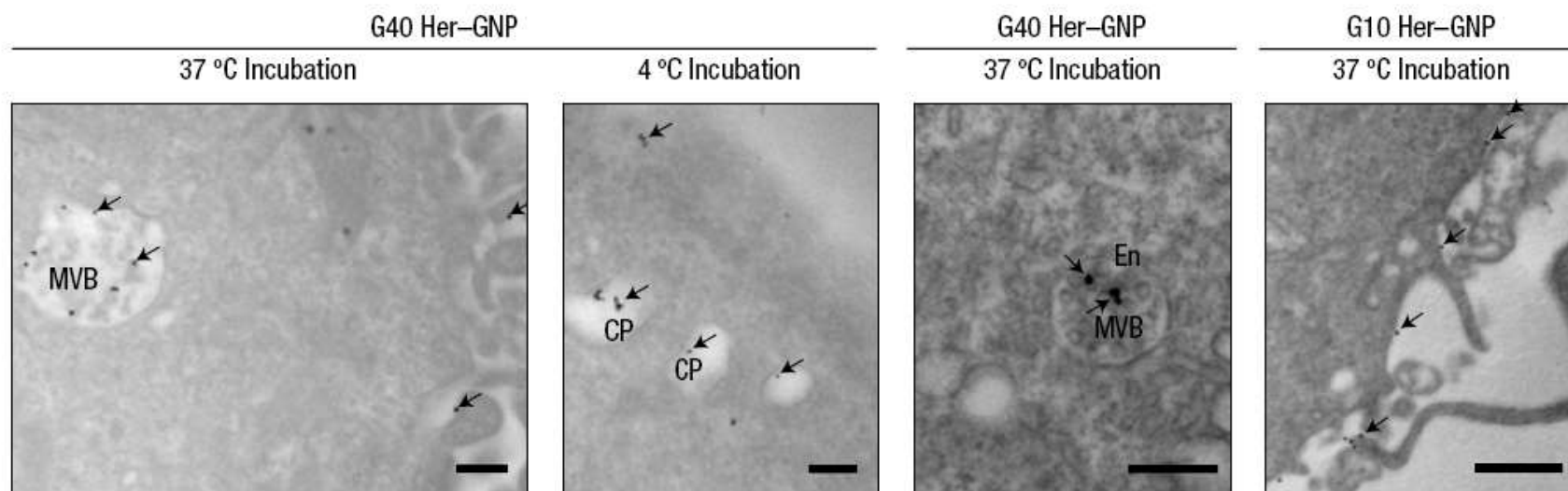
🟢 Spherical particle	• 10 nm nanoparticle	⬮ Endothelial cell
🟡 Non-spherical particle	• 50 nm nanoparticle	⬛ Cancer cell
🟡 200 nm nanoparticle		⬛ Apoptotic cancer cell

Figure 1 The geometry of a nanoparticle impacts its ability to perform its four basic functions. **a**, Navigation: non-spherical particles are more likely to be near the capillary walls and adhere to the cancer-specific molecules expressed on the vascular walls. **b**, Avoidance of biological barriers: particles of the right size fit through cancer-associated capillary wall fenestrations and localize preferentially in cancer lesions. **c**, Site- and cell-specific localization: nanoparticles of different sizes are taken up by cancer cells with different efficiency. **d**, Targeting of biological pathways. Chan and colleagues[3] showed that nanoparticles of different size can affect two signalling pathways, MAPK and AKT, to decrease proliferation and increase apoptotic cell death. These properties show that nanoparticles themselves can be candidate anticancer agents, even if they do not carry drugs.

Nanoparticle-mediated cellular response is size-dependent

a

	Herceptin	Herceptin + DAPI	SK-BR-3 zoom
HeLa			
SK-BR-3			

b

G40 Her–GNP — 37 °C Incubation — 4 °C Incubation

G40 Her–GNP — 37 °C Incubation
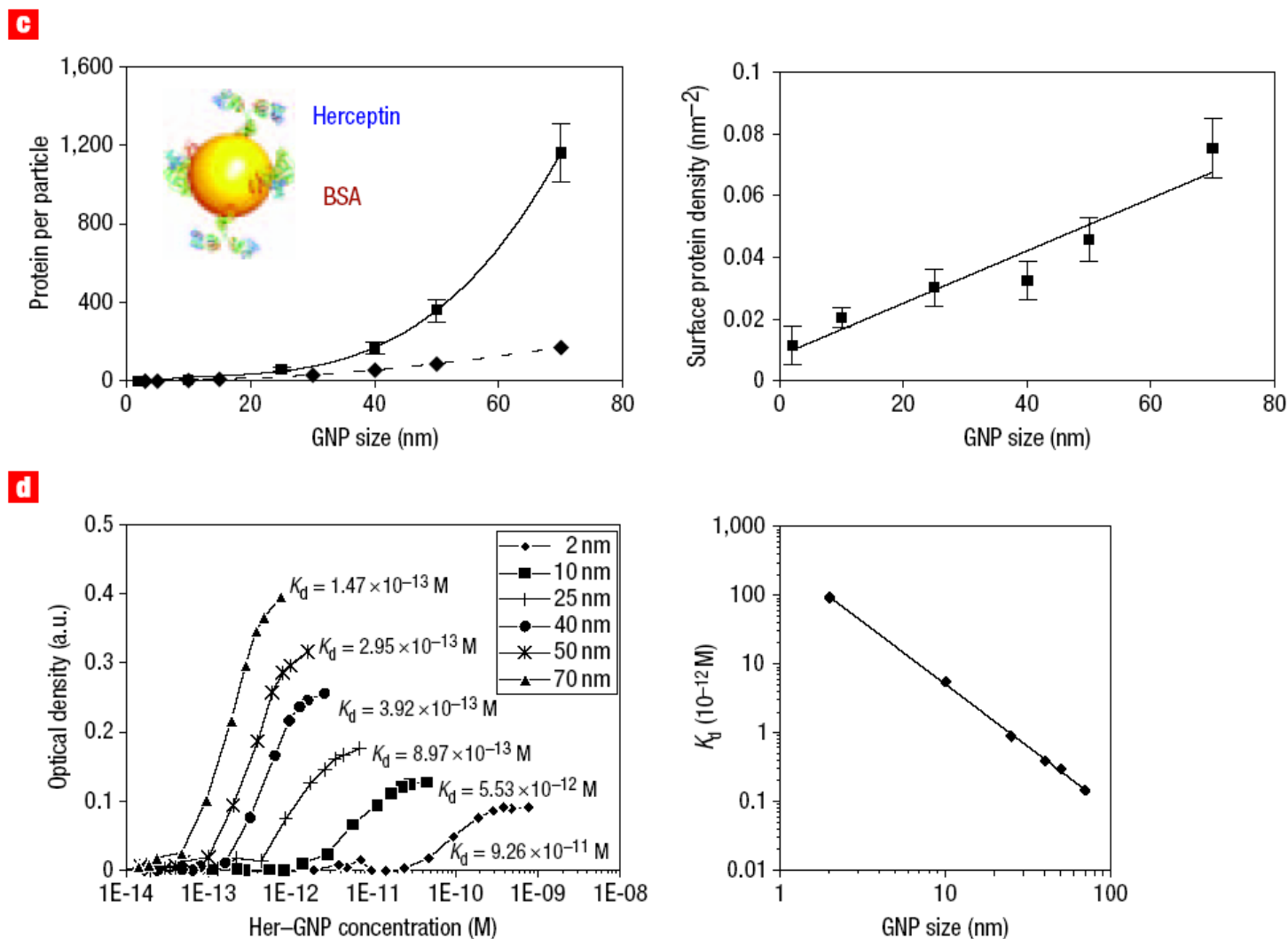
G10 Her–GNP — 37 °C Incubation

MVB

CP CP

En MVB

Figure 1 Specific interactions between Her−GNPs and ErbB2 receptors determine their internalization fate. **a**, Fluorescence images showing specific binding of Herceptin antibody (labelled with the Texas red dye molecule) to the ErbB2 receptors in SK-BR-3 cells. The cell nucleus is labelled with DAPI (blue). HeLa cells served as control. The enlarged view represents a single SK-BR-3 cell (scale bars = 5 μm). **b**, TEM images of cells incubated with G40 Her−GNPs at 37 °C and 4 °C and G40 and G10 Her−GNPs at 37 °C. Arrows indicate Her−GNPs (scale bars = 0.5 μm). MVB, multivesicular bodies; En, endosomes; CP, clathrin-coated pits. **c**, Antibody loading analysis. Left panel: Herceptin adsorption as a function of nanoparticle size (filled squares, experimental measurement; filled diamonds, calculation assuming constant Herceptin coverage area). Right panel: Surface-bound Herceptin density correlates with GNP size. Error bars, $\pm$s.d.; $n = 6$. **d**, Binding avidity analysis. Left panel: Effect of dissociation constant K_d for different-sized Her−GNPs. Right panel: K_d is inversely proportional to GNP size.
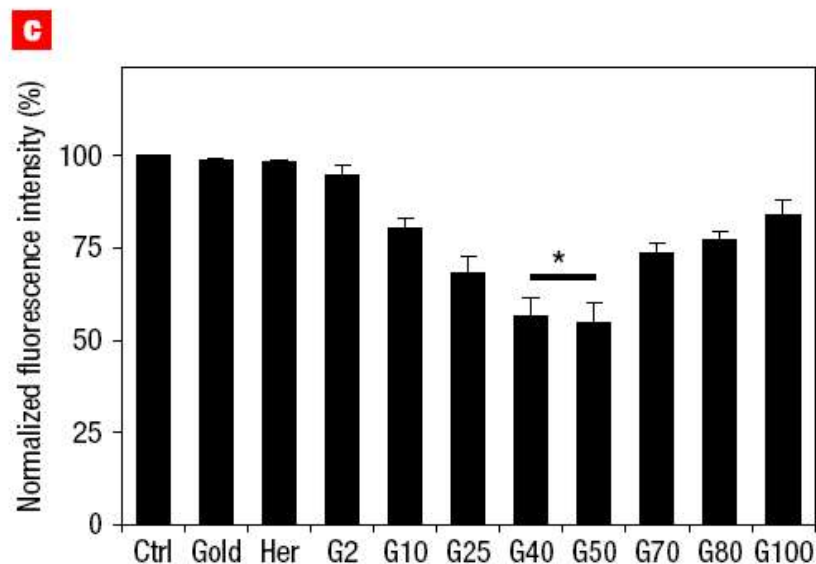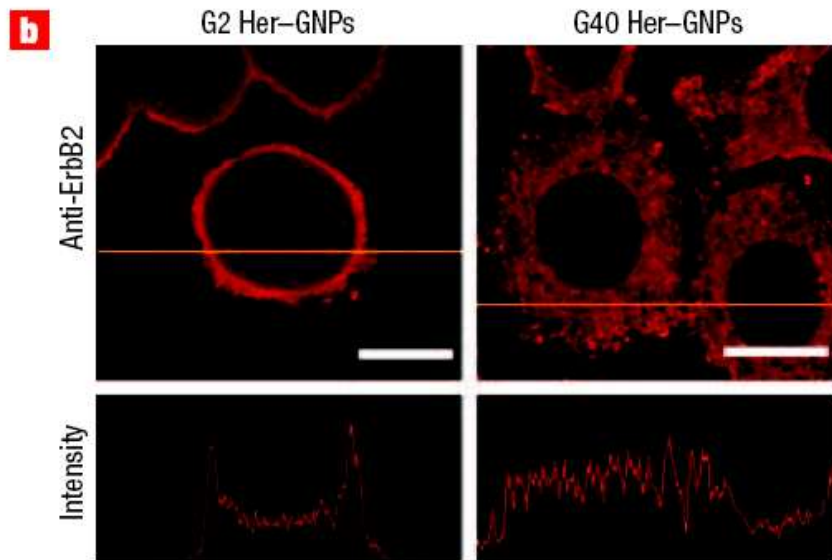
Figure 3 **Dependence of downregulation of membrane ErbB2 expression on nanoparticle size. a**, Illustrations with corresponding fluorescence images of ErbB2 receptor localization after treatment with different-sized Her–GNPs. Arrows indicate ErbB2 receptors, and the nucleus is counterstained with DAPI (blue) (scale bars=10 μm). **b**, Cross-sectional fluorescence intensity measurements of ErbB2 receptor localization patterns with G2 and G40 Her–GNPs (scale bars = 10 μm). **c**, Surface ErbB2 expression analysis using untreated cells normalized as 100% expression level (Ctrl). Cells were treated with unmodified 40-nm GNPs (Gold), Herceptin (Her) and Herceptin-modified GNPs of various sizes (* denotes statistical significance for G40/G50 compared to Her–GNPs of other sizes, $p < 0.05$, ANOVA). Error bars, ±s.d.; $n = 4$.
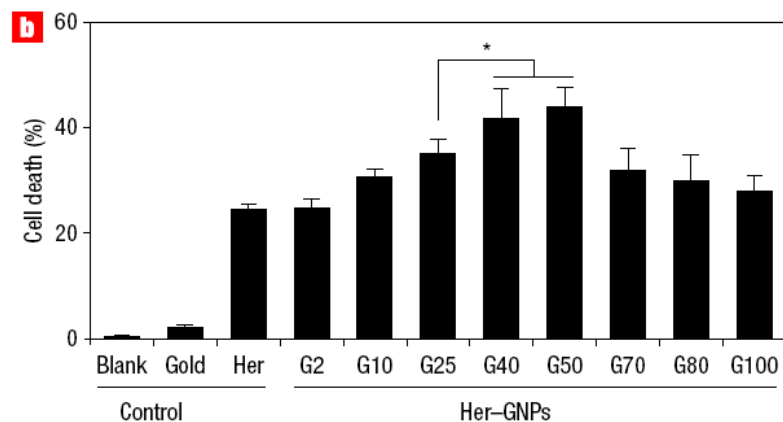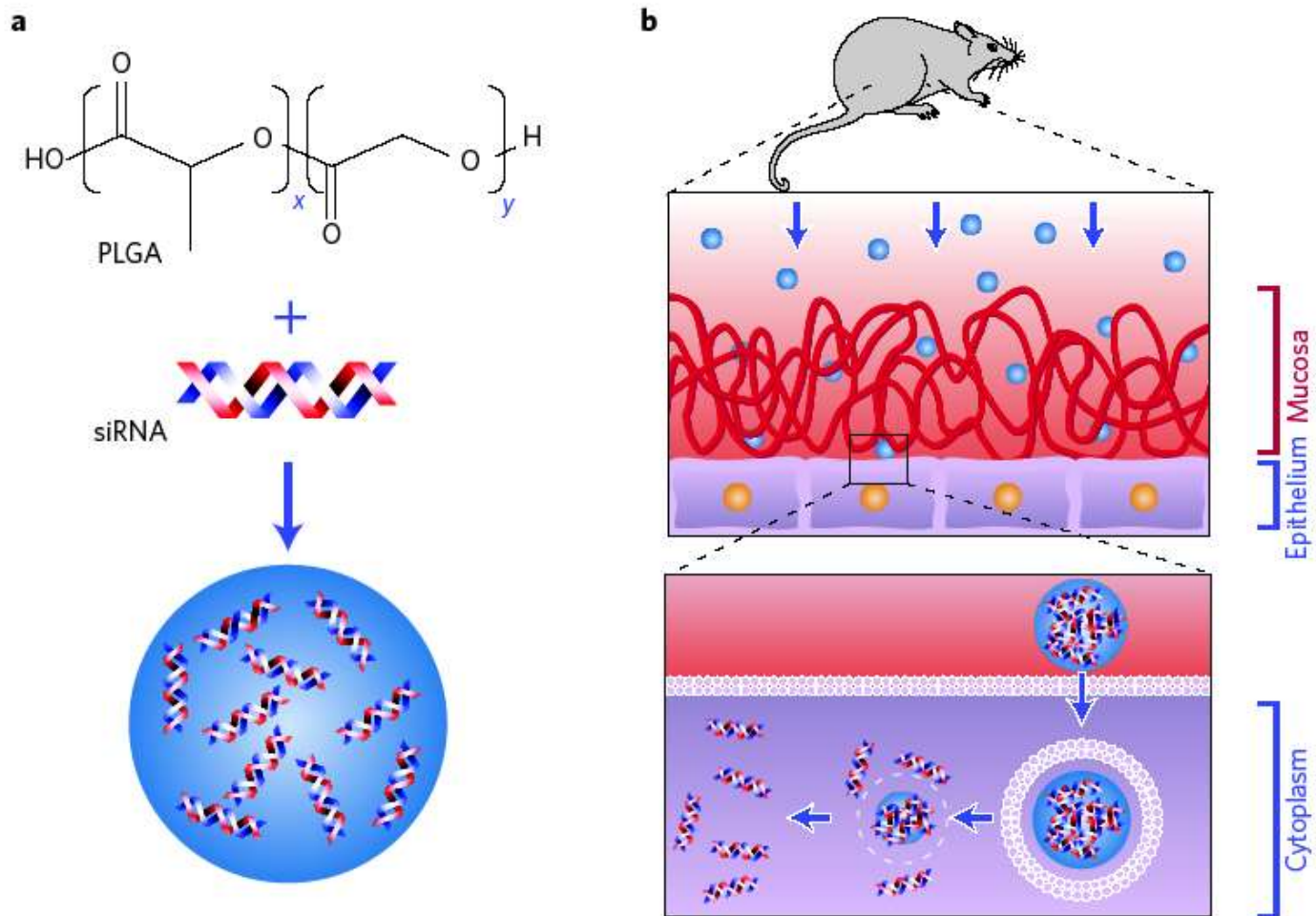
Figure 1 | Schematic illustration of the preparation and delivery of siRNA-loaded PLGA nanoparticles. **a**, Nanoparticles are formed using a double-emulsion solvent evaporation technique in which siRNA and a complexing agent (such as spermidine) are added to PLGA in an organic solvent. Particles are formed by sonication followed by solvent evaporation, and are then subsequently collected and freeze-dried. **b**, A single dose of siRNA-loaded nanoparticles is administered vaginally to mice. The particles must first diffuse through a mucosal layer; they are eventually taken up by epithelial cells and degrade, releasing their siRNA payloads.
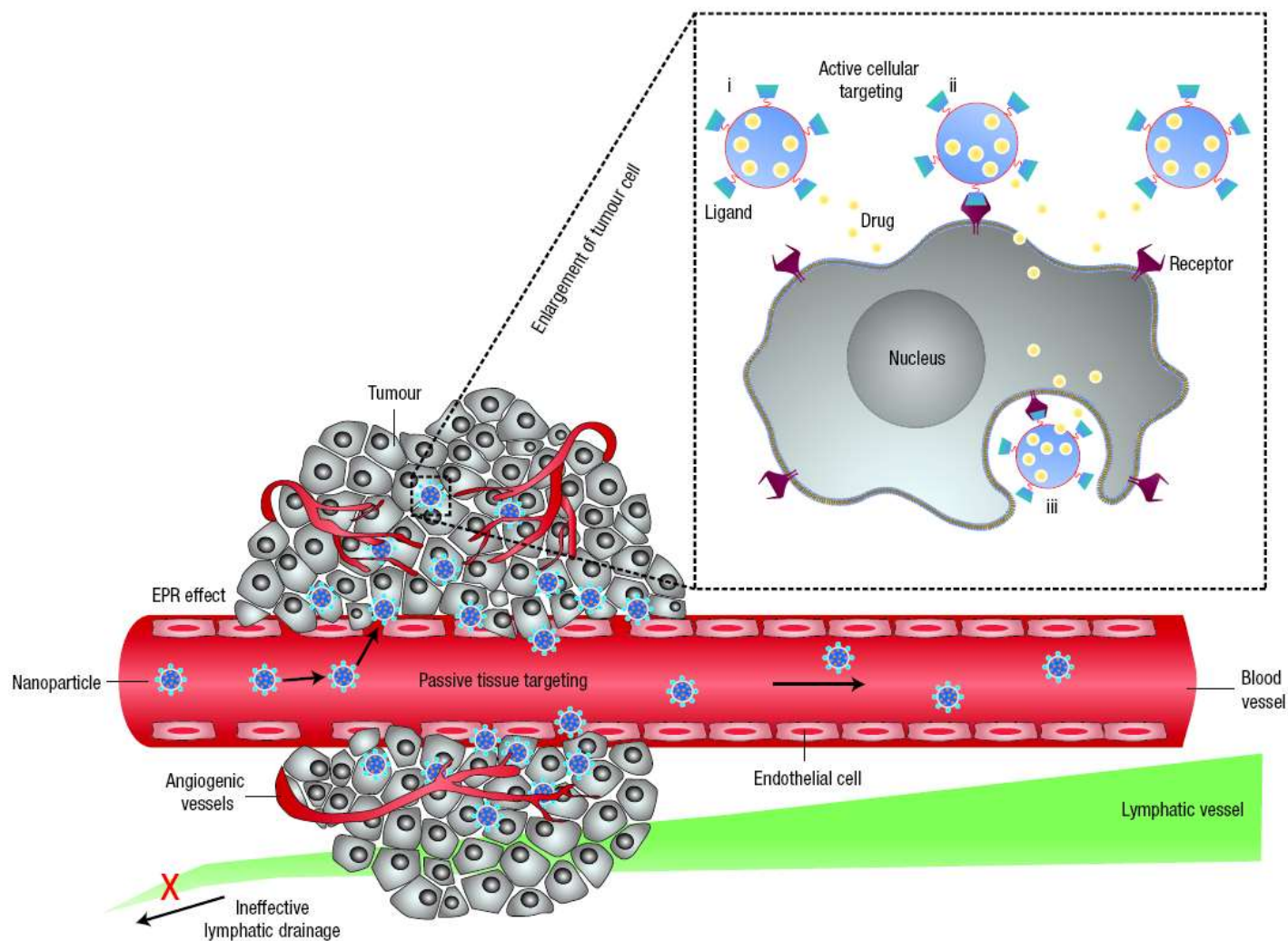
Figure 1 Schematic representation of different mechanisms by which nanocarriers can deliver drugs to tumours. Polymeric nanoparticles are shown as representative nanocarriers (circles). Passive tissue targeting is achieved by extravasation of nanoparticles through increased permeability of the tumour vasculature and ineffective lymphatic drainage (EPR effect). Active cellular targeting (inset) can be achieved by functionalizing the surface of nanoparticles with ligands that promote cell-specific recognition and binding. The nanoparticles can (i) release their contents in close proximity to the target cells; (ii) attach to the membrane of the cell and act as an extracellular sustained-release drug depot; or (iii) internalize into the cell.
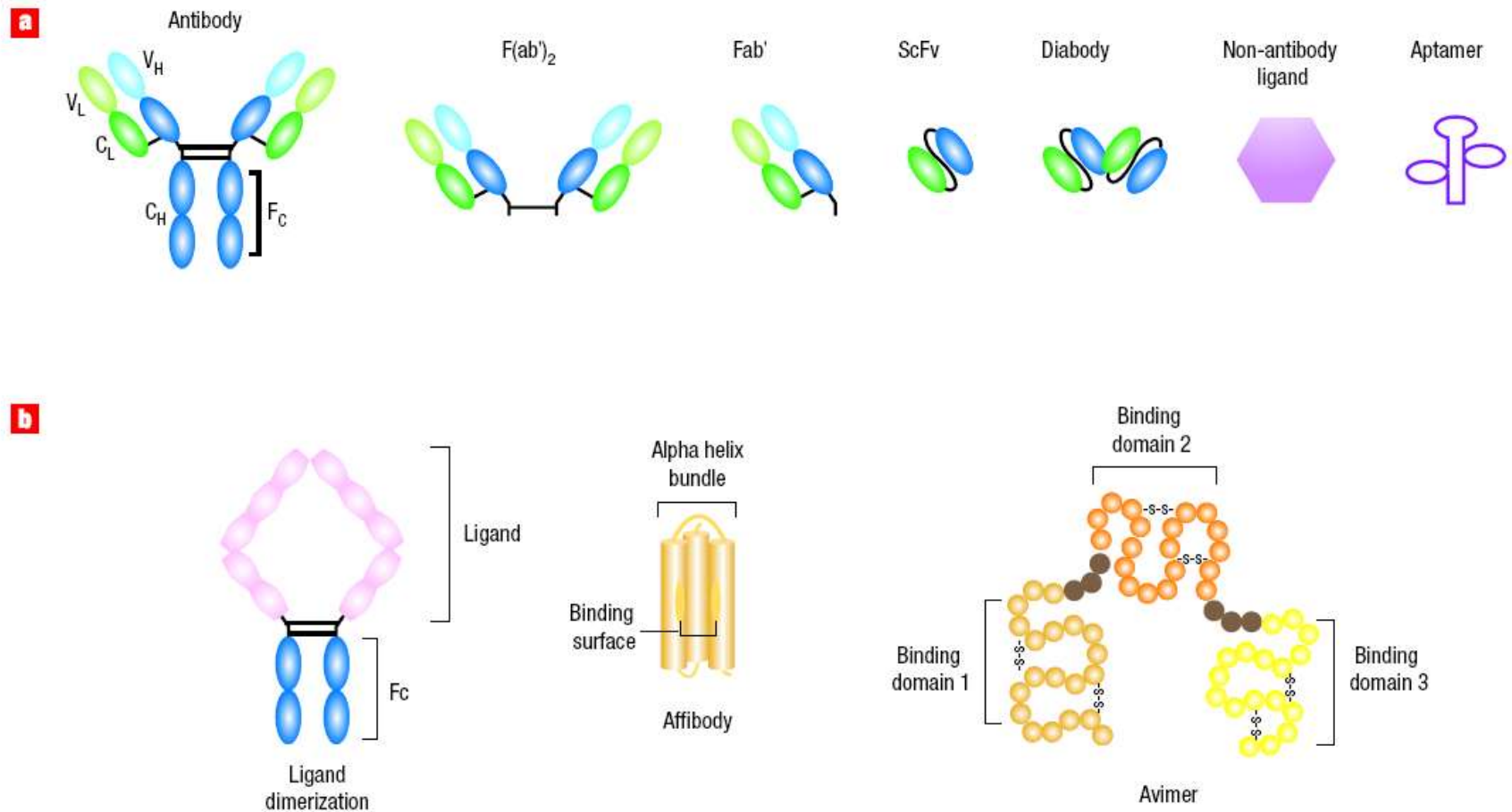
Figure 2 Common targeting agents and ways to improve their affinity and selectivity. **a**, The panel shows a variety of targeting molecules such as a monoclonal antibody or antibodies' fragments, non-antibody ligands, and aptamers. The antibody fragments F(ab)$_2$ and Fab are generated by enzymatic cleavage whereas the Fab , scFv, and bivalent scFv (diabody) fragments are created by molecular biology techniques. V_H: variable heavy chain; V_L: variable light chain; C_H: constant heavy chain; C_L: constant light chain. Non-antibody ligands include vitamins, carbohydrates, peptides, and other proteins. Aptamers can be composed of either DNA or RNA. **b**, Affinity and selectivity can be increased through ligand dimerization or by screening for conformational-sensitive targeting agents such as affibodies, avimers and nanobodies, as well as intact antibodies and their fragments.
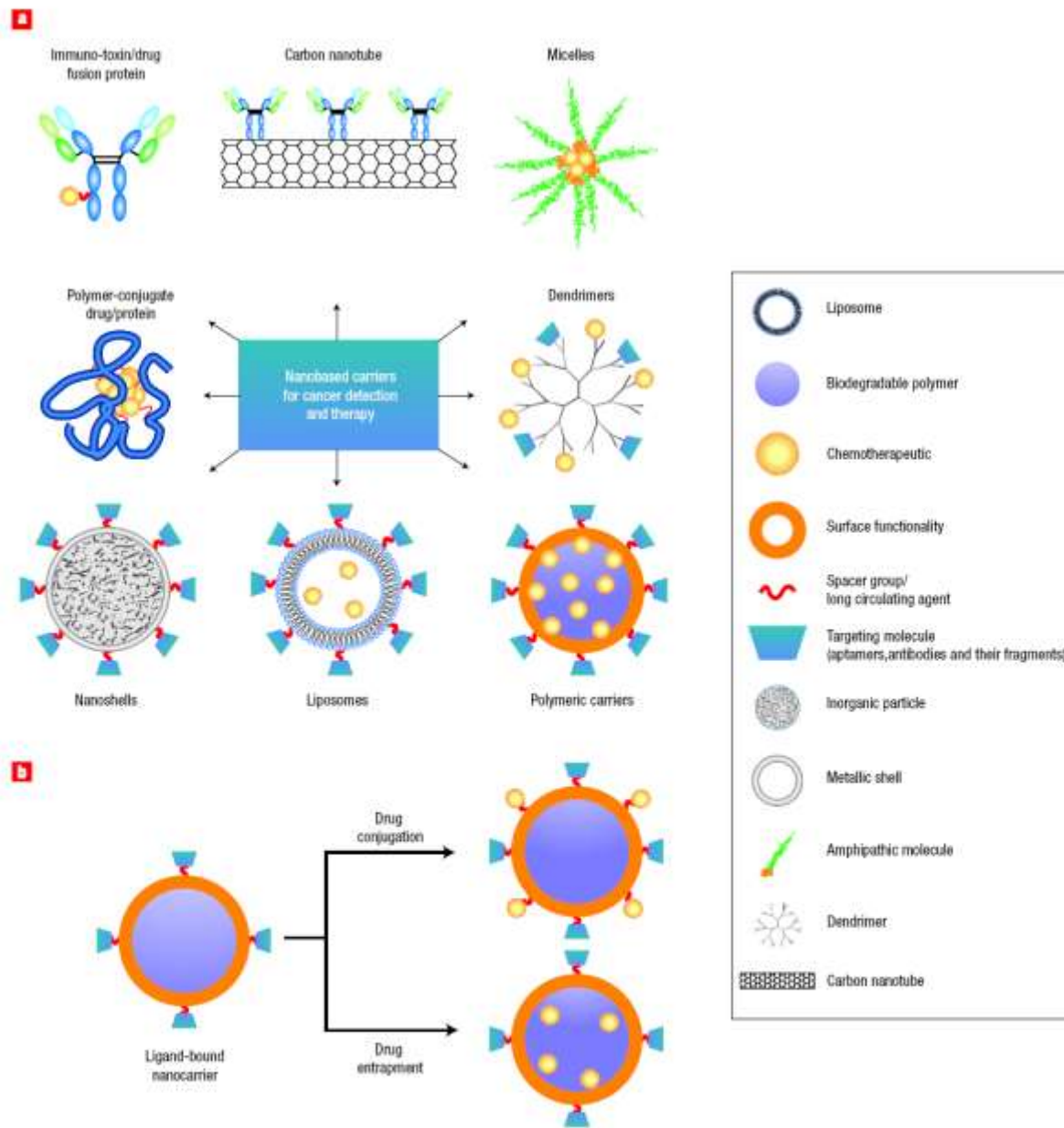
a

Immuno-toxin/drug fusion protein

Carbon nanotube

Micelles

Polymer-conjugate drug/protein

Nanobased carriers for cancer detection and therapy

Dendrimers

Nanoshells

Liposomes

Polymeric carriers

b

Ligand-bound nanocarrier

Drug conjugation

Drug entrapment

Liposome

Biodegradable polymer

Chemotherapeutic

Surface functionality

Spacer group/ long circulating agent

Targeting molecule (aptamers, antibodies and their fragments)

Inorganic particle

Metallic shell

Amphipathic molecule

Dendrimer

Carbon nanotube

Figure 3 Examples of nanocarriers for targeting cancer. **a**, A whole range of delivery agents are possible but the main components typically include a nanocarrier, a targeting moiety conjugated to the nanocarrier, and a cargo (such as the desired chemotherapeutic drugs). **b**, Schematic diagram of the drug conjugation and entrapment processes. The chemotherapeutics could be bound to the nanocarrier, as in the use of polymer–drug conjugates, dendrimers and some particulate carriers, or they could be entrapped inside the nanocarrier.

Table 5

Confirmed and likely nanomedicine applications and products identified that utilize active targeting

Application(s)/Product(s)	Company	Status	Condition	Nanocomponent	Targeting Mechanism
Ontak [45,46]	Seragen, Inc.	Approved (1999)	T-Cell Lymphoma	Protein NP	IL-2 Protein
MBP-Y003, MBP-Y004, MBP-Y005 [47]	Mebiopharm Co., Ltd	Preclinical	Lymphoma	Liposome	Transferrin
MBP-426 [47–49]	Mebiopharm Co., Ltd	Phase I/II	Solid Tumors	Liposome	Transferrin
CALAA-01 [19,50]	Calando Pharmaceuticals	Phase I	Solid Tumors	NP	Transferrin
SGT-53 [19,51]	SynerGene Therapeutics, Inc.	Phase I	Solid Tumors	Liposome	Transferrin
MCC-465 [48,52]	Mitsubishi Tanabe Pharma Corp	Phase I	Stomach Cancer	Liposome	GAH Antibody
Actinium-225-HuM195 [53]	National Cancer Institute	Phase I	Leukemia	NP	HuM195 Antibody
AS15 [54]	GlaxoSmithKline Biologicals	Phase I/II	Metastatic Breast Cancer	Liposome	dHER2 Antibody
PK2 [48,55]	Pharmacia & Upjohn Inc.	Phase I	Liver Cancer	Polymeric NP	Galactose
Rexin-G, Reximmune-C [56,57]	Epeius Biotechnologies	Phase I/II	Solid Tumors	NP	von Willebrand factor (Collagen-Binding)
Aurimune (CYT-6091) [19,58] Auritol (CYT-21001) [59]	CytImmune Sciences, Inc.	Phase II Preclinical	Solid Tumors	Colloid Gold	TNF-α
SapC-DOPS [60,61]	Bexion Pharmaceuticals, Inc.	Preclinical	Solid Tumors	Liposome	Saposin C
Targeted Emulsions [62,63]	Kereos, Inc.	Preclinical	In Vivo Imaging	Emulsion	"Ligands"
Opaxio [42,64]	Cell Therapeutics, Inc.	Phase III	Solid Tumors	Polymeric NP	Enzyme-Activated
ThermoDox [43]	Celsion Corporation	Phase II/III	Solid Tumors	Liposome	Thermosensitive
DM-CHOC-PEN [44,65]	DEKK-TEC, Inc.	Phase I	Brain Neoplasms	Emulsion	PenetrateBlood-Brain-Barrier

Table 7
Confirmed and likely nanomedicine products that exhibit active behavior, beyond active targeting, identified
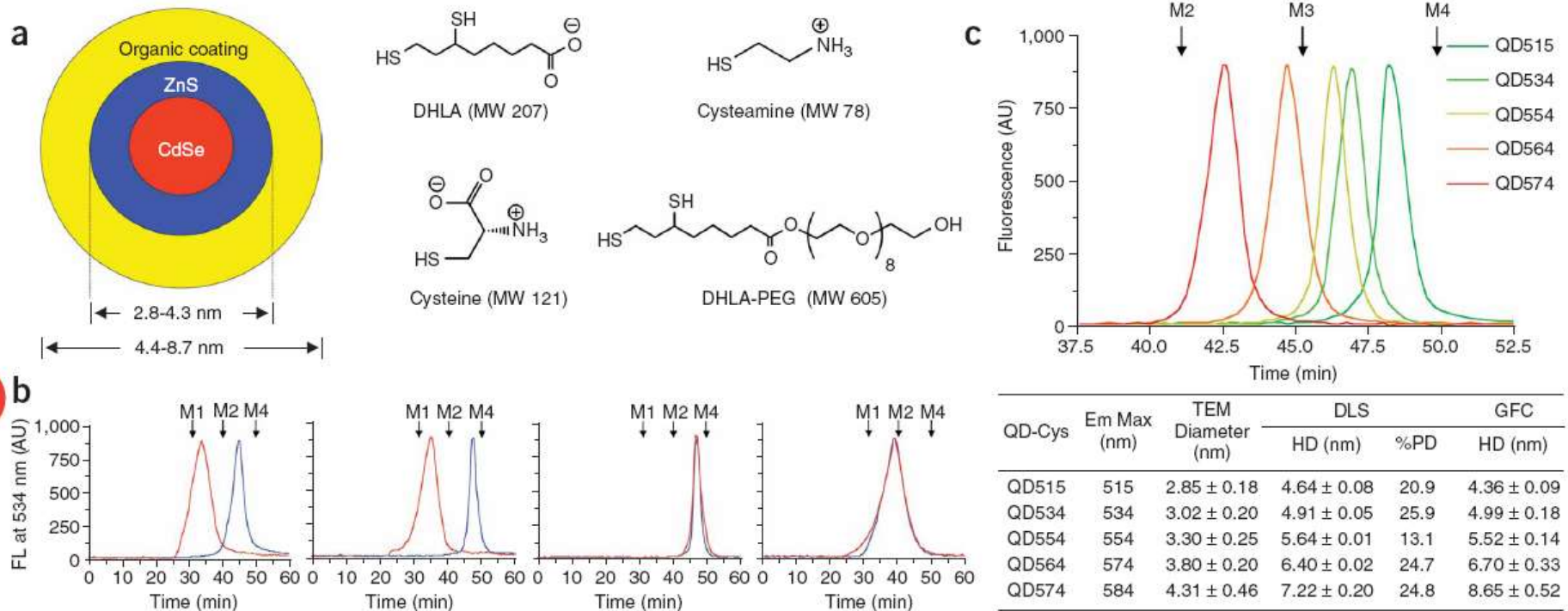
Use	Application(s)/Product(s)	Company	Status	Nanocomponent	Active Mechanism
Solid Tumor Hyperthermia	NanoTherm [77]	MagForce Nanotechnologies AG	Approved	Iron Oxide NPs	AC Magnetic Heating
	Targeted Nano-Therapeutics [105]	Aspen Medisys, LLC. (Formerly Triton BioSystems, Inc.)	Pre-Clinical	Iron Oxide NPs	AC Magnetic Heating
	AuroShell [83]	Nanospectra Biosciences	Phase I	Gold Nanoshell	IR Laser Heating
Solid Tumor Treatment	NanoXray [77]	Nanobiotix	Phase I	Proprietary NP	X-Ray-Induced Electron Emission
In Vivo Imaging	Feridex IV, GastromarkCombidex (Ferumoxtran-10) [79,106]	Advanced Magnetics	Approved (1996)Phase III	Iron Oxide NPs	Enhanced MRI Contrast
	Endorem, Lumirem, Sinerem [79,106]	Guebert	Approved / Investigational	Iron Oxide NPs	Enhanced MRI Contrast
	FeraSpin [107]	Miltenyi Biotec	Research Use Only	Iron Oxide NPs	Enhanced MRI Contrast
	Clariscan [79]	Nycomed	Phase III	Iron Oxide NPs	Enhanced MRI Contrast
	Resovist [79,106] Supravist [80]	Schering	Approved (2001)Phase III	Iron Oxide NPs	Enhanced MRI Contrast
In Vitro Imaging	Qdot Nanocrystals [108]	Invitrogen Corporation	Research Use Only	Quantum Dot	Fluorescent Emission
	Nanodots [109]	Nanoco Group PLC	Research Use Only	Quantum Dot	Fluorescent Emission
	TriLite™ Nanocrystals [110]	Crystalplex Corporation	Research Use Only	Quantum Dot	Fluorescent Emission
	eFluor Nanocrystals [111]	eBiosciences	Research Use Only	Quantum Dot	Fluorescent Emission
	NanoHC [112]	DiagNano	Investigational (Research Only)	Quantum Dot	Fluorescent Emission
In Vitro Cell Separation	CellSearch® EpithelialCell Kit [99]	Veridex, LLC (Johnson & Johnson)	Approved (2004)	Iron Oxide NPs	Magnetic Separation
	NanoDX [113]	T2 Biosystems	Research Use Only	Iron Oxide NPs	Magnetic Separation

Table 6
Confirmed and likely nanomedicine products that have been approved by the FDA through the 510(k) process identified

Use	Application(s)/Product(s)	Company	Approval Year	Nanocomponent Description
Bone Substitute	Vitoss [14]	Orthovita	2003	100-nm Calcium-Phosphate Nanocrystals
	Ostim [87]	Osartis	2004	20-nm Hydroxapatite Nanocrystals
	OsSatura [62]	Isotis Orthobiologicals US	2003	Hydroxapatite Nanocrystals
	NanOss [77]	Angstrom Medica, Inc.	2005	Hydroxapatite Nanocrystals
	Alpha-bsm, Beta-bsm, Gamma-bsm, EquivaBone, CarriGen [93]	ETEX Corporation	2009	Hydroxapatite Nanocrystals
Dental Composite	Ceram X Duo [94]	Dentspley	2005	Ceramic NPs
	Filtek [95]	3M Company	2008	Silica and Zirconium NPs
	Premise [14]	Sybron Dental Specialties	2003	"Nanoparticles"
	Nano-Bond [96]	Pentron® Clinical Technologies, LLC	2007	"Nanoparticles"
Device Coating	ON-Q SilverSoaker / SilvaGard™ [97]	I-Flow Corporation / AcryMed, Inc.	2005	Antimicrobial Nanosilver
	EnSeal Laparoscopic Vessel Fusion [39]	Ethicon Endo-Surgery, Inc.	2005	NP-Coated Electrode
	NanoTite Implant [98]	Biomet	2008	Calcium Phosphate Nanocrystal Coating
In Vitro Assay	CellTracks® [14]	Immunicon Corporation	2003	Magnetic NPs
	NicAlert [14]	Nymox	2002	Colloidal Gold
	Stratus CS [62]	Dade Behring	2003	Dendrimers
	CellSearch® Epithelial Cell Kit [99]	Veridex, LLC (Johnson & Johnson)	2004	Iron Oxide NPs
	Verigene [100,101]	Nanosphere, Inc.	2007	Colloidal Gold
	MyCare™ Assays [102]	Saladax Biomedical	2008	"Nanoparticles"
Medical Dressing	Acticoat® [97,103]	Smith & Nephew, Inc.	2005	Antimicrobial Nanosilver
Dialysis Filter	Fresenius Polysulfone® Helixone® [104]	NephroCare	1998	Nanoporous Membrane
Tissue Scaffold	TiMESH [39]	GfE Medizintechnik GmbH	2004	30-nm Titanium Coating

Renal clearance of quantum dots

a

T = 0 h

Ki
Bl
Ki

Ki
Bl
Ki

T = 2 h

Ki
Bl
Ki

Ki
Bl
Ur
Ki

b

| QD515 (4.36 nm) | QD534 (4.99 nm) | QD554 (5.52 nm) | QD564 (6.70 nm) | QD574 (8.65 nm) |

c QD515 (4.36 nm)

Color video | Gamma | Merge

Intact

Bl

Resected

Sk   Ad   Mu   Bo
He   Lu   Sp   Li
Ki   St   In   Br

Li

Ki

%ID / QD515

Heart Lung Spleen Liver Kidneys Stomach Intestine Brain Feces

cpm
200
180
160
140
120
100
80
60
40
20
0

d QD574 (8.65 nm)

Color video | Gamma | Merge

Intact

Li / Sp / Lu

Bl

Resected

Sk   Ad   Mu   Bo
He   Lu   Sp   Li
Ki   St   In   Br

Lu   Sp   Li

Ki

%ID / QD574

Heart Lung Spleen Liver Kidneys Stomach Intestine Brain Feces

cpm
200
180
160
140
120
100
80
60
40
20
0

Figure 1. Cross-linked iron oxide (CLIO) nanoparticles for T_2-weighted images of rodent pancreatic cancer: (a) preinjection of CLIO, (b) postinjection of CLIO, and (c) higher magnification of postinjection image with the arrow indicating tumor. L, liver; P, pancreas; K, kidney; B, bowel.[16]
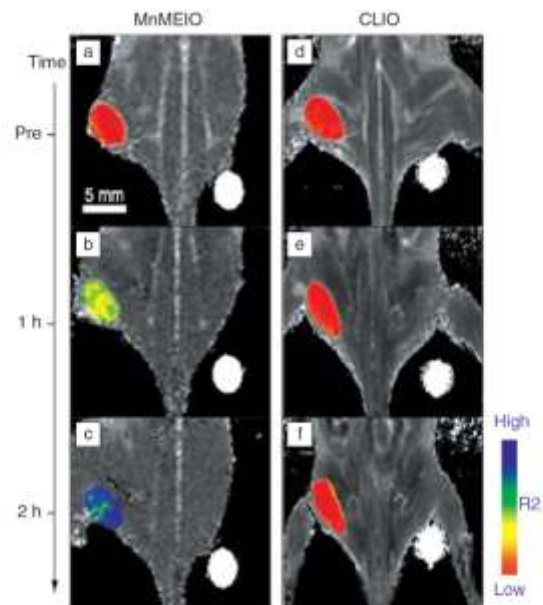
Figure 2. In vivo magnetic resonance detection of cancer after administration of magnetic nanoparticles Herceptin conjugates. MnFe$_2$O$_4$ nanoparticles (MnMEIO) (a–c) show higher signal enhancement than cross-linked iron oxide (CLIO) (d–f).[24] R2, inverse of transverse relaxation time.

Mesoporous Silica

MRI

Cell labeling

Activatable
probes

Magnetic
NPs

Multimodal
imaging

Drug delivery

Gene delivery

DNA and other nucleic acids

Sensitive coverage

Targeting agents

Proteins

Magnetic
nanoparticles

Polyethylene glycol

Adsorbed drug

Fluorescent
molecules

Anchored prodrug

MRI active
agent

Nanocaps
(stimuli-responsive)

External funcionalization

R

Functional groups to tune
the surface charge

Mesoporous silica NP

Cargo

SiO_2

Mass transport inhibition

SiO_2

Controlled release

pH
Temperature
Light
Ultrasounds
Hc
Redox potential

Carbon Nanotubes

SWNT   MWNT   open MWNT

5 nm

Figure 2. TEM images showing a) the plasma deposited acrylic acid (AA) polymer thin film on the carbon nanotube, the lattice image of carbon nanotube can be clearly seen with an extremely thin layer of polymer film (~ 2 nm); b) the thin film of AA was plasma deposited near the open end of the carbon nanotube.
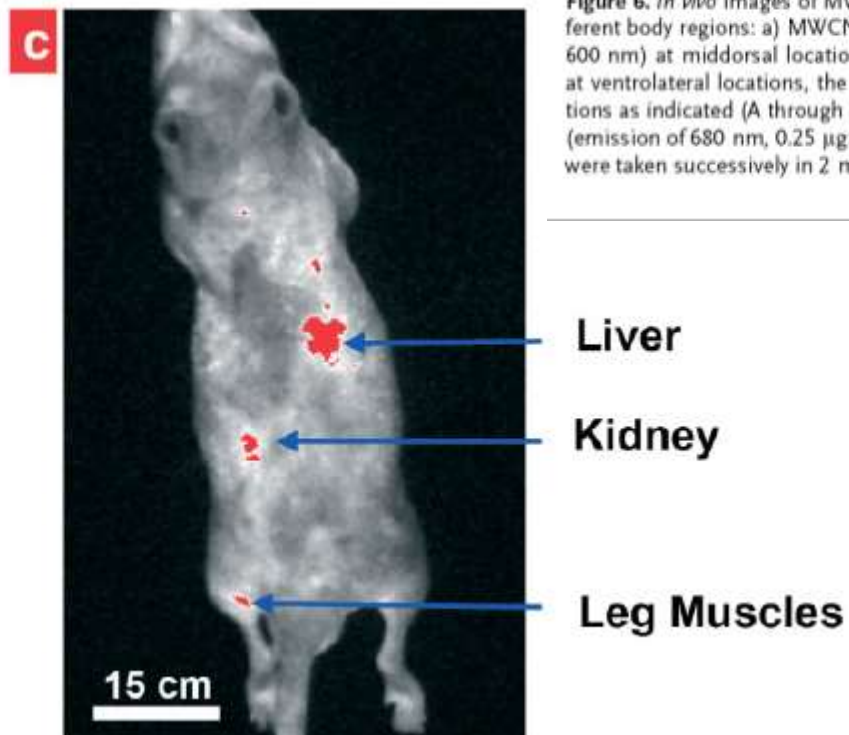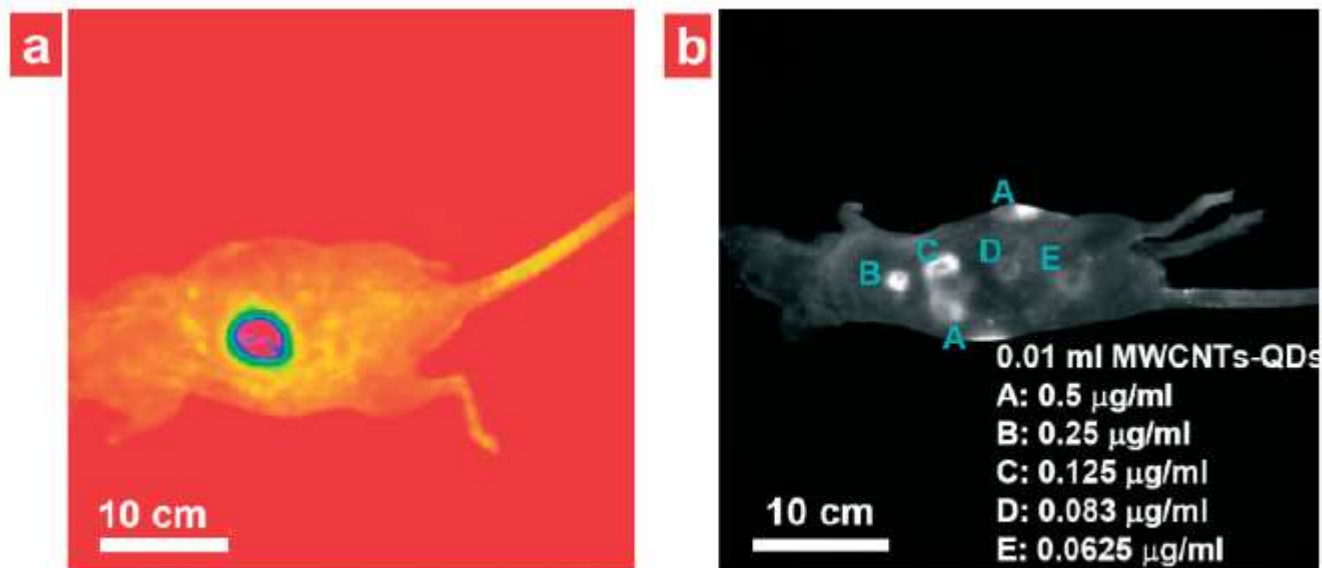
Figure 6. *In vivo* images of MWCNTs-QDs (0.5 μg ml⁻¹ in PBS) in mice injected at different body regions: a) MWCNTs attached with CdSe/ZnS quantum dots (emission of 600 nm) at middorsal location; b) MWCNTs attached with CdSe/ZnS quantum dots at ventrolateral locations, the suspensions were diluted by PBS at various concentrations as indicated (A through E); c) MWCNTs attached with InGaP/ZnS quantum dots (emission of 680 nm, 0.25 μg ml⁻¹ in PBS) in liver, kidney, and leg muscles. All images were taken successively in 2 min under epi-UV illuminator with excitation of 435 nm.

Polymer
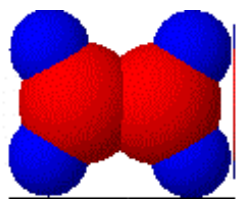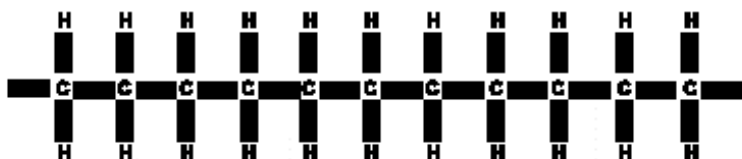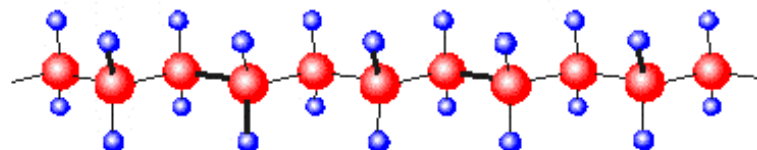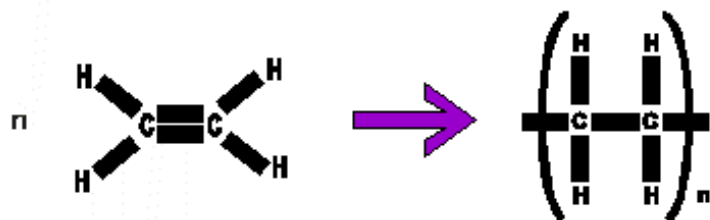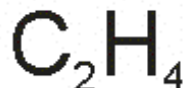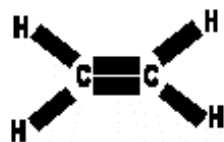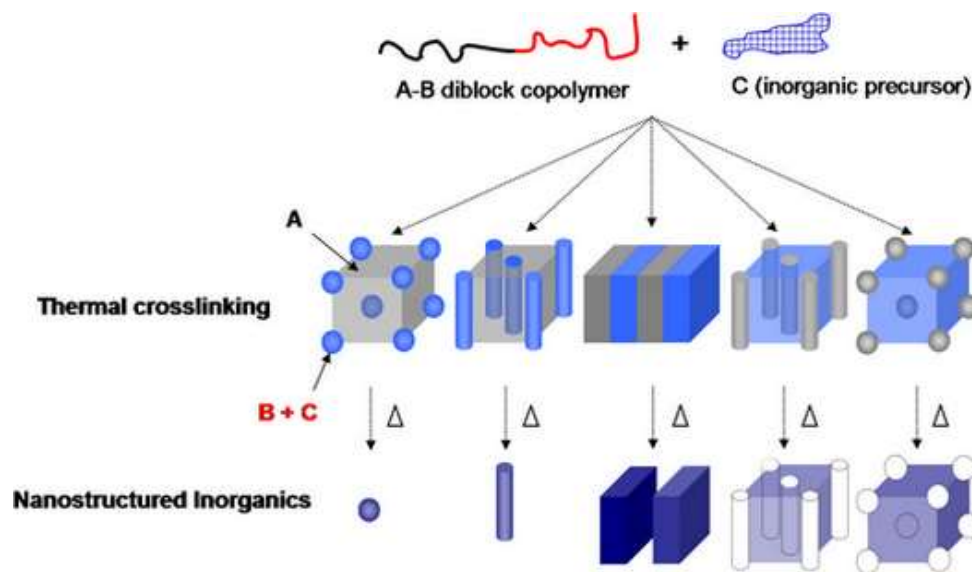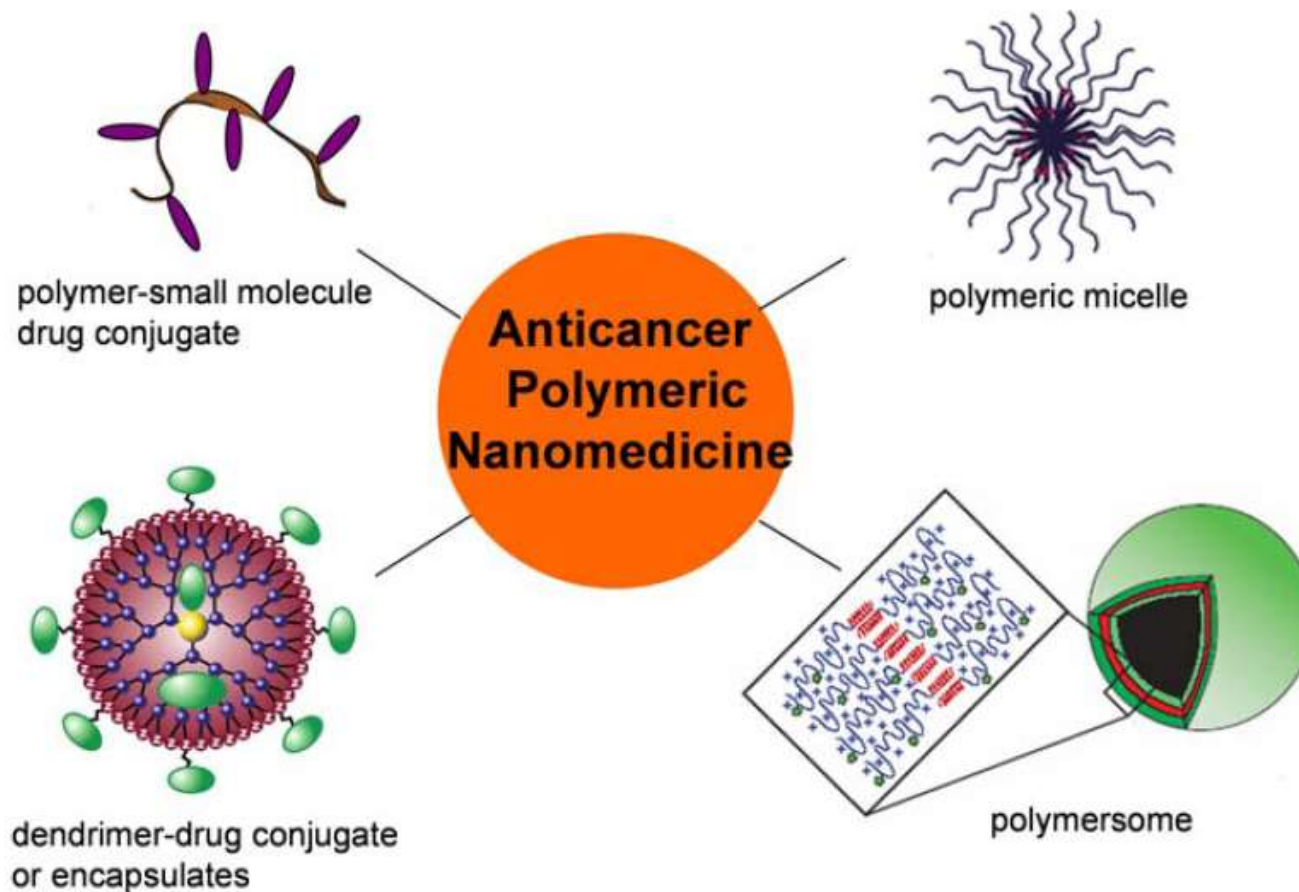
Figure 1. Illustration of various anticancer polymeric nanomedicines that have been developed and are used in cancer drug delivery. Polymer-small molecule drug conjugates are usually hydrophilic (water-soluble) polymers with covalently bound, releasable hydrophobic drug molecules. Polymeric micelles are core-shell micellar nanostructures with a hydrophobic core that can be used for the encapsulation of hydrophobic drug molecules and for the controlled release of hydrophobic therapeutics, and a hydrophilic shell can be used for micelle surface modification (e.g., incorporation of targeting ligands). Polymersomes are a class of hollow spherical nanostructures that enclose a solution and can be used to deliver hydrophilic therapeutics such as DNA and proteins. Dendrimer drug conjugate or encapsulates are a class of drug delivery systems with drugs conjugated to the periphery or encapsulated inside of monodisperse macromolecules with highly branched, symmetric, three-dimensional architectures.

a

Polyethylene glycol-*b*-poly(glutamic acid)
[PEG-*b*-P(Glu)]

+

or

cis-diamminedichloroplatinum(II)   (1,2-diaminocyclohexane)platinum(II)
Cisplatin, CDDP   DACHPt aqueous complex

b

Metal-polymer
complex formation

Self-assembly in aqueous environment

c

Platinum drug-loaded micelles
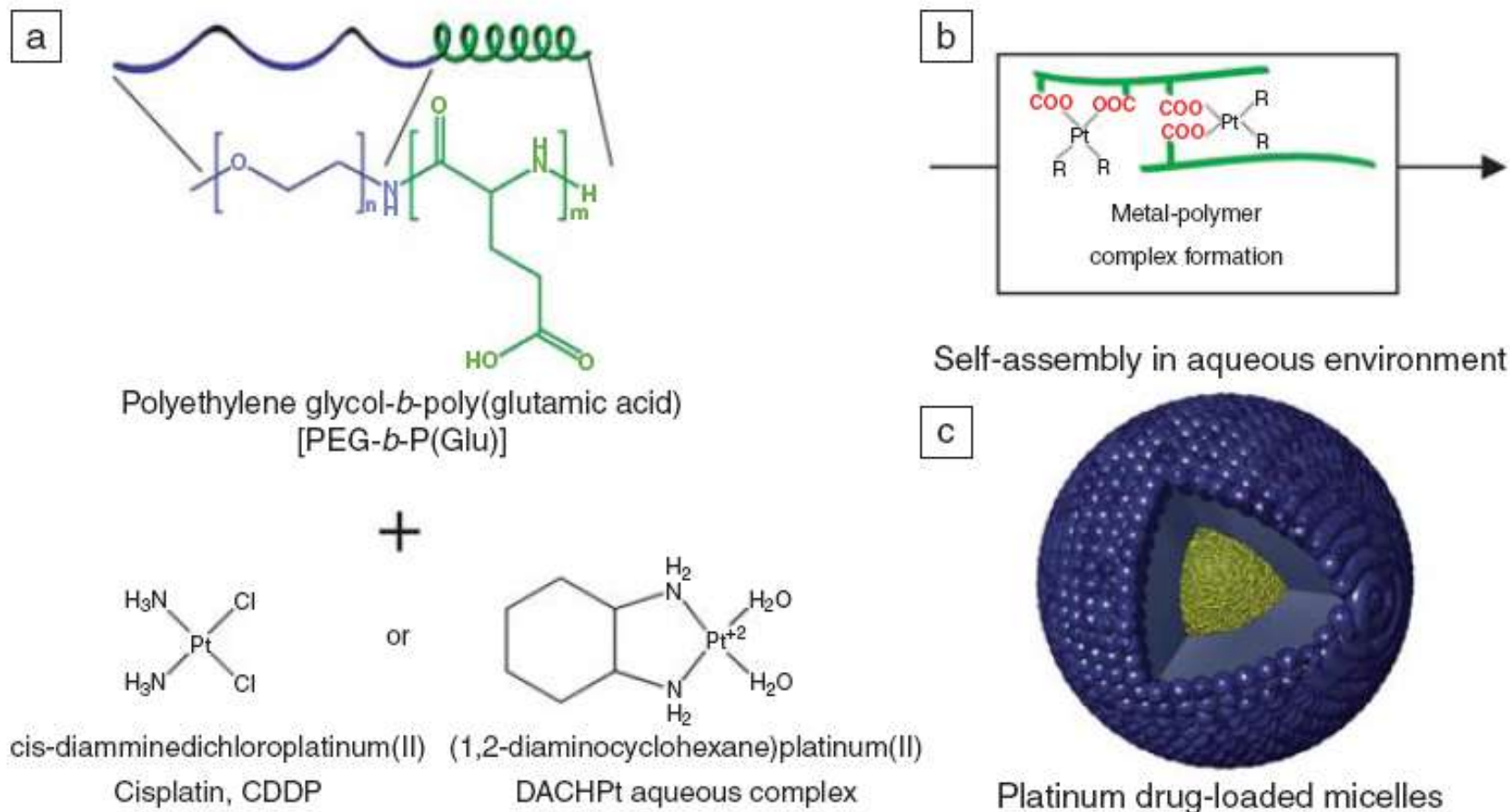
Figure 2. (a) Schematic diagram of proposed self-assembly of platinum drug-loaded polymeric micelles.[101,102] (b) The self-assembly is mediated by the coordination of the platinum (II) and the carboxylate groups (COO) of the poly(glutamic acid) segments. (c) Narrowly distributed polymeric micelles with dense drug-loaded cores are formed.
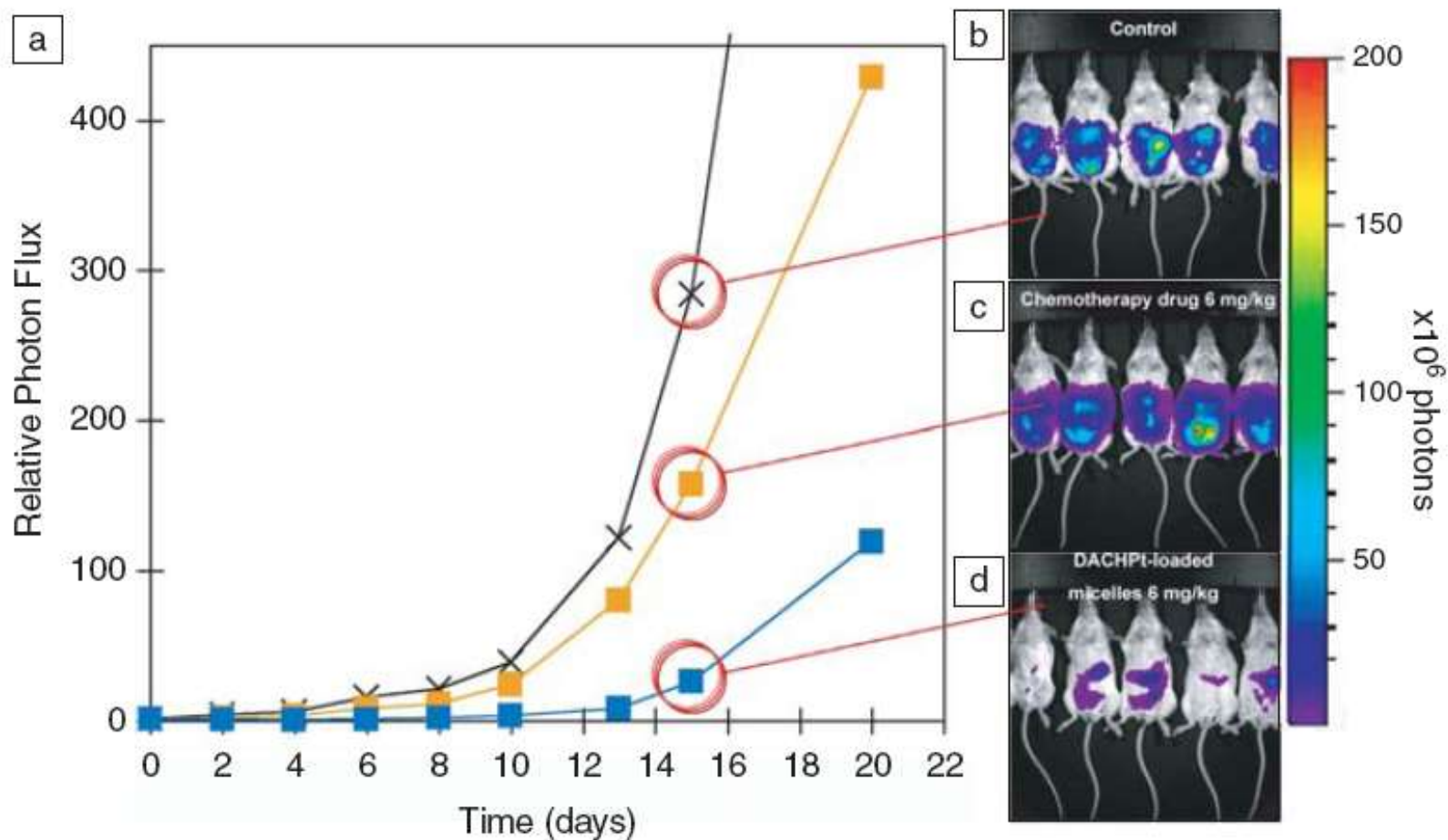
Figure 3. Platinum drug-loaded polymeric micelles.[103] (a) Antitumor activity measured as the relative photon flux, which is the ratio between the photon flux (photons/second) and the initial photon flux, from bioluminescent intraperitoneal (within the abdominal cavity) metastasis and the in vivo bioluminescent images corresponding to day 10. (b) Control (crosses), (c) the clinically used DACHPt derivative, oxaliplatin, 6 mg/kg (orange squares), (d) (1,2-diaminocycloheance) platinum (II) (DACHPt)-loaded micelle (blue squares).

Dendrimer

Liposome

Liposome

PEG

RGD Peptide

Liposome Bilayer
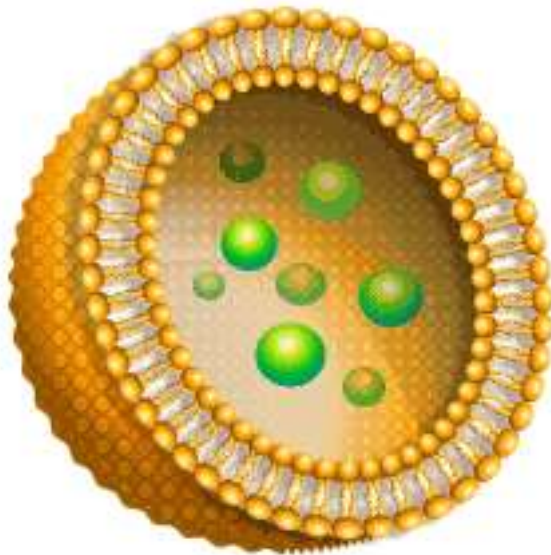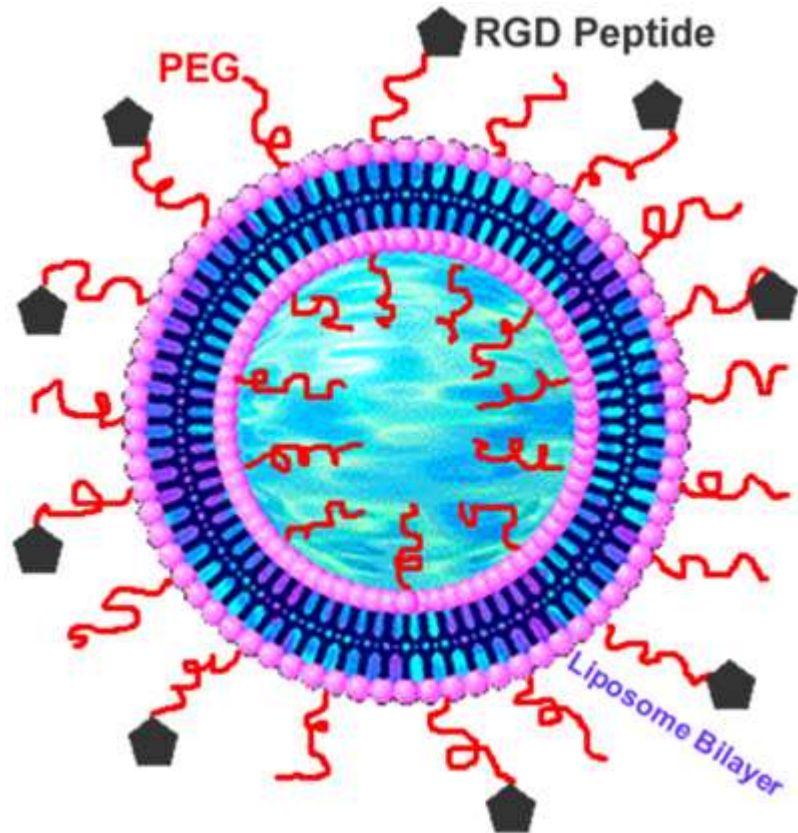
Cationic Lipids

Immune Cells

APC

b

Antibody immunotherapy
Blocking inhibitory GBR

c

Antibody immunotherapy
Glycan targeting with genetically modified mAb

ADCC-mediated killing

Antibody–glycosidase conjugate

d

Cellular immunotherapy
Glycan targeting with CAR T cells

a

Anti-glycan vaccines

mAb αGBR

Anti-glycan mAb

Anti-glycan immunotoxin

CAR T cell

e

DC targeting
Using glycans for DC loading

Glycan-specific antibodies

TCR

Glycopeptide-specific CD8+ and CD4+ T cells

Cancer cell

Glycopeptide

Immune Checkpoint Blockade
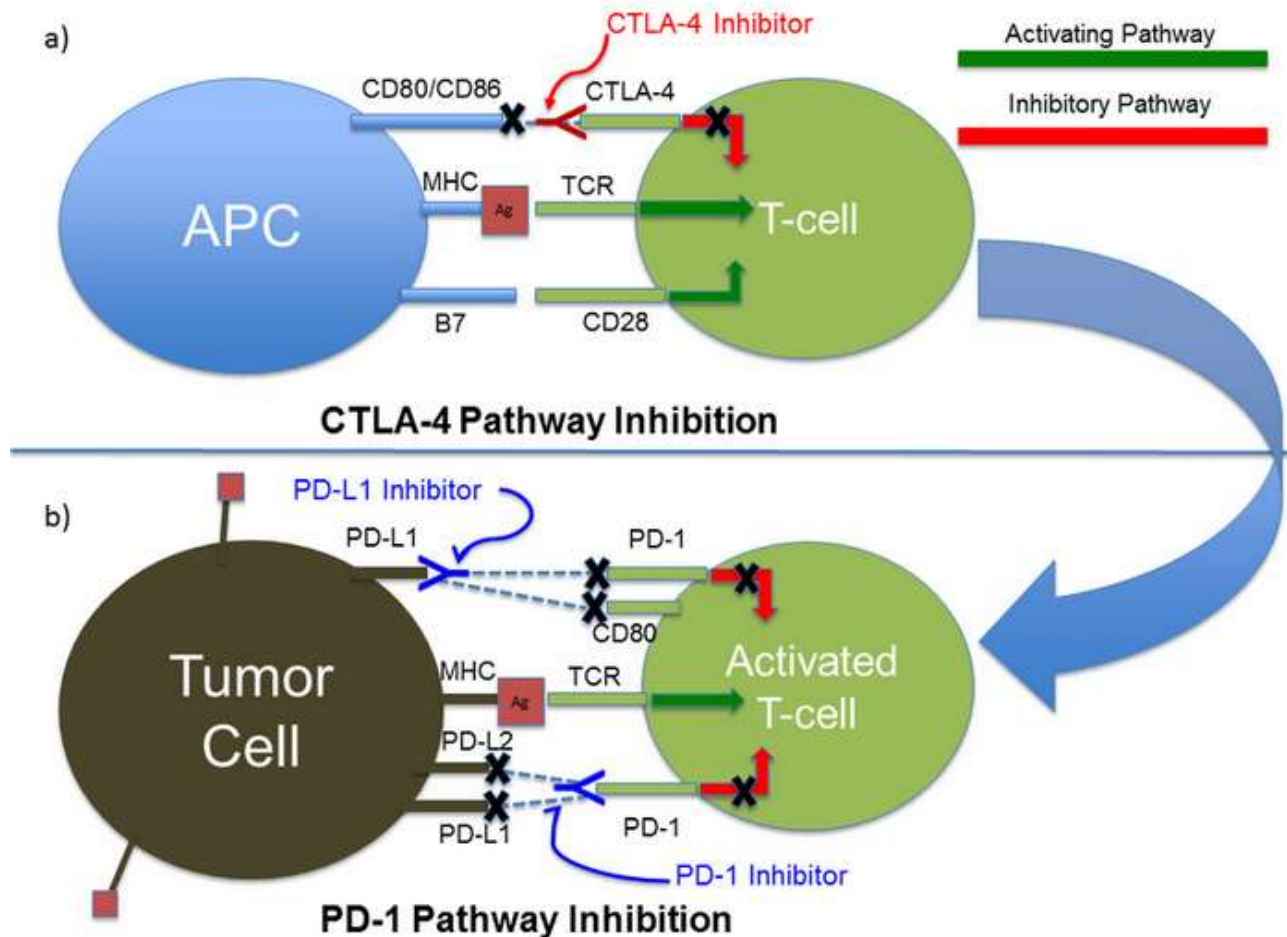
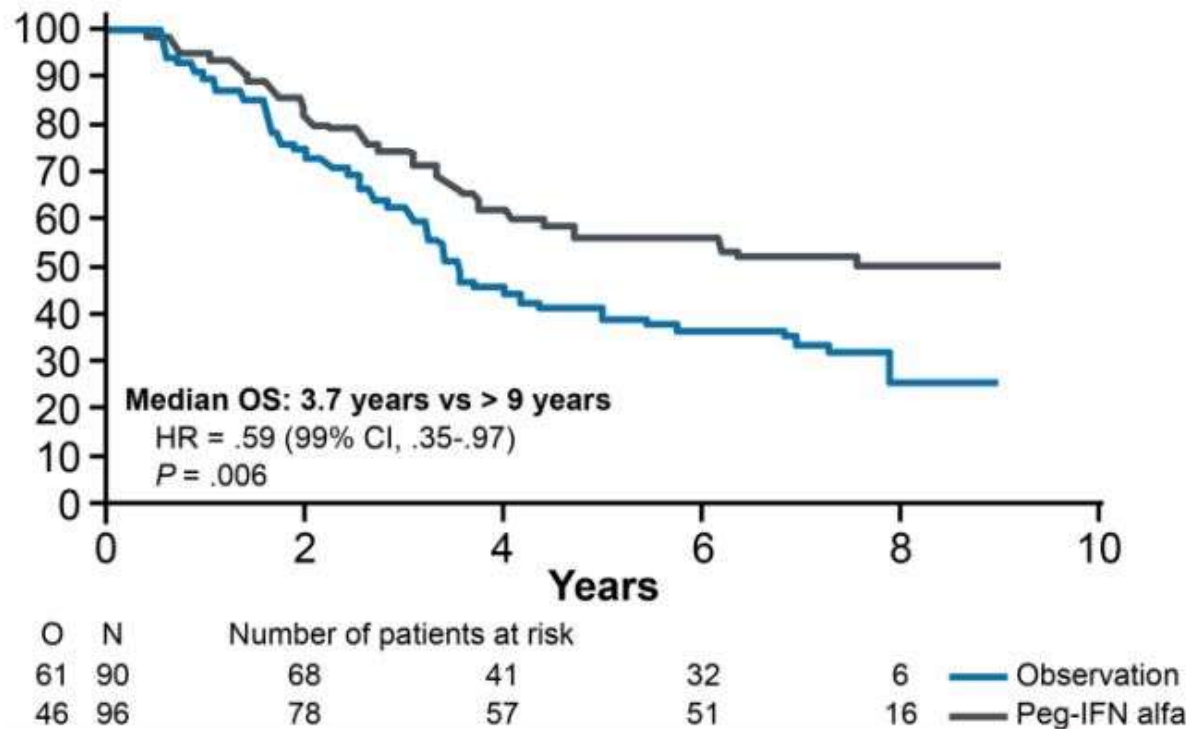# Partners in Immune System Signaling
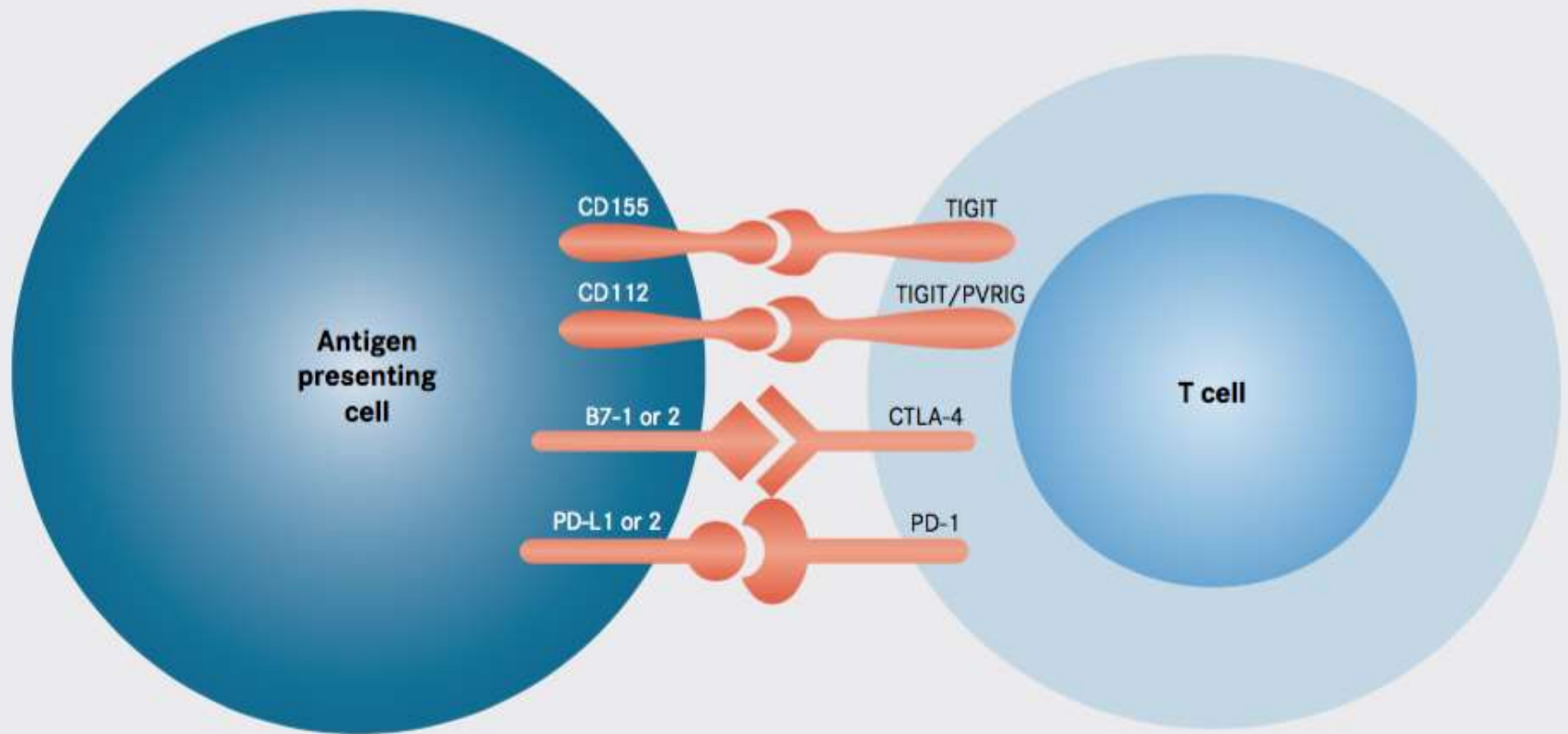
TIGIT is among the T-cell receptors that interact with proteins expressed by antigen presenting cells to send inhibitory signals to the immune system. Dysregulated interaction between TIGIT and its ligands serves to suppress immunity when under attack from cancer cells, similar to the activity of the PD-1 and CTLA-4 pathways.
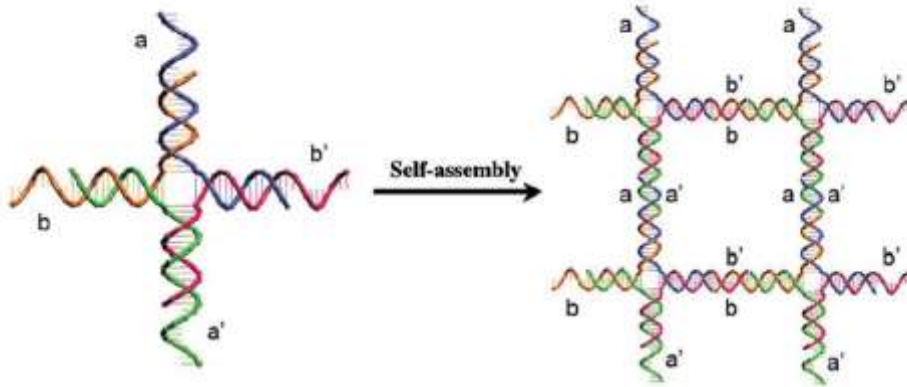
Overall Survival

Long Term Survival

Median OS: 3.7 years vs > 9 years
HR = .59 (99% CI, .35-.97)
P = .006

O	N	Number of patients at risk				
61	90	68	41	32	6	Observation
46	96	78	57	51	16	Peg-IFN alfa

Medscape
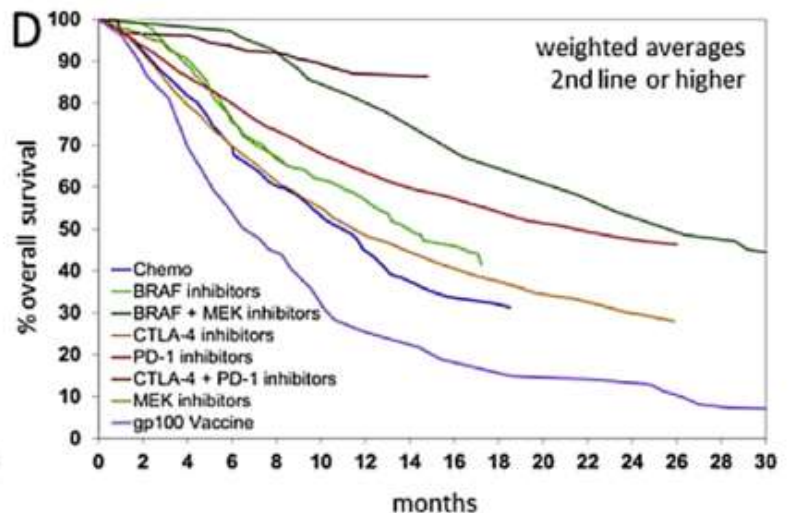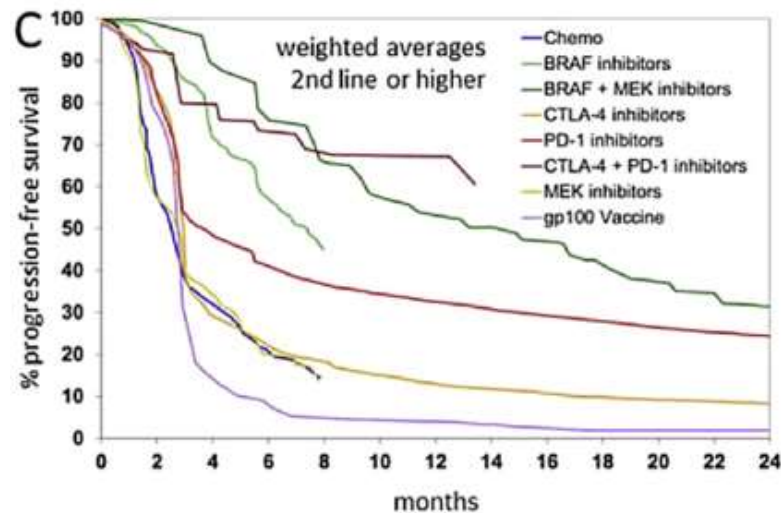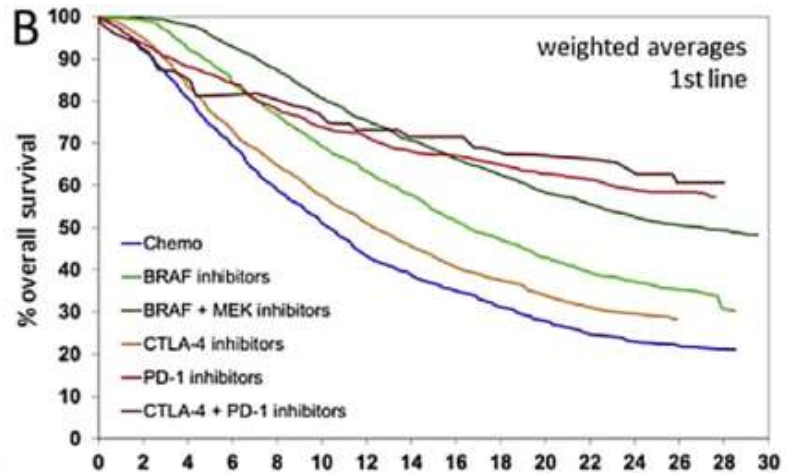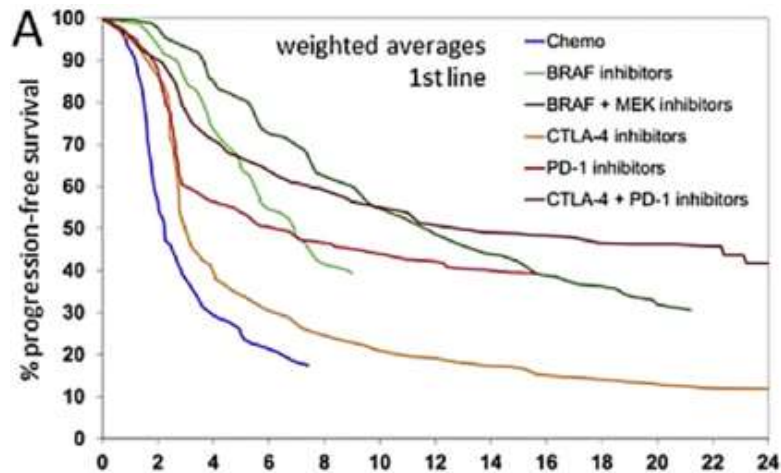
DNA Origami

Figure 1. Key concept of DNA tile based self-assembly: combining branched DNA junction with sticky-end associations (e.g. a–a′ and b–b′ pairings) to self-assemble 2D lattices (adapted from ref. [1]). The DNA model was rendered using the Strata program (www.strata.com).
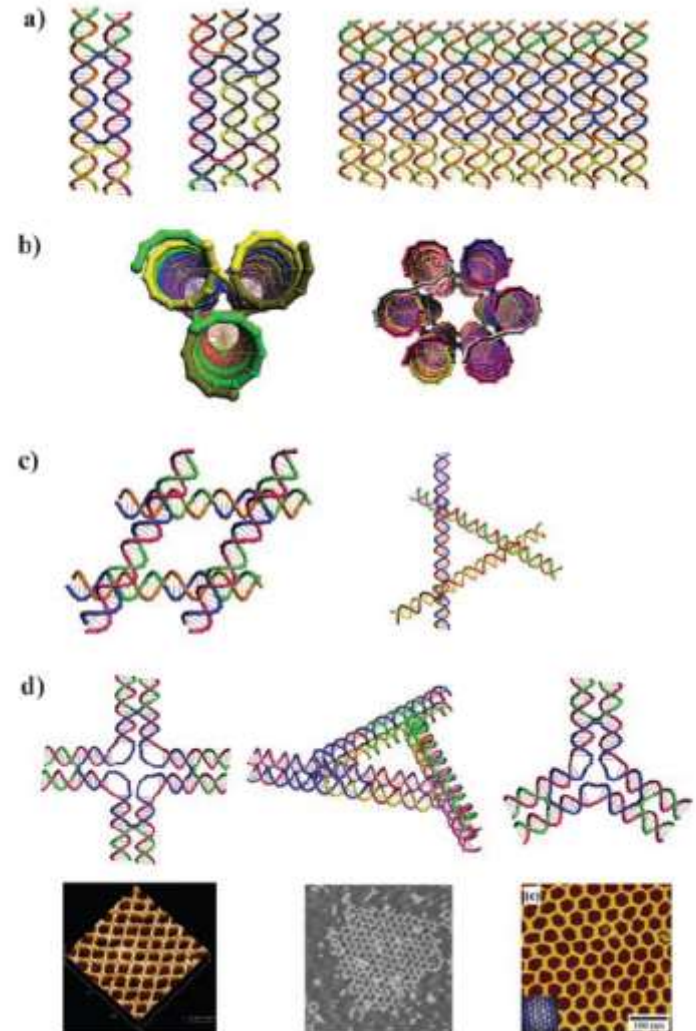
Synthesis from DNA of a molecule with the connectivity of a cube

Junghuei Chen & Nadrian C. Seeman
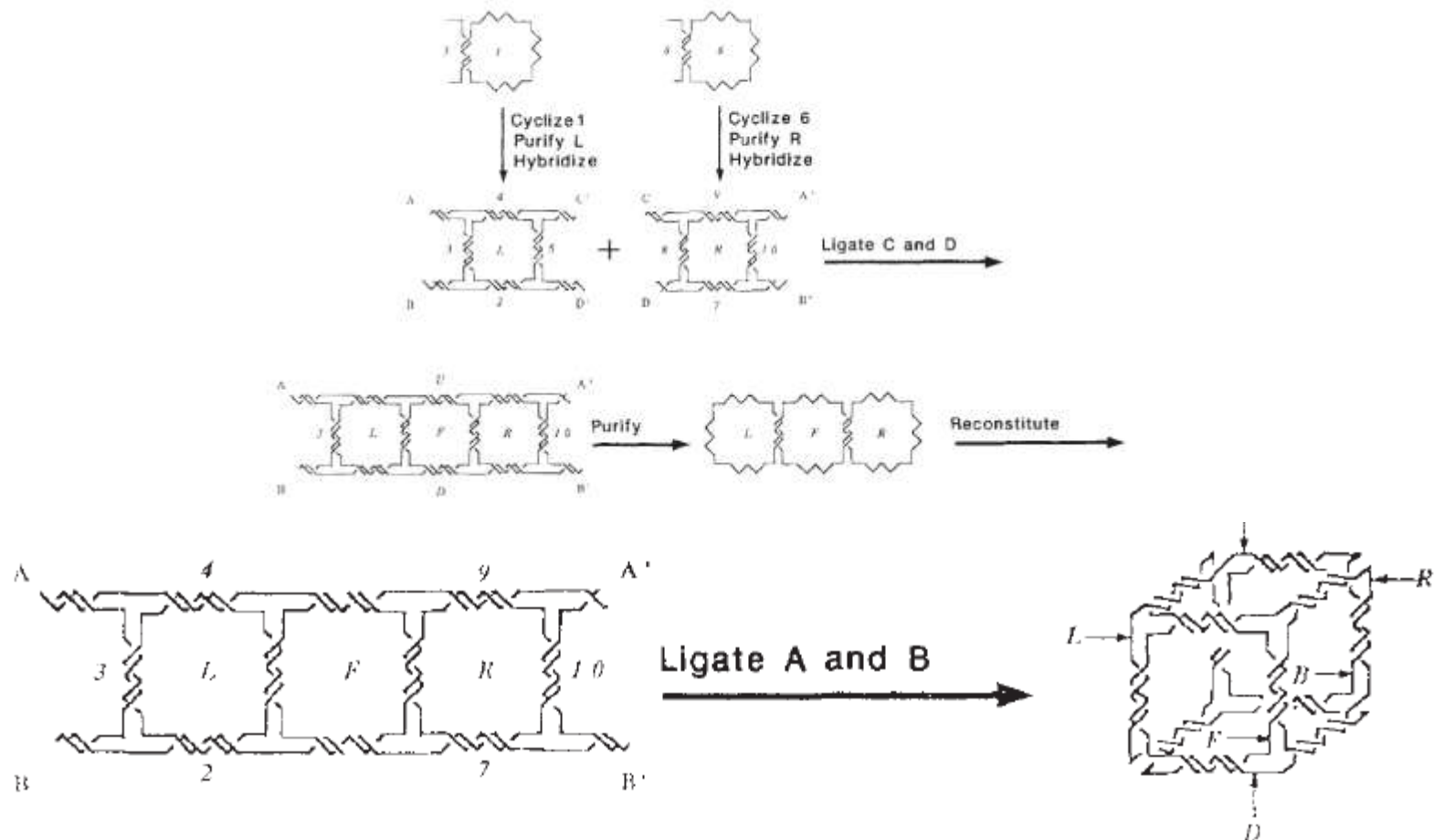
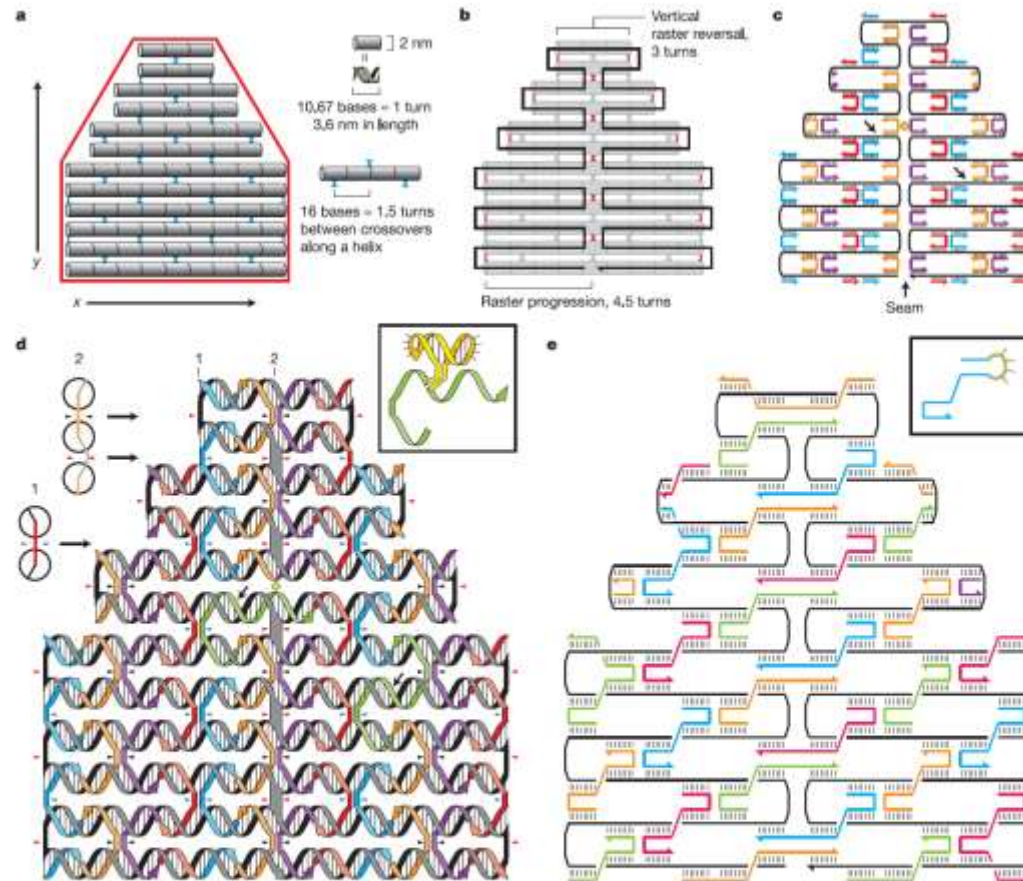# Folding DNA to create nanoscale shapes and patterns

Paul W. K. Rothemund[1]

Figure 1 | Design of DNA origami. a, A shape (red) approximated by parallel double helices joined by periodic crossovers (blue). **b**, A scaffold (black) runs through every helix and forms more crossovers (red). **c**, As first designed, most staples bind two helices and are 16-mers. **d**, Similar to **c** with strands drawn as helices. Red triangles point to scaffold crossovers, black triangles to periodic crossovers with minor grooves on the top face of the shape, blue triangles to periodic crossovers with minor grooves on bottom. Cross-sections of crossovers (1, 2, viewed from left) indicate backbone positions with coloured lines, and major/minor grooves by large/small angles between them. Arrows in **c** point to nicks sealed to create green strands in **d**. Yellow diamonds in **c** and **d** indicate a position at which staples may be cut and resealed to bridge the seam. **e**, A finished design after merges and rearrangements along the seam. Most staples are 32-mers spanning three helices. Insets show a dumbbell hairpin (**d**) and a 4-T loop (**e**), modifications used in Fig. 3.

a   b   c   d   e   f

~ 100 nm
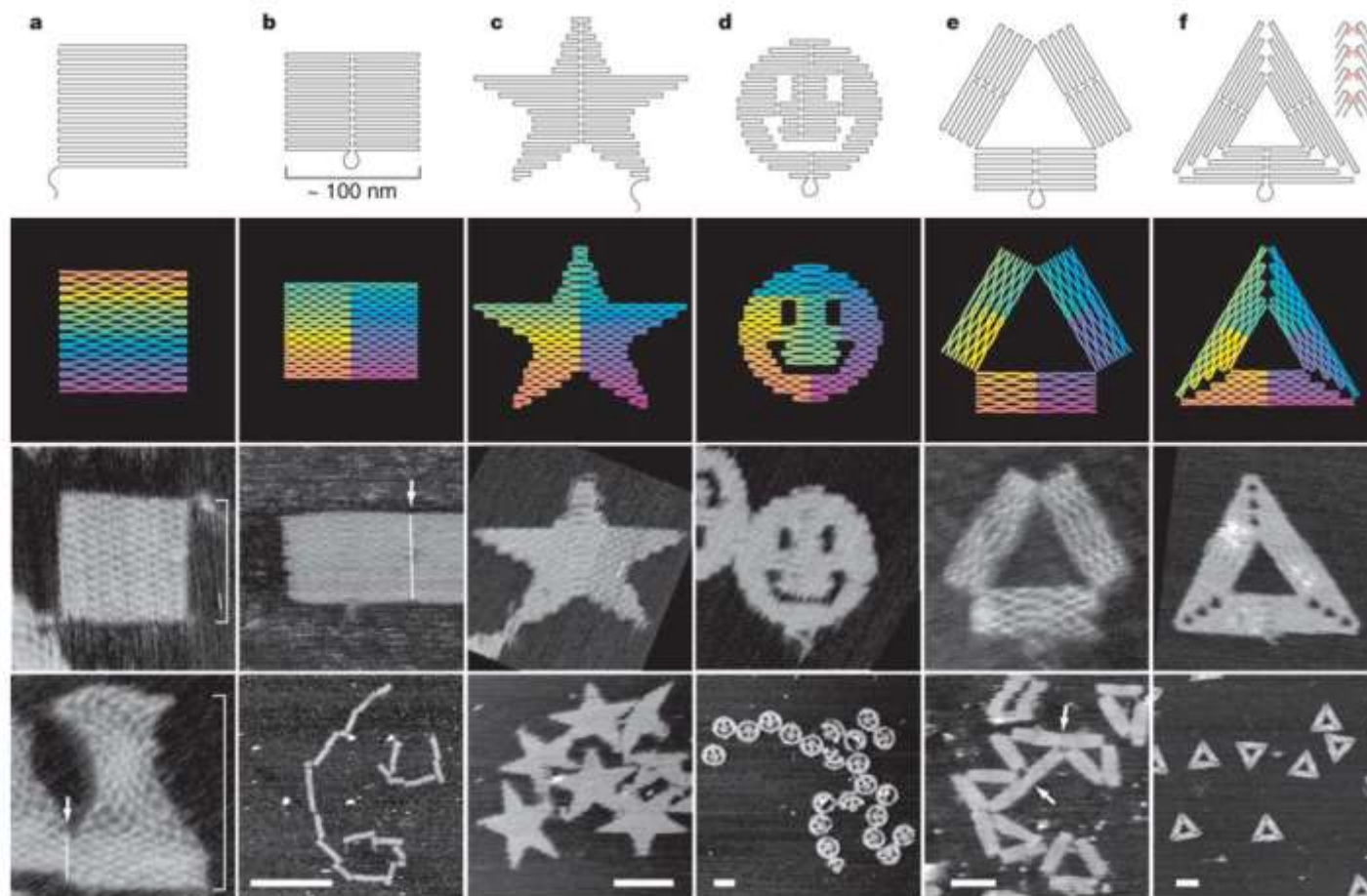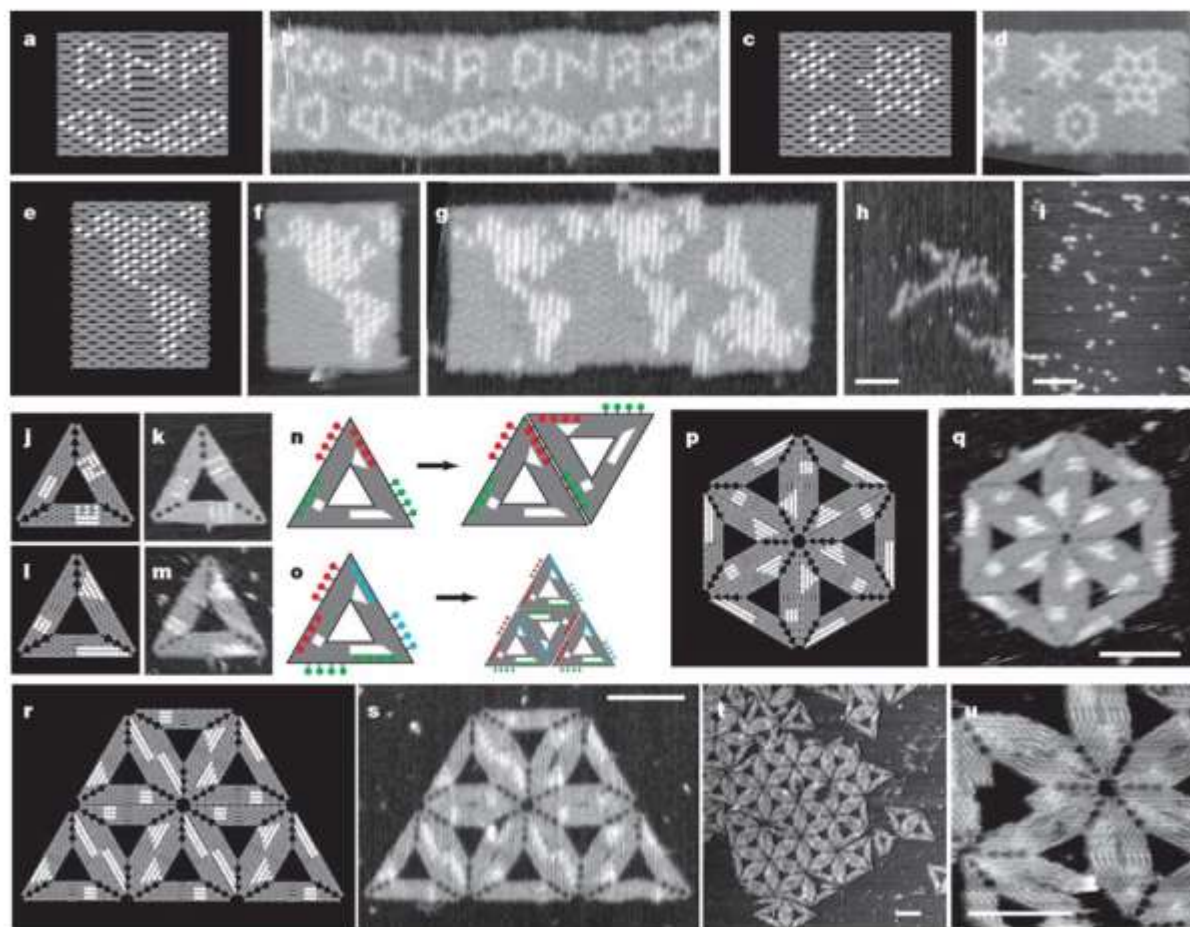
Rapid Folding of DNA into Nanoscale Shapes at Constant Temperature
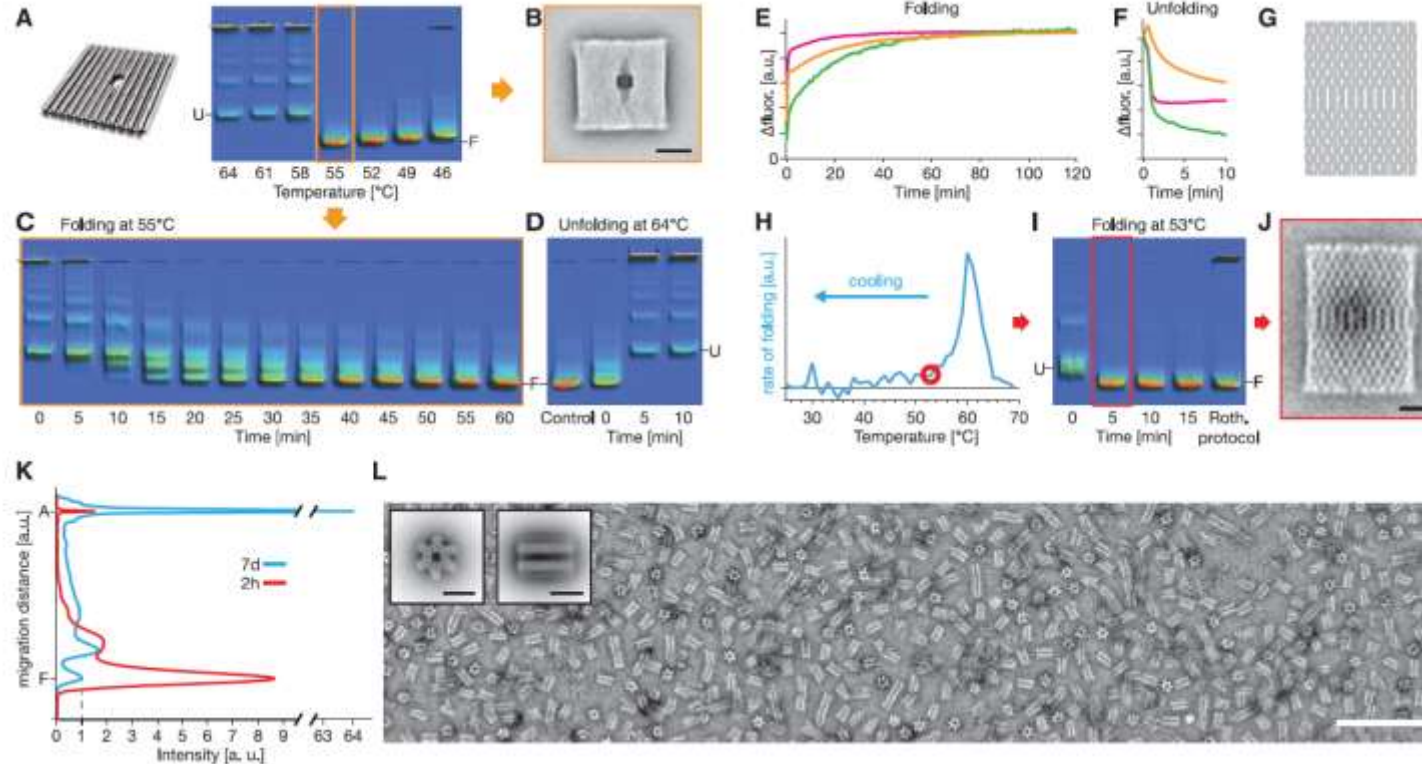
DNA Origami as a Carrier for Circumvention of Drug Resistance
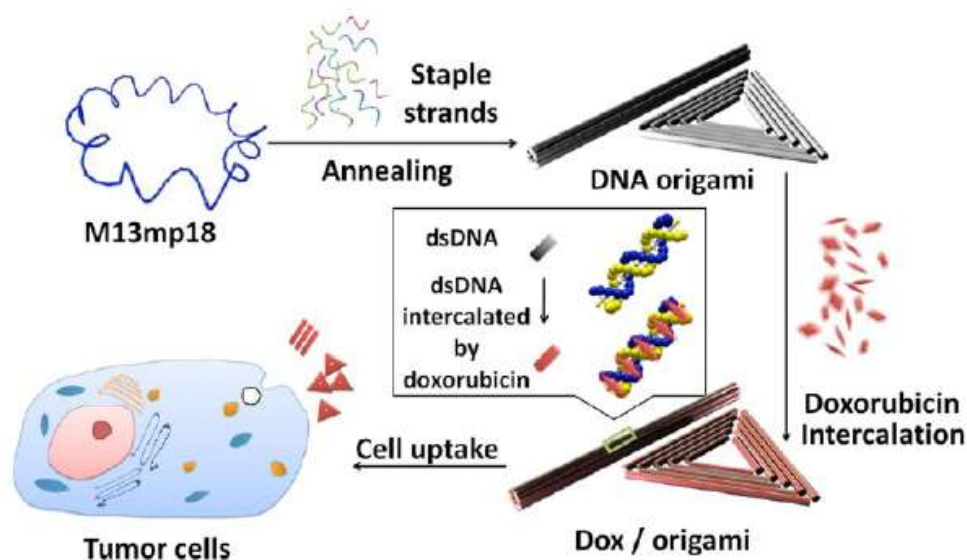
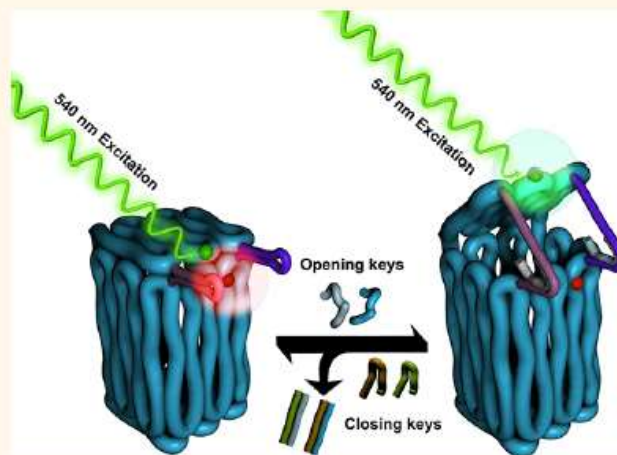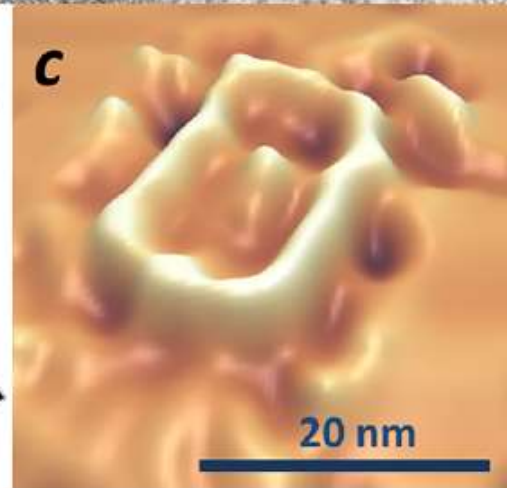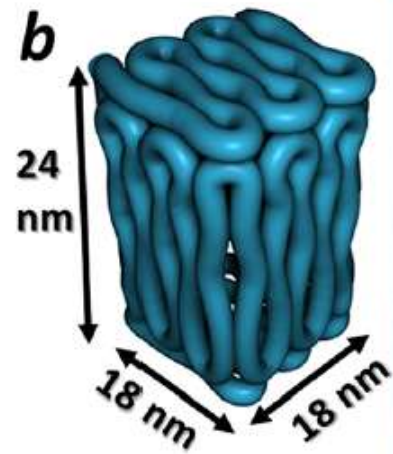**Figure 1.** DNA origami and doxorubicin origami delivery system assembly. The long single-strand M13mp18 genomic DNA scaffold strand (blue) is folded into the triangle and tube structures through the hybridization of rationally designed staple strands. Watson—Crick base pairs in the double helices serve as docking sites for doxorubicin intercalation. After incubation with doxorubicin, the drug-loaded DNA nanostructure delivery vessels were administered to MCF 7 cells, and the effects were investigated.

Construction of a 4 Zeptoliters Switchable 3D DNA Box Origami

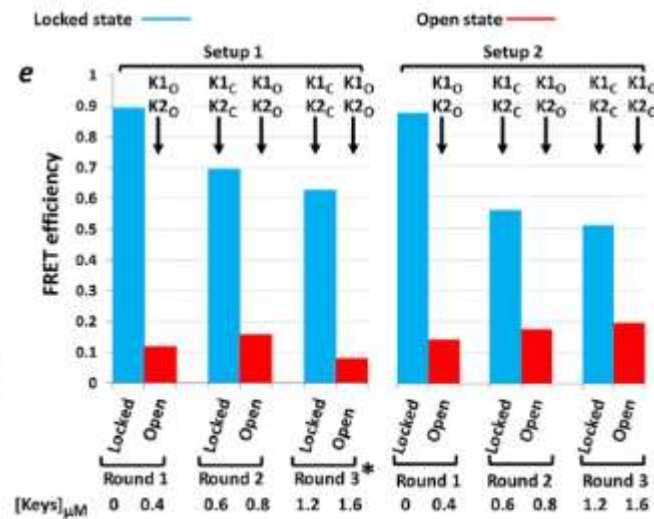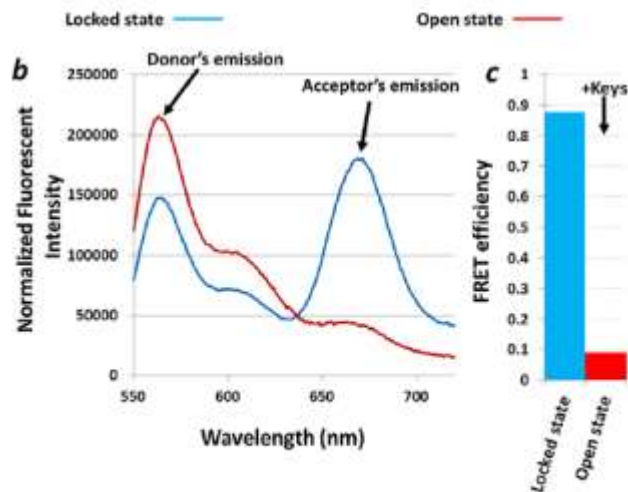**ABSTRACT** The DNA origami technique is a recently developed self-assembly method that allows construction of 3D objects at the nanoscale for various applications. In the current study we report the production of a $18 \times 18 \times 24$ nm^3 hollow DNA box origami structure with a switchable lid. The structure was efficiently produced and characterized by atomic force microscopy, transmission electron microscopy, and Förster resonance energy transfer spectroscopy. The DNA box has a unique reclosing mechanism, which enables it to repeatedly open and close in response to a unique set of DNA keys. This DNA device can potentially be used for a broad range of applications such as controlling the function of single molecules, controlled drug delivery, and molecular computing.

a

100 nm

b

24 nm

18 nm   18 nm

c

20 nm

a

Cy3

Locks

Cy5

Keys

Locked state   Open state

b

Donor's emission

Acceptor's emission

Normalized Fluorescent Intensity

250000

200000

150000

100000

50000

0

550   600   650   700

Wavelength (nm)

c

FRET efficiency

1

0.9

0.8

0.7

0.6

0.5

0.4

0.3

0.2

0.1

0

+Keys

Locked state   Open state

d

Cy3

Locks

Cy5

Opening keys
$K1_O$ & $K2_O$

Closing keys
$K1_C$ & $K2_C$

Locked state   Open state

e

Setup 1   Setup 2

$K1_C$ $K1_C$ $K1_O$ $K1_C$ $K1_O$ $K1_O$ $K1_C$ $K1_O$ $K1_C$ $K1_O$
$K2_C$ $K2_C$ $K2_O$ $K2_C$ $K2_O$ $K2_O$ $K2_C$ $K2_O$ $K2_C$ $K2_O$

FRET efficiency

1

0.9

0.8

0.7

0.6

0.5

0.4

0.3

0.2

0.1

0

Locked Open   Locked Open   Locked Open   Locked Open   Locked Open   Locked Open

Round 1   Round 2   Round 3 *   Round 1   Round 2   Round 3

$[Keys]_{\mu M}$ 0   0.4   0.6   0.8   1.2   1.6   0   0.4   0.6   0.8   1.2   1.6

A Logic-Gated Nanorobot for Targeted Transport of Molecular Payloads
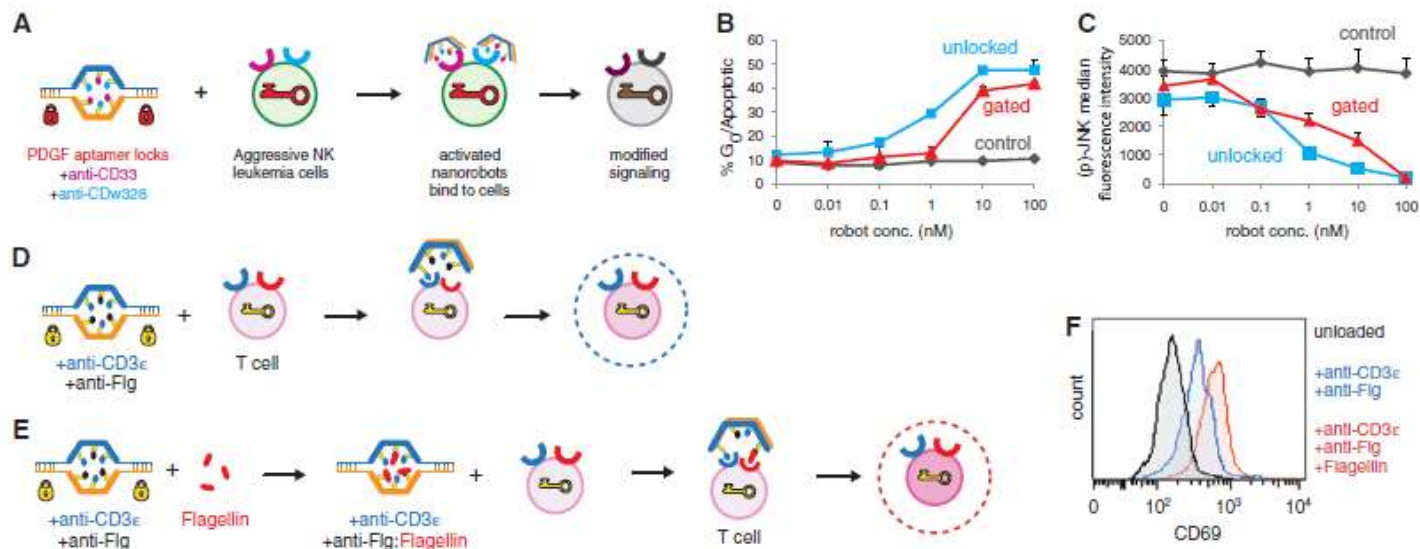
Shawn M. Douglas,* Ido Bachelet,* George M. Church†
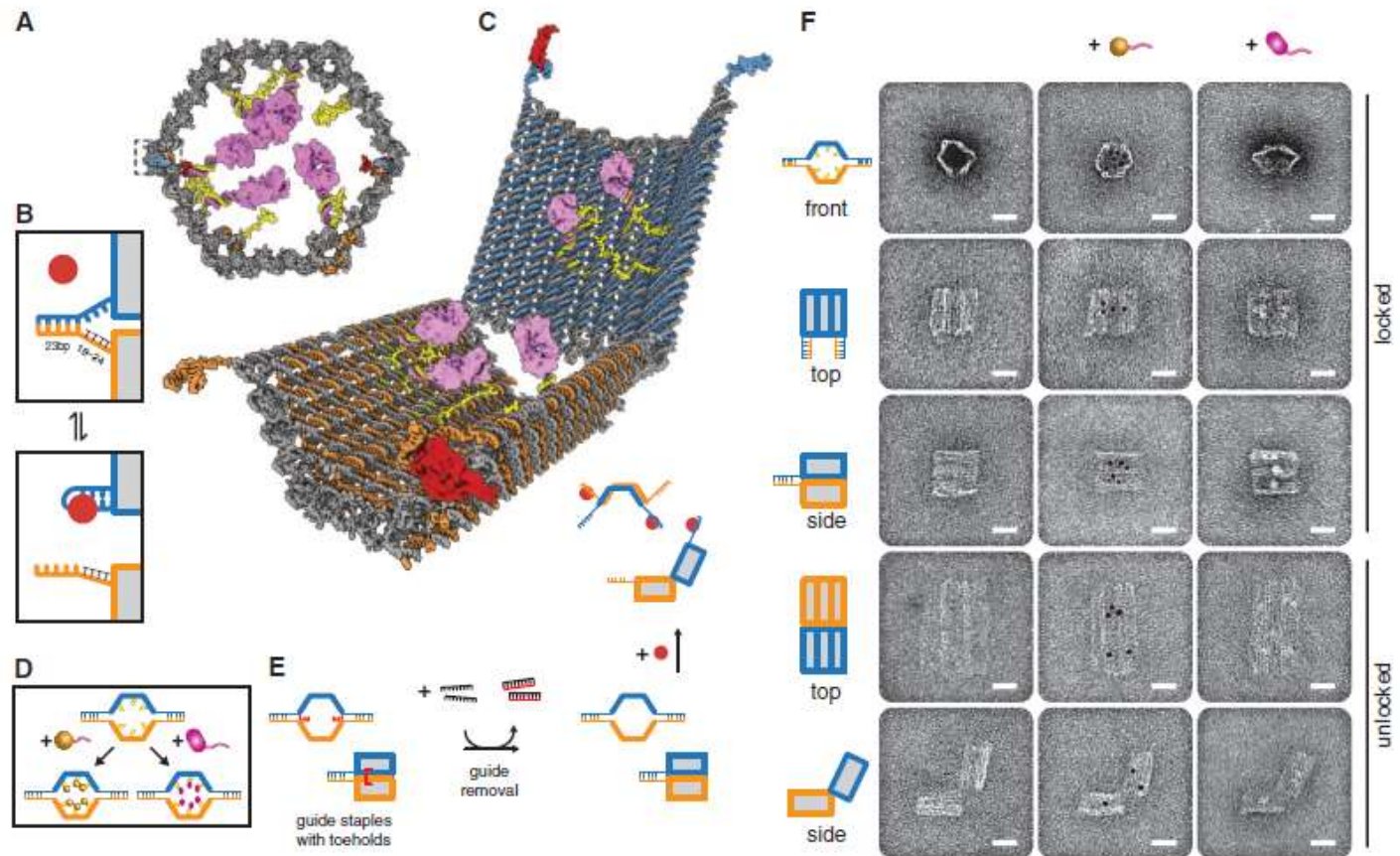
Fig. 3. Nanorobots manipulate target cell signaling. (A) Experimental scheme. A single dose of nanorobots loaded with an equal mixture of antibody to human CD33 and antibody to human CDw328/Siglec-7 Fab´ fragments (cyan and magenta, respectively, each at a molar excess of 10 over nanorobots) and gated by 41t locks recognizing platelet-derived growth factor (PDGF) were used to treat NKL cells at various concentrations (0 to 100 nM). Phosphorylation of JNK was measured after 72 hours by intracellular flow cytometry. **(B)** NKL cells (10,000 per sample) treated with nanorobots were analyzed after 72 hours for cell cycle distribution by propidium iodide (5 µg/ml). **(C)** Phosphorylation level of JNK as a function of robot concentration (lowest, 0; highest, 100 nM) after 72 hours. Error bars for (B) and (C) represent SEM of two biological replicates. **(D** and **E)** Incremental activation of T cells by nanorobots loaded with antibody to human CD3ε (blue) and antibody to flagellin Fab´ (black). Nanorobots (50 nM) with (E) and without (D) pre-incubation with flagellin (red; 100 pg/ml) were reacted with Jurkat T cells (pink) for 1 hour at 37°C. **(F)** Histograms showing T cell activation after nanorobot treatment, as measured by labeling with FITC-labeled antibody to CD69.